THE UNIVERSITY *of* EDINBURGH

Mechanisms of climate variation in the broader Mexican-United States region: the role of atmospheric circulation and anthropogenic forcing

Ivonne Mariela García Martínez

THE UNIVERSITY
of EDINBURGH

Thesis submitted in fulfilment of
the requirements for the degree of
Doctor of Philosophy
to the
University of Edinburgh — 2020

Declaration

I declare that this thesis has been composed solely by myself and that it has not been submitted, either in whole or in part, in any previous application for a degree. Except where otherwise acknowledged, the work presented is entirely my own.

Ivonne García Mtz

Ivonne Mariela García Martínez

August 2020

To my loving parents, Flor y Agustín

To Luis, my partner in discoveries

A mis amorosos padres, Flor y Agustín

A Luis, mi compañero de descubrimientos

Abstract

The climate of the region comprising Central America, Mexico and the United States (US) has undergone important temperature and precipitation changes in the recent decades. For instance, a rapid warming has been identified, in line with the current global trend. Annual precipitation has decreased over central and southern Mexico with increased precipitation variability and more severe droughts, while a positive trend has been observed in northern Mexico and most of the US. This has had profound impacts on society, water resources, and the local economy. Along with greenhouse gases, anthropogenic aerosols –in particular sulphate– are thought to be the main contributors to these changes. Yet, the relative contribution from aerosols represents the largest uncertainty in current estimates of this human-driven climate change. This PhD research is therefore aimed at contributing in the understanding of the mechanisms that modulate the climate variations in the region, in particular, the role of dynamical features and anthropogenic forcing in the mean and extreme climate states. This is achieved by using a range of observational and remote-sensing datasets, atmospheric reanalyses and advanced modelling experiments. We apply both simple and more sophisticated statistical techniques to create an integral mechanistic picture of the pathways linking large-scale dynamics with regional changes. The thesis is organised as follows: after a general introduction (Chapter 1), I present three independent but related core Chapters (2-4), followed by Conclusions (Chapter 5).

In Chapter 2, I analyse the summer spatial structure and sub-monthly

temporal evolution of one of the key dynamical features of Central American climate, the Caribbean Low-Level Jet (CLLJ), by means of extended empirical orthogonal functions (EEOFs) and lead and lag linear regressions using reanalysis data (1979-2010). This approach reveals new insights into the dynamical processes and spatio-temporal evolution of the CLLJ summer intensification and allows to identify significant climate links in the broader Caribbean region. The results show that the CLLJ generates significant precipitation and temperature responses with a distinct temporal evolution over the Caribbean-Atlantic domain and the tropical Pacific, which hints at different underlying controlling mechanisms over these two regions. An influence of extratropical hemispheric-wide waves on the CLLJ intensification is identified, which along with the weakening of a thermal low in northeast Mexico-central US trigger the summer intensification of the CLLJ. Additionally, two leading modes of tropical variability, El Niño Southern Oscillation and the Madden-Julian Oscillation, are found to further intensify the CLLJ and to extend its life cycle during summer. The full nature of these relationships was only partially appreciated, if not overlooked, in previous works. This analysis therefore contributes with a unitary mechanistic portrayal of the CLLJ evolution and its large-scale climate links, thus providing novel details to be used for predictability of regional precipitation events.

The effects of North American sulphate aerosol emissions on the climate of the United States and Mexico during 1950-1975 (the period of peak aerosol emissions) are investigated in Chapter 3. Two sets of historical experiments (each of 8 members) conducted with the Community Earth System Model (CESM) are used to isolate the impact of regional aerosol changes: an all-forcing experiment (ALL) and an identical one but with North American aerosol emissions kept at their pre-industrial levels (NoNA). Linear trends of the ensemble-mean atmospheric fields are computed for each set and, by obtaining their difference (ALL-NoNA), we identify the aerosol-driven changes. The results show that the sharp 1950-1975 increase in North American sulphate aerosols had important regional and

remote effects. In central US and northern Mexico, strengthened easterlies and aerosol direct and indirect effects caused a cooling trend and enhanced precipitation. These continental anomalies are embedded in a hemispheric-wide upper-tropospheric teleconnection pattern that originates in the north-equatorial Pacific and extends through North America and the extratropical Atlantic. This analysis pinpoints at the prominent role of adjustments in the atmospheric circulation and the interplay between local and remote influences in realising the impact of North American aerosols. The improved understanding of regional as well as large-scale climate response to the 20^{th}-century changes in North American aerosols is key for achieving more robust near-future regional projections.

Finally, in Chapter 4, the characterisation of three independent heat wave (HW) types over Mexico and the US during the second half of the 20^{th}-century using the CESM Large Ensemble and observations is carried out. To identify recent changes, the trends in frequency, duration and intensity of compound, daytime and nighttime HWs in the summers of 1950-1975 and 1980-2005 are contrasted. In addition, the relative contribution from anthropogenic aerosols and greenhouse gases (GHGs) is identified by comparing an all-forcing set of simulations (40 members) with identical sets where aerosols and greenhouse gases are kept at their 1920 levels (20 members each). The results show that all three types of HWs became considerably more frequent, longer and more intense in the recent period. Notably, each HW type shows a preferred location of occurrence, though. The compound heat waves show the largest changes over northern Mexico, west and central US; the daytime type is more recurrent over east US, the south-central US states and in Mexico; and the nighttime HWs occur mostly over the southeast US, central and southern Mexico. A strong anthropogenic imprint is found. Aerosols dominate the compound HWs over central US, the daytime HWs in large part of the domain and the nighttime HWs over Mexico during the first period. Their impact is realised predominantly via aerosol-radiation interactions. Greenhouse gases, on the other hand, play a major role in increasing the frequency,

duration and intensity of HWs throughout the domain in the recent period in all three HW types. Increasing greenhouse gas emissions impact the HW trends directly, through an enhanced greenhouse effect, and indirectly, via dynamical adjustments in the local atmospheric circulation and associated feedbacks. This chapter highlights the importance of using distinct HW definitions to properly identify the more recurrent HW type in each region and their associated forcing factors. A deeper understanding of these extreme events is necessary for building regionally-customised trustworthy future projections in a changing climate.

Altogether, the results from this PhD thesis contribute to the understanding of the mechanisms modulating regional climate variability, including the fundamental role of the atmospheric circulation and anthropogenic forcing on the mean and extreme climate over the broader Central America-Mexico-US region. It is our hope that this improved mechanistic understanding will contribute to reducing the uncertainties in near-future projections of regional hydroclimate variability.

Lay Summary

The climate of the region comprising Central America, Mexico and the United States (CAMUS) underwent important temperature and precipitation changes in the recent decades. For instance, a rapid warming has been identified, in line with the current global trend. Annual precipitation has decreased over central and southern Mexico with increased precipitation variability and more severe droughts, while a positive trend has been observed in northern Mexico and most of the US. This has resulted in large negative impacts on the well-being of the local population and on the ecosystems. Among all the factors driving climate change, greenhouse gases (GHGs) play the most critical role. Second to this, human-made aerosols also have an effect on the Earth's climate, and are currently one of the largest sources of uncertainty in climate model projections. While GHGs tend to warm the surface, aerosols, on average, cool it down mainly by blocking sunlight. Aerosols also interact with clouds, changing their properties and therefore modifying regional rainfall patterns. Their effects can be perceived on remote areas, through changes in the atmospheric circulation. In the 20^{th} century, North America was one of the largest emission sources of aerosols worldwide. However, the extent to which aerosols may have affected climate over the CAMUS region is still uncertain.

This PhD work aims at improving the understanding of the mechanisms responsible for the recent climate variations in the CAMUS region, in particular, the role of atmospheric circulation and the human influence. To accomplish this, we use observed data and advanced climate simulations. First, we study the

sub-monthly characteristics (spatial pattern and temporal evolution) of one of the dominant elements of Central American climate, the Caribbean low-level jet. This jet is a region of strong near-surface easterly winds over the Caribbean that is present all-year round but it is more intense in the summer. Most of the previous studies focused on seasonal to year-to-year variations. However, the jet varies along with other land-ocean-atmosphere processes on days to weeks, so studying its sub-monthly variability is a relevant, yet overlooked, matter. The results show that the jet modulates the summer changes in precipitation and temperature, with a different temporal evolution in the Caribbean-Atlantic region to that found in the tropical Pacific. This suggests that there are two distinct mechanisms in play over these regions. The surface anomalies are linked with the upper atmosphere, where a vertical circulation cell over the Caribbean Sea is found. Also, we found that the jet is influenced by two large-scale oscillations: the El Niño Southern Oscillation and the Madden-Julian Oscillation, that strengthen the jet and make it more persistent. These results help to advance the understanding of the processes that modulate local climate variations, which is an important issue in view of the rapid climate change the region is undergoing.

Next, we assess the impact of North American sulphate aerosol emissions on the climate of Mexico and the United States (US), using a state of the art global climate model. Sulphate aerosols are the most common human-made aerosol type and are created by the burning of coal and oil. The results show that aerosols had important regional and remote effects. In northern Mexico and central US, temperature decreased and rainfall increased during 1950-1975, as North American aerosol emissions reached their peak. In Mexico, the high central mountains and aerosol-induced moist flow from the Gulf of Mexico favoured more rainfall on the Atlantic slope and less over the Pacific side. We find that these land anomalies brought about by the aerosols increase are part of a large-scale wave pattern that extends from the Pacific-North American region towards the extra-tropical Atlantic. Understanding these effects is essential for climate change

adaptation, as currently it is largely uncertain by how much did aerosols offset the GHGs warming and as aerosol emissions continue to decrease in the near-future both in North America and worldwide.

Finally, we study the summer heat waves (HW) over Mexico and the US in the second half of the 20^{th} century. We do so by focusing on three main aspects. First, we classify the HWs into three types: compound, daytime and nighttime and characterise their frequency, duration and intensity for two different periods with opposing aerosol trends (1950-1975 and 1980-2005). Then, we identify the relative role of global human-made aerosols and GHGs on the HW changes for the two periods. Lastly, we describe the physical mechanisms associated with these changes. For this analysis, we use three large ensembles with different external forcing (up to 40 members), which allows us to separate the natural from the human-made changes with some confidence. The results show that all three types of HWs became considerably more frequent, longer and more intense in the recent period. However, each HW type shows a clear preferred location of occurrence. Furthermore, we find a strong human-made signal in these changes, with aerosols dominating the compound HWs over central US, the daytime HWs in large part of the domain and the nighttime HWs over Mexico during the first period. On the other hand, GHGs play a major role in increasing the HW indicators throughout the domain in the second period in all three HW types. Therefore, we highlight the importance of using different HW definitions to properly identify the more recurrent HW type in each region and their associated forcing factors. An improved knowledge of the HW changes is necessary for developing regionally-customised strategies for adaptation and mitigation to these climate extremes that severely impact human health and ecosystems.

Altogether, the results from this PhD thesis contribute to the understanding of the mechanisms modulating climate variability over the CAMUS region, including the fundamental role of the atmospheric circulation and human influence on the mean and extreme climate. It is our hope that this improved mecha-

nistic understanding will contribute to reducing the uncertainties in near-future projections of regional climate variability.

Acknowledgements

I would like to thank Massimo Bollasina for his endless enthusiasm and guidance throughout my PhD. We had some good times and I appreciate the shared knowledge and your sincere friendship. Thank you to David Stevenson for his professional support in rough times. I would also like to thank the GeoSciences PGR and IT staff for offering a helping hand when needed.

My deepest gratitude to the Mexican people, who made my stay in Edinburgh possible through a PhD scholarship from the National Council for Science and Technology (CONACyT). My gratitude also extends to the School of GeoSciences for the complimentary funding to carry out my PhD work.

Thank you to my friends and fellow PhD students for the good company. Exploring Edinburgh was an even more enjoyable experience because of all the walks, dinners, and afternoons we spent together. I would also like to thank Jayoung Yun for sharing her great tech skills with me and Sabine Undorf for kindly providing the CESM runs used in Chapter 3.

Finally, I would like to especially thank my supportive family. To my hard-working parents, who have been a source of inspiration and encouragement throughout my life. Thank you to my brothers, Agustín and Paúl, for being supportive and for always making me laugh. My sincere gratitude to my partner in science and life, Luis. Thank you for supporting my decisions, for your contagious serenity and for the insightful discussions about pretty much anything.

Agradecimientos

Me gustaría agradecer a Massimo Bollasina por su ilimitado entusiasmo y orientación a lo largo de mi doctorado. Tuvimos buenos momentos y agradezco el conocimiento compartido y tu sincera amistad. Gracias a David Stevenson por su apoyo profesional en tiempos difíciles. También me gustaría agradecer al personal de la oficina de Posgrado en Geociencias y al equipo de Informática por ofrecer una mano amiga cuando fue necesario.

Mi más profundo agradecimiento al Pueblo Mexicano, que hizo posible mi estadía en Edimburgo a través de una beca de doctorado del Consejo Nacional de Ciencia y Tecnología (CONACyT). También extiendo mi agradecimiento a la Escuela de Geociencias por la financiación complementaria para llevar a cabo mi trabajo de doctorado.

Gracias a mis amigos y compañeros del doctorado por la buena compañía. Explorar Edimburgo fue una experiencia aún más agradable debido a todos los paseos, cenas y tardes que pasamos juntos. También me gustaría agradecer a Jayoung Yun por compartir conmigo sus excelentes habilidades tecnológicas y a Sabine Undorf por proporcionar amablemente las simulaciones de CESM usadas en el capítulo 3.

Finalmente, me gustaría agradecer especialmente a mi familia. A mis padres trabajadores, que han sido una fuente de inspiración y ánimo a lo largo de mi vida. Gracias a mis hermanos, Agustín y Paúl, por apoyarme y por hacerme reír siempre. Mi más sincero agradecimiento a mi compañero en la ciencia y en la

vida, Luis. Gracias por apoyar mis decisiones, por tu contagiosa serenidad y por las estimulantes discusiones sobre prácticamente cualquier cosa.

Contents

List of Figures

List of Acronyms

BEST: Berkeley Earth Surface Temperature
CESM: Community Earth System Model
CFSR: Climate Forecast System Reanalysis
CHIRPS: Climate Hazards Group InfraRed Precipitation with Station data
CLLJ: Caribbean Low-Level Jet
CMAP: Climate Prediction Center Merged Analysis of Precipitation
CRU: Climatic Research Unit of the University of East Anglia
ENSO: El Niño - Southern Oscillation
EEOF: Extended Empirical Orthogonal Functions
EOF: Empirical Orthogonal Functions
GHGs: Greenhouse gases
GPLLJ: Great Plains Low-Level Jet
HW: Heat wave
HWD: Heat wave duration
HWF: Heat wave frequency
HWI: Heat wave intensity
ITCZ: Intertropical Convergence Zone
LENS: Large ensemble
MFC: Moisture Flux Convergence
MJO: Madden-Julian Oscillation
NASH: North Atlantic Subtropical High pressure system
PC: Principal component
SST: Sea surface temperature
SLP: Sea level pressure
TOA: Top of the atmosphere
TRMM: Tropical Rainfall Measurement Mission
US: United States of America

USMEX: Merged Climate Prediction Center Unified Precipitation for the US and station data over Mexico

Chapter 1

Introduction

1.1 Motivation

This PhD thesis addresses the mechanisms that modulate the summer climate variations over the region comprising Central America, Mexico and the United States (CAMUS), with an emphasis on the role of atmospheric circulation and anthropogenic forcing in both mean and extreme climate. The motivation for this research generates from the substantial changes in climate the region has recently undergone. In particular, an overall rapid warming has been identified (Pachauri et al. 2014; Wuebbles et al. 2017), in line with the current global trend. Annual precipitation has decreased over central and southern Mexico, while a positive trend has been observed in northern Mexico and most of the US (Pachauri et al. 2014; Wuebbles et al. 2017). Besides, the intensity and severity of droughts in some regions of the US and Mexico have increased (Stahle et al. 2009; Wuebbles et al. 2017; Vega-Camarena et al. 2018). This had profound impacts on society, water resources, and the local economy (Stocker et al. 2013). Moreover, the climate of the CAMUS region is modulated by diverse regional and remote multi-scale atmospheric and oceanic phenomena and by a varied topography (composed by coastal plains, islands chains, mountains ranges of different altitudes and orientations, interior basins and high plateaus; Hastenrath

1967; Taylor and Alfaro 2005), which contributes to making the climate of this region inherently complex. Further, the changes in regional climate are expected to continue in the near and long-term future. For instance, CMIP5 models project strong additional warming and a large precipitation reduction throughout the 21^{st} century, particularly during the summer, although with considerable uncertainty (Karmalkar et al. 2011; Taylor et al. 2012; Stocker et al. 2013). Understanding the drivers and mechanisms of these changes is therefore of relevance for the society.

Wet-season (May-October) precipitation is of utmost importance for southern Mexico and Central America as it provides more than 80% of the annual total rainfall of the region, and it is a vital resource for the regional economy, agriculture, ecosystems as well as the livelihood of the nearly 180 million inhabitants (United Nations 2019). Yet, its large spatio-temporal rainfall variability poses a significant challenge as it can adversely impact a number of activities in this vulnerable region, such as tourism, hydropower generation, agricultural output, and the overall management of critical water resources (e.g., Méndez and Magaña 2010). For example, during the 2011-2012 prolonged drought, one of the most severe and damaging in recent decades, 86% of Mexican territory experienced a severe water crisis, with economic losses exceeding $1.2 billion US dollars in the agriculture sector alone and reduced water supplies for more than 2 million people (Neri and Magaña 2016). In particular, subseasonal rainfall variability –which manifests as wet and dry spells– is a critical factor as periods of intense rainfall and droughts can adversely affect agricultural output and farmer livelihoods (e.g., Endfield et al. 2006; Neri and Magaña 2016). On the long term, precipitation is expected to significantly change by the end of the century (e.g., Taylor et al. 2013; Pachauri et al. 2014), although there are considerable discrepancies among the studies on the spatial pattern of changes (e.g., Singh 1997; Angeles et al. 2007; Karmalkar et al. 2011; Campbell et al. 2011; Hall et al. 2013).

A large contribution to this uncertainty stems from our current limited understanding of the mechanisms underpinning regional precipitation variability,

including the fundamental role of the atmospheric circulation. This is directly reflected on model biases related to the physical parameterisations used. Improved knowledge of the pathways linking large-scale dynamics with regional rainfall changes is key to achieve more confidence in projections of future changes of regional water resources. This will allow policy makers to formulate more adequate and plausible mitigation and adaptation plans to climate change across a wide range of climate-sensitive activities and sectors.

Another pressing issue in the climate of the CAMUS region is understanding and quantifying the influence of anthropogenic forcing. Aside greenhouse gases (GHGs), anthropogenic aerosols have been important drivers of global, but especially regional, climate change (Pachauri et al. 2014). In general, aerosols exert an opposite effect on the Earth's radiative balance to that of GHGs. While the effect of the GHGs is to warm the planet by decreasing the emission of longwave radiation back to space, the net effect of aerosols is to cool it down. Aerosols can absorb and reflect solar radiation (the direct effect; Charlson et al. 1992) and modify clouds properties (the indirect effect; Twomey 1977; Albrecht 1989), which impacts the hydrological cycle (e.g., Ming and Ramaswamy 2009; Leibensperger et al. 2012; Bollasina et al. 2014).

The effects of anthropogenic GHGs and aerosols have been observed in the changes of mean and extreme climate across different regions of the world, including in North America. For instance, GHGs are the well-known drivers of the post-industrial warming at global scale (Pachauri et al. 2014). Whereas the counteractive cooling effect of aerosols took a leading role in the Northern Hemisphere midlatitudes, where aerosol loadings were largest (Ming and Ramaswamy 2009). In addition, increases in aerosol emissions have been related to large circulation changes on major monsoon systems around the globe (e.g., Bollasina et al. 2011; Song et al. 2014; Undorf et al. 2018b). Even though some recent works have emphasised the influence of North American and global anthropogenic aerosols in the US (e.g., Leibensperger et al. 2012; Westervelt et al. 2015), some major

knowledge gaps still remain. For instance, the large-scale climate impact (over the neighbouring Mexico region and adjacent ocean basins) and the physical mechanisms behind the aerosol-driven changes. Identifying and quantifying the impacts of anthropogenic aerosols may help to narrow down the uncertainties of future changes in climate as well as to provide a clearer view of the projected changes in the region.

A marked anthropogenic imprint has also been found in one of the most devastating extreme weather events at global scale: heat waves. As global temperatures rose, an increase in the frequency of hot extremes was observed in many regions of the globe in the recent decades (Alexander et al. 2006; Donat et al. 2013). These extreme events had severe impacts for human health and ecosystems. For instance, one of the most damaging heat wave events in the recent decades was that experienced in Europe in 2003, where it was estimated that more than 70,000 human lives were lost (Robine et al. 2008). In the US, the heat-related morbidity and mortality are also one of the major public health threats (Luber and McGeehin 2008). The recent increase in the global heat wave activity has been strongly linked to anthropogenic forcing (Bindoff et al. 2013). Yet, the relative role of individual anthropogenic factors over the CAMUS region and their underlying physical processes are still unclear. As the anthropogenic influence on the global climate is projected to increase in the coming decades, future increases in hot extremes seem unavoidable. This poses an acute need for characterising and improving the understanding of the drivers and mechanisms of these temperature extreme events for policy making purposes and opportune adaptation strategies.

1.2 Introduction to the core chapters

In this section, an introduction to the topics covered in this thesis is given. Each of these topics (Sections 1.2.1-1.2.3) contains relevant background and point out

the knowledge gap addressed in each of the core Chapters (2-4). The research aim and objectives of this work then follow in Section 1.3.

1.2.1 Features of the regional atmospheric circulation

Central American hydroclimate is modulated by a variety of local and remote atmospheric and oceanic phenomena across a wide range of spatio-temporal scales. At seasonal and subseasonal timescales, summer (May-August) atmospheric circulation and rainfall are impacted by the zonal migration of the North Atlantic Subtropical High (NASH) and the related Caribbean Low-Level Jet (CLLJ; e.g., Hastenrath 1967; Taylor and Alfaro 2005; Amador et al. 2006), the meridional migration of the Intertropical Convergence Zone (ITCZ), and transient phenomena such as the Madden-Julian Oscillation (MJO), tropical cyclones and easterly waves (Maloney and Hartmann 2000; Inoue et al. 2002; Serra et al. 2010; Perdigón-Morales et al. 2020). Additionally, the complex topography of the region also plays a significant role in determining the distribution and pattern of precipitation and winds (e.g., Muñoz et al. 2008).

Among these factors, the CLLJ has been recognised as one of the most influential dynamic features of Mexican and Central American summer climate (Magaña et al. 1999; Amador et al. 2006; Romero-Centeno et al. 2007; Wang 2007; Muñoz et al. 2008; Amador 2008; Cook and Vizy 2010; Hidalgo et al. 2015; Herrera et al. 2015). The CLLJ is a region of intense (up to 12-14 m s^{-1}) lower tropospheric easterly winds over the Caribbean Sea, with its core between 925-700 hPa. Unlike other jets (i.e. the Great Plains low-level jet, GPLLJ) which are seasonal features, the CLLJ is present throughout the year, although its magnitude varies semiannually with maxima in July (the strongest) and February, and corresponding minima in May and October (Amador 1998; Wang 2007; Amador 2008; Whyte et al. 2008). The May to July intensification of the CLLJ is important as the jet acts as a moisture conveyor belt within the Caribbean and the surrounding areas, thus modulating moisture availability in the

region during the summer rainy season (Durán-Quesada et al. 2010). In particular, the CLLJ strengthening has been shown to be one of the main drivers of the typical mid-summer drought over southern Mexico and the Pacific slope of Central America through enhanced convection at the jet exit and associated subsidence over the eastern tropical Pacific, and by causing a southward displacement of the latitudinal centre of mass of precipitation (Hidalgo et al. 2015), leading to a rainfall decrease of up to 40% in July-August (Magaña et al. 1999; Romero-Centeno et al. 2007; Small et al. 2007; Muñoz et al. 2008). The CLLJ also modulates vertical wind shear and sea surface temperature (SST) over the Caribbean Sea, which in turn influence the formation of tropical cyclones in the region (Amador et al. 2010).

Not surprisingly, the majority of the studies on the CLLJ and its variability have focused on seasonal to interannual timescales, where the CLLJ variance peaks (e.g., Wang 2007). These studies have identified links between the CLLJ and large-scale atmospheric circulation variability over the Atlantic (e.g., Wang and Lee 2007; Cook and Vizy 2010), global-scale SST fluctuations (e.g., Mestas-Nuñez et al. 2007; Amador 2008), and regional temperature and orographic effects (e.g., Xie et al. 2005). On the contrary, higher-frequency (intra-seasonal) regional circulation variability has received much less attention (e.g., Amador et al. 2016). Yet, the seasonal variation of the CLLJ and its link with regional hydroclimate is modulated by a variety of coupled land-ocean-atmosphere processes and feedbacks which occur on short time scales (days to weeks), questioning the appropriateness of monthly or seasonal-based investigations (e.g., Serra et al. 2014; Amador et al. 2016). For example, Magaña et al. (1999) and Magaña and Caetano (2005) related sub-monthly variations of eastern tropical Pacific SST with the mid-summer drought via feedbacks between solar radiation, convective activity, and circulation fluctuations. Durán-Quesada et al. (2010) emphasised the key role of the CLLJ in driving the large-scale moisture transport toward Central America at synoptic to intraseasonal scales. Moreover, large synoptic and intraseasonal

fluctuations of the tropospheric circulation over Central America were also found to be associated with variations of the CLLJ (Amador et al. 2006; Amador 2008).

Additionally, the CLLJ is typically described on a monthly or seasonal scale, primarily by using a circulation index based on area-averaged 925-hPa zonal wind over the climatological position of the jet core (e.g., Wang 2007; Whyte et al. 2008; Cook and Vizy 2010; Maldonado et al. 2018), or alternatively, albeit much less commonly, by Empirical Orthogonal Function (EOF) analysis of the 925-hPa (zonal) wind over the Caribbean region (e.g., Whyte et al. 2008; Muñoz and Enfield 2011). Common to both methods is the assumption of stationarity of the spatial pattern of the winds during the examined season. Therefore lagged links with regional circulation and hydroclimate (e.g., Serra et al. 2010; Martin and Schumacher 2011) do not account for the underlying evolution of the CLLJ in modulating its climate signature. This is a potentially important shortcoming in investigating the underpinning mechanisms involving rapidly-evolving atmospheric dynamical features, such as the CLLJ, and ultimately hinders our understanding of the generation of sub-seasonal hydroclimate events over Central America (e.g., Alfaro et al. 2018).

It is worth mentioning that a better characterisation of the mechanisms driving the CLLJ variability is of scientific and economic relevance for a wider region as moisture transport from the Caribbean continues across Mexico to the central and southeastern US as part of the GPLLJ (e.g., Wang 2007), which exerts an important control on sub-monthly precipitation variability over the central US (Weaver and Nigam 2011), and modulates tornado activity there (e.g., Muñoz and Enfield 2011).

1.2.2 Climate impacts of North American sulphate aerosols

Aside greenhouse gases, anthropogenic aerosols currently exert a considerable forcing on the Earths radiative balance (Stocker et al. 2013). In particular,

the global radiative forcing from sulphate aerosols during the 20^{th} century is estimated to be of the same order of magnitude, but of opposite sign, to that of GHGs (Pachauri et al. 2014). Anthropogenic sulphate aerosol emissions have been declining worldwide since the early 1980s and are projected to decrease by up to 80% by the end of the 21^{st} century, leading to an amplification of the GHG-related warming of up to 1°C globally and even more at regional scale (Westervelt et al. 2015). Yet, aerosols represent the largest uncertainty in current estimates of human-driven climate change (Myhre et al. 2014) due to compounding uncertainties associated with model representations of poorly-known aerosol processes, and with the estimation of aerosol emissions.

Anthropogenic aerosols can modify the climate by scattering or absorbing solar radiation, or by changing cloud properties and precipitation processes (e.g., Twomey 1977; Albrecht 1989; Charlson et al. 1992; Ming and Ramaswamy 2009; Boucher et al. 2013, and references therein). Worldwide, aerosols have been found to play a major role in driving the late 20^{th}-century weakening of the monsoon over South Asia (Bollasina et al. 2011; Undorf et al. 2018b), East Asia (Song et al. 2014), and West Africa (Undorf et al. 2018b), as well as in modulating multidecadal variability in sea surface temperature over the North Atlantic (Booth et al. 2012; Undorf et al. 2018a). Even though North America was one of the largest contributors (along with Europe) to global aerosol emissions, particularly of sulphur dioxide (SO_2, precursor of sulphate aerosols), up to the 1980s (Hoesly et al. 2018), only a few studies have examined the climate response to anthropogenic aerosol variations over this region. Leibensperger et al. (2012) found a cooling of 0.5 to 1°C over the central and eastern US in response to increased US anthropogenic aerosols during 1970-1990. Westervelt et al. (2017) reported a considerable rainfall increase over the central and eastern US and over the North Atlantic associated with the recent SO_2 emissions decline. Yet, the physical mechanisms underlying these changes remain unclear.

The case for North America is particularly relevant as while surface tem-

perature increased worldwide, a cooling trend (the so-called "warming hole"), was observed over the southern US from the early 1950s to the mid 1970s (e.g., Robinson et al. 2002; Wang et al. 2009; Leibensperger et al. 2012). Yet, there is no consensus on the factors driving this muted warming, with some works emphasising the impact of aerosols (Leibensperger et al. 2012; Yu et al. 2014; Mascioli et al. 2017), others the role of internal climate variability (mainly through teleconnections with Pacific sea surface temperatures; Robinson et al. 2002; Wang et al. 2009; Banerjee et al. 2017) or possibly the combined effect of both (Kunkel et al. 2006; Portmann et al. 2009).

A better understanding of the regional as well as large-scale climate response to the 20^{th} century changes in North American aerosol emissions is key to achieve more robust near-future projections in this highly vulnerable region (Karmalkar et al. 2011).

1.2.3 Anthropogenic influence on regional hot extremes

In line with the current global trend, an increase in the frequency of heat waves has been experienced in Mexico and the US in the past few decades (Cueto et al. 2010; Lau and Nath 2012). These hot extremes pose detrimental impacts on human health and ecosystems and also have considerable socioeconomic costs. In the US alone, heat waves are the primary cause of weather-related human deaths, with a mortality rate close to 700 cases annually, higher than that of hurricanes, lightning, tornadoes, floods, and earthquakes combined (Luber and McGeehin 2008). Extreme heat wave activity from the 1980s to the early 2000s severely impacted the agricultural sector, leaving economic damages estimated from billions to tens of billions of US dollars per event (Kunkel et al. 1999; Ross and Lott 2003).

Increasing evidence points to a prominent role of anthropogenic influence in the recent global changes of hot extremes (Meehl et al. 2007; Bindoff et al. 2013; Su and Dong 2019b; Wang et al. 2020). However, the relative role of

each of the dominant anthropogenic drivers (e.g., GHGs and aerosols) and their associated physical processes is less known. This is a relevant issue, as the temporal evolution of GHGs and aerosols was different in the second half of the 20^{th} century, with global aerosol emissions at their peak in the 1970s, while GHGs continuously rose. Understanding these changes in hot extremes and their drivers is furthermore essential to better prepare for the expected increase in heat wave activity throughout the 21^{st} century (Pachauri et al. 2014).

A heat wave can be broadly described as a prolonged period of excessive heat that could span from a few days to several weeks and they can extend to cover large domains (e.g. half of the US). Heat waves are more frequent during the summer half of the year, when surface temperatures are higher. However, some details in the heat wave definitions vary across studies. For instance, whether to use an absolute (area-averaged) or a relative (local) threshold for identifying the hot extremes. Even though there is no general consensus on how to define a hot event, some authors agree on considering the exceedance of a local temperature threshold for identifying a HW event (e.g., Chen and Li 2017; Su and Dong 2019b; Wang et al. 2020). This has the advantage –relative to using an absolute threshold– of accounting for different types of climate, which may be necessary when analysing an extensive domain with large spatial temperature variations.

Another notable difference in the commonly used HW definitions is related to the time of day considered for the identification of the hot events. In this regard, hot extremes have been classified into three types: compound, daytime and nighttime (e.g., Chen and Li 2017; Su and Dong 2019b). This classification has proven to be useful in the study of these extreme hot events, as the impacts of each HW type and the related physical mechanisms are distinct (Chen and Li 2017; Su and Dong 2019b). For instance, daytime events are known to induce heat strokes, to increase the chance of wildfires and to damage crops (Luber and McGeehin 2008; García-Herrera et al. 2010), while the nighttime heatwaves are particularly harmful for humans, as hot nights cause body thermoregulation to

fail (Basu and Ostro 2008; Gosling et al. 2009). However, the most damaging impacts for human health are seen during the compound HWs (with hot days and nights), when the day-round hot conditions impede humans to recover at night (Basu and Ostro 2008). Most hot extreme studies in the literature have focused on the daytime heatwaves (i.e. only looking at maximum temperature). Yet, a refined categorisation is necessary for distinguishing the impacts of each of these heat wave types and their associated mechanisms.

In addition to the forcing from anthropogenic origin, the changes in HWs are the result of superimposed internal climate variability. Yet, the relative importance of the natural forcing to the heat wave variability has not been conclusively assessed. One way to achieve this involves the use of a large ensemble of simulations from a single model (all subjected to identical external forcing), where the externally forced response can be obtained by averaging across the ensemble members. The internally generated response can then be derived by subtracting the externally forced response from each ensemble member. Understanding the contribution of internal variability in the presence of external (anthropogenic) forcing in current climate extreme trends is important as internal variability is one of the largest sources of uncertainty in the near-future climate projections over North America (Deser et al. 2014; Thompson et al. 2015).

1.3 Research aim and objectives

This PhD work aims to contribute in the understanding of the mechanisms of climate variation over the Central America-Mexico-United States region, with a focus on the role of key circulation regional features and the influence of anthropogenic forcing in both mean and extreme climate.

To accomplish this aim, the objectives are as follows:

- to identify the sub-seasonal spatio-temporal evolution of the Caribbean low-level jet, a key regional summer feature, in the recent decades, and

to describe its interactions with regional and large-scale hydroclimate and circulation in a coherent dynamical portrayal

- to assess the summertime climate impact of North American anthropogenic sulphate aerosols using a state-of-the-art climate model, and to identify the underpinning physical mechanisms and teleconnection links behind the aerosol-driven changes during 1950-1975 (the period with the largest regional aerosol trends)

- to characterise changes in three independent heat wave types (compound, daytime and nighttime) over Mexico and the United States during the second half of the 20^{th} century using experiments from a large ensemble and observations; to identify the relative contribution from anthropogenic aerosols, greenhouse gases and internal variability in the heat wave recent changes and to describe their associated physical mechanisms

Each of these objectives are addressed in Chapters 2, 3 and 4, respectively.

Chapter 2

Sub-monthly evolution of the Caribbean low-level jet and its relationship with regional precipitation and atmospheric circulation

This chapter is an adapted version of a paper published in Climate Dynamics (García-Martínez and Bollasina, April 2020 [1])

2.1 Introduction

In this chapter, the summer spatial structure and sub-monthly temporal evolution of one of the key dynamical features of regional and large-scale climate in the tropical Americas, the Caribbean Low-Level Jet, is investigated by means of Extended Empirical Orthogonal Functions (EEOFs). The Caribbean 925-hPa zonal wind from the Climate Forecast System Reanalysis for the period 1979-

[1] https://doi.org/10.1007/s00382-020-05237-y

2010 is used for the analysis. In particular, we characterise the spatio-temporal evolution of the CLLJ at sub-seasonal timescale and describe its interactions with regional hydroclimate and circulation in a coherent dynamical portrayal.

The analysis takes advantage of the extended EOF technique to identify the CLLJ as the most recurring temporal series of spatial variability patterns of low-level winds over the Caribbean region, as opposed to traditional EOF-based investigations which focus only on a stationary spatial pattern. This approach is therefore more insightful in revealing the evolution of the variability pattern (from the nascent to the decay phase), thus providing novel details to be used for predictability of regional precipitation events.

The remainder of this chapter is organised as follows. Section 2.2 details data and methods used in the analysis. The spatio-temporal characteristics of the CLLJ as provided by the EEOF analysis and the links with regional hydroclimate and atmospheric circulation are documented in Section 2.3. Finally, the summary, discussion and concluding remarks follow in Section 2.4.

2.2 Data and methods

2.2.1 Data

The primary data used in this analysis consists of 6-hourly surface and upper-level variables from the Climate Forecast System Reanalysis (CFSR; Saha et al. 2010) at ∼0.3° and 0.5° horizontal resolution, respectively. Wind and precipitation from the ERA-Interim reanalysis of the European Centre For Medium-Range Weather Forecasts (Dee et al. 2011) at ∼0.7° horizontal resolution were used to corroborate the CFSR performance. Additionally, a number of other precipitation and temperature observational datasets were used for validation purposes. Observed precipitation came from various datasets to account for the different spatial resolutions and to identify potential discrepancies: the Climate Hazards Group InfraRed Precipitation with Station data (CHIRPS; Funk et al. 2015) for

the period 1981-2010 (regridded) at 0.5° resolution, the Tropical Rainfall Measurement Mission (TRMM) 3B42 dataset (Huffman et al. 2007) at 0.25° resolution for the period 1997-2010, the merged CPC Unified Precipitation for the US and station data over Mexico (USMEX, Higgins et al. 1996) at 1° resolution available from 1979 to 2009, and the Climate Prediction Center Merged Analysis of Precipitation (CMAP, Xie and Arkin 1997) at 2.5° resolution that extends from 1979 to 2010. Surface air temperature was obtained from the Berkeley Earth Surface Temperature dataset (BEST, Rohde et al. 2013) at 1° resolution for the period 1980 to 2010.

The analysis with CFSR covers the period 1979-2010 and focuses on the late-spring to mid-summer (May to July) months, in order to target the CLLJ-induced hydroclimate variability while the jet intensifies. A power spectrum of the daily 925-hPa wind over the Caribbean region (Figure 2.1) revealed a significant band of large variance from 20 to 25 days and a second peak at 40 days, highlighting the dominance of sub-seasonal wind variability in this region. The characterisation of sub-seasonal variability in this work is achieved by using pentad (five-day mean) anomalies computed from the available six-hourly CFSR fields (daily for the rest of the datasets) in order to retain sub-monthly variations while suppressing diurnal and synoptic variability.

2.2.2 Extended Empirical Orthogonal Function analysis

The CLLJ is identified by applying the extended empirical orthogonal function analysis (Weare and Nasstrom 1982) to pentad 925-hPa zonal wind anomalies over the Caribbean domain (10°-20°N, 60°-84°W), which encloses the region where the climatological CLLJ core is located. The analysis is robust for larger domains centred on the Caribbean Sea, however, by using this domain (where the correlations with the CLLJ and the 925-hPa zonal wind are largest), the CLLJ signal and its associated explained variance are maximised. Figure 2.2 shows the May to June 925-hPa wind climatology, the topography of the

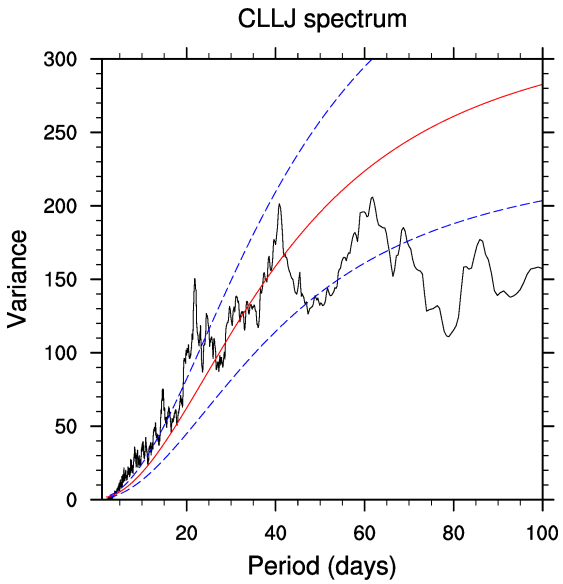

Figure 2.1: Power spectrum of the CLLJ daily index (as defined in the main text). The blue lines denote the confidence interval at 5 and 95%

region and the Caribean domain used for the EEOF enclosed in a box. The EEOF technique is a useful tool to analyse geophysical fields given their high spatio-temporal co-variability and has been successfully used in hydroclimate and teleconnection analyses recently (e.g., Weaver and Nigam 2011; Baxter and Nigam 2015; Bollasina and Messori 2018). This method extracts the most recurrent temporal series of spatial variability patterns associated with each principal component (PC), with no assumption or imposition of any specific periodicity. Besides, unlike the traditional EOF analysis, the EEOF technique does not assume spatial stationarity. However, some potential difficulties when interpreting the EEOF must be kept in mind (e.g., Chen and Harr 1993).

The spatio-temporal evolution of the CLLJ is described as the leading mode of the most recurrent five-pentad sequences of spatial patterns from EEOF, where the covariance matrix is used for the EEOF computation so that the elements with larger variance are weighted more heavily. By using a non-standardised data matrix, our results represent anomalies per unit of the respective principal component. For brevity, we will refer to these simply as anomalies throughout the manuscript. Interestingly, for the leading Caribbean mode one PC unit is close

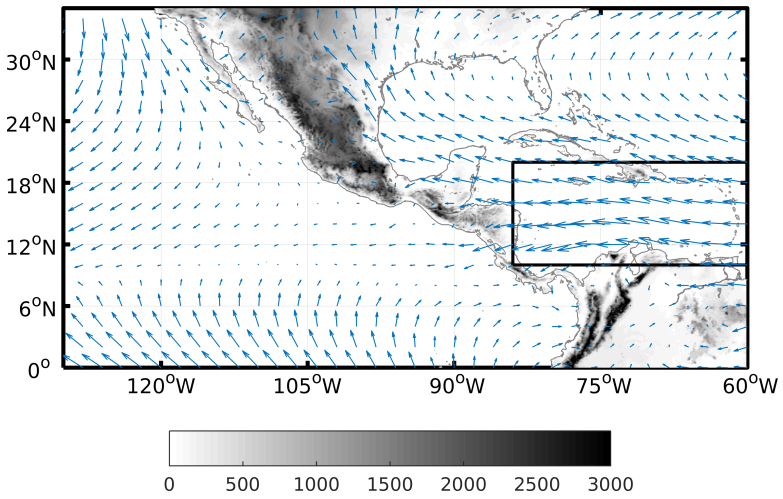

Figure 2.2: Topography of the study region [shades, m] and May-July 925-hPa wind climatology [vectors]. The Caribbean domain used for the EEOF computation is enclosed in the small box

to one standard deviation (not shown). Sensitivity tests using three-member overlapping pentads were also carried out, however, the five-pentad sampling window showed to better represent the relatively long-lived fluctuations of the CLLJ and these are therefore used in our analysis (see further discussion in Section 2.3).

The statistical links between the CLLJ and the large-scale Caribbean climate are investigated using least-squares linear regressions on the (non-standardised) PC of the first EEOF mode (PC1). These links are displayed as series of five anomaly patterns, from lag $= t - 2$ pentads (or $t - 10$ days) to lag $= t + 2$ pentads (or $t + 10$ days). The significance of the correlations between the PC1 and other meteorological variables is evaluated using a two-tailed t-test, after adjusting the degrees of freedom for every grid point to account for the large autocorrelation inherent in the time series (Santer et al. 2000). To make the interpretation easier, the principal component is set to have positive values for an easterly flow (i.e. the CLLJ flow is positive). A conventional EOF analysis was also carried out, allowing to assess the added-value of the EEOF-based analysis compared to the more traditional method (e.g., Muñoz et al. 2008). The statistical

significance of the EEOF modes is estimated in terms of the sampling error as proposed by North et al. (1982). Figure 2.A.1 shows the first four modes to be statistically significant (distinguished from the rest). Almost 55% of the total explained variance is contained within the first three modes (Figure 2.A.1).

2.3 Sub-monthly variability of the CLLJ and associated atmospheric patterns

2.3.1 Spatio-temporal evolution of the CLLJ

The leading mode of the most recurrent five-pentad sequences of 925-hPa zonal wind anomalies is shown in Figure 2.3 (shades, left panels), together with the total wind anomalies (vectors). Note that these large-scale patterns are calculated by regressing the 925-hPa wind fields on the PC1, as this is computed on the smaller Caribbean domain. The PCs of the three leading modes are shown in Figure 2.4. The explained variance by the first EEOF is 27.2%, considerably larger than the second (15.6%) and third (11.9%) EEOFs. The second and third EEOF modes represent different flavours of the CLLJ, as they also portray the strongest signal over the jet core, but have a faster temporal evolution (Figures 2.4 and 2.A.2). The EEOF wind patterns from ERA-Interim are shown in Figure 2.A.3 (left panels). Our selection of analysing the leading mode only is motivated by our focus on the variability of the CLLJ at sub-monthly scales, rather than on its supersynoptic-scale fluctuations.

The leading mode captures the key features of the CLLJ and associated wind pattern over the surrounding areas (e.g., Amador 2008; Muñoz et al. 2008): it displays the strongest signal over the CLLJ core (from 12°-16°N; 70°-80°W), and splits into a northward and a westward branch (Amador et al. 2003, 2006; Wang 2007; Amador 2008; Muñoz et al. 2008; Cook and Vizy 2010). The northward branch crosses the Gulf of Mexico and continues to be part of the western and

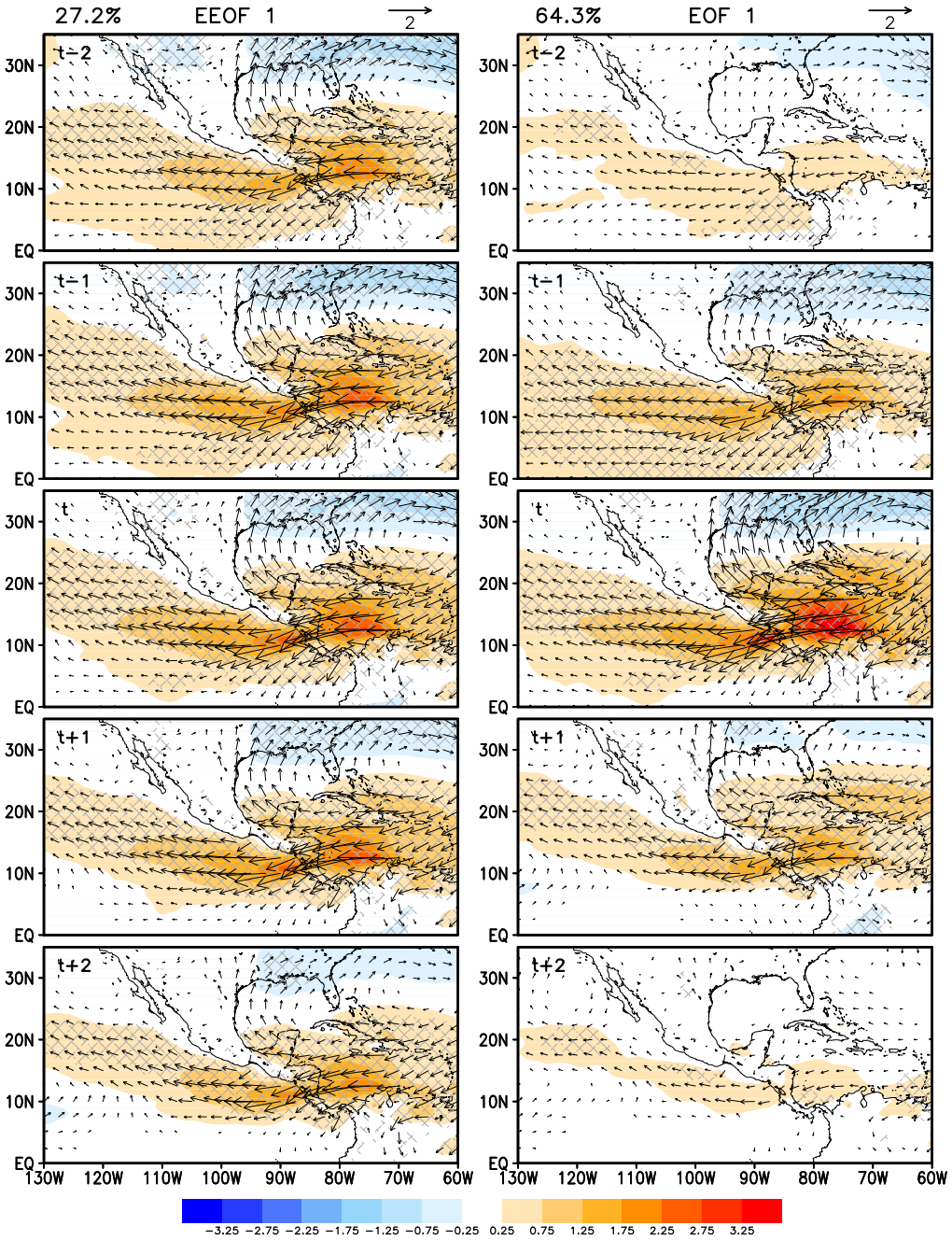

Figure 2.3: Regressed 925-hPa total winds [vectors, m s^{-1}] and its zonal component anomalies [shades, m s^{-1}] onto the PC of the first mode of variability for (left) EEOF and (right) EOF from $t = -2$ to $t = +2$ pentads. The 95% confidence interval is hatched in grey and the explained variance is shown in the top left corner of each column

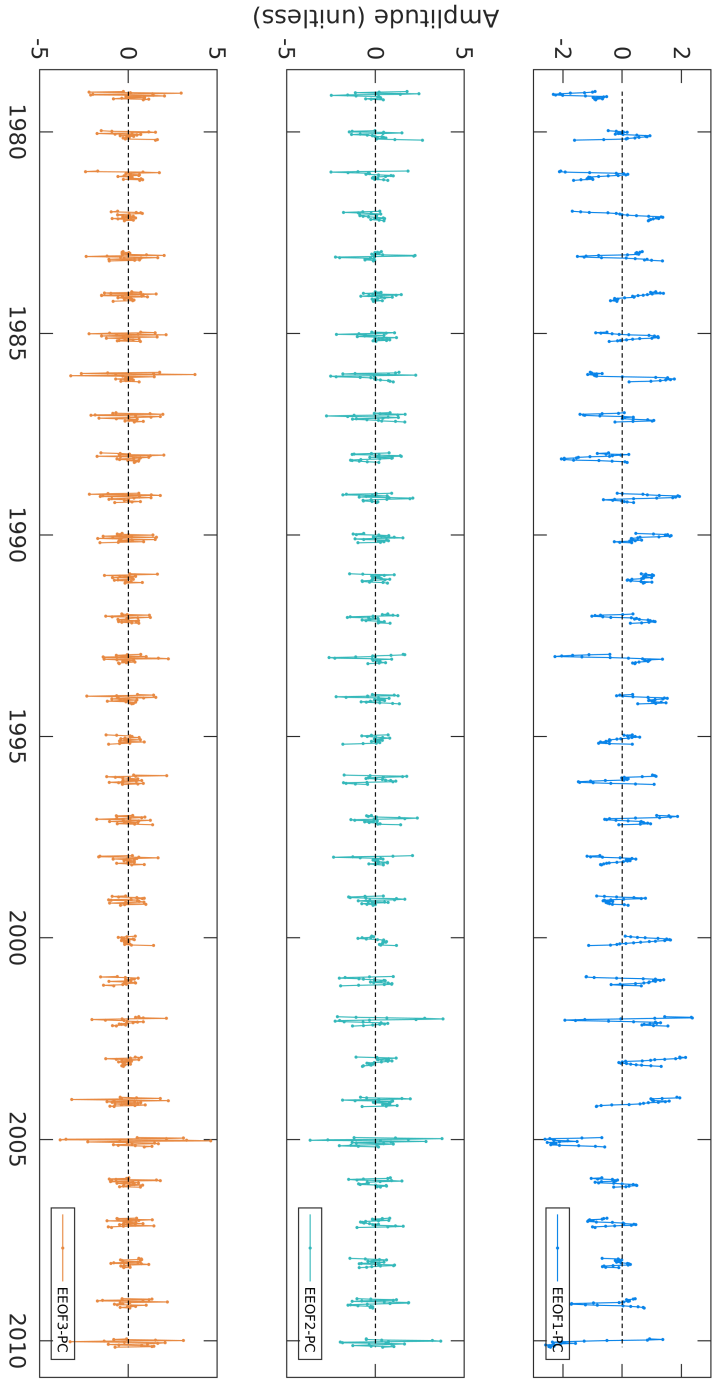

Figure 2.4: Principal components of the three leading EEOF modes of the 925-hPa zonal wind over the Caribbean

northern edges of the NASH circulation, where it merges with the GPLLJ (Mo et al. 2005), whereas the westward branch influences the tropical Pacific zonal and meridional flows over southern Mexico and the Central American coast. The mode is centred on the peak phase of the CLLJ, with spatio-temporal asymmetric growth and decay phases around lag 0 (t). In the 10°-20°N region, easterlies intensify over the Caribbean (up to 2.5 m s^{-1}) from $t-2$ to t (∼10 days before the maximum), and then decrease gradually in the following pentads (from $t+1$ to $t+2$). On the Pacific side, the wind evolves similarly, with maxima anomalies of up to 2 m s^{-1} off the Nicaraguan coast (the Papagayo jet), suggesting a simultaneous (within a five-day period) wind response to CLLJ variability there. However, as the CLLJ evolves, the winds confined to the southeast quadrant of the domain (0°-12°N, 100°-130°W), albeit relatively weak, exhibit a marked direction change: from easterlies at $t-2$ to southerlies and westerlies (converging at 120°-125°W) at $t+2$. This modal evolution exerts a strong modulation on the precipitation pattern over the tropical Pacific (more details in Section 2.3.2). In contrast to the westward branch, it is noteworthy that the magnitude of the northward branch weakens gradually throughout the five pentads. This difference, an important and yet unnoticed dynamical feature of the CLLJ, suggests a lagged relationship between the two branches and hints at different underlying controlling mechanisms.

An appreciation of the benefits of using the EEOF analysis instead of the conventional EOF can be appraised by comparing the left and right panels of Figure 2.3, the latter showing the five-pentad evolution of the 925-hPa wind anomalies obtained from lead/lag regressions on the EOF1-PC. The larger variance explained by the EOF1 (64.3%) compared to that of the EEOF1 (27.2%) is not surprising, since using a series of five spatial patterns instead of one in the covariance matrix increases the variance (Bollasina and Messori 2018). While the mature phase (lag 0) spatial pattern is very similar between both methods, the lead/lag EOF regressions do not capture the wind evolution at sub-monthly

timescale (from its nascent to its decay phase) entirely, but, instead, depict a strong dominance of higher-frequency (supersynoptic) variability.

This is supported by comparing the temporal autocorrelation of the first PC from both EEOF and EOF analyses, which provides an estimate of the timescale of the most recurrent mode of CLLJ summer variability (Figure 2.5). The EEOF1-PC displays a longer temporal autocorrelation than that of EOF1-PC. The latter falls off rapidly beyond ±1 pentad, indicating a large contribution of supersynoptic-scale variability. The former is longer-lived, with an event duration of 6 to 8 pentads as estimated from the e^{-1} threshold. This is consistent with the EEOF's ability to capture the whole evolution of a spatial pattern from its nascent to decay phases, which is conversely absent in its EOF approximation via lead/lag regressions. The autocorrelation of the second and third EEOF PCs follow a similar behaviour as EOF1-PC, dropping down rapidly after the first pentad. This further indicates that these two modes are, too, modulated by supersynoptic-scale processes. The autocorrelation of the CLLJ index (defined as the negative of the 925-hPa zonal wind anomalies averaged over 12°-16°N and 70°-80°W as in Wang 2007) is also included in Figure 2.5 for reference. As expected, the CLLJ index and the EOF1-PC timeseries are quite similar, and both show the supersynoptic variations of the CLLJ, while the EEOF1-PC captures the jet fluctuations at sub-monthly scale.

2.3.2 Surface anomalies associated with the CLLJ

The main role of the CLLJ in regional climate variability is to act as a moisture conveyor belt, by advecting moisture from the warm Caribbean Sea towards the Pacific and across the Gulf of Mexico (Durán-Quesada et al. 2010; Amador et al. 2016) and thus modulating precipitation, temperature and circulation patterns in the region. Precipitation (from CFSR, USMEX and CMAP), vertically-integrated stationary moisture fluxes, surface skin temperature and sea level pressure anomalies associated with the sub-monthly variability of the CLLJ are

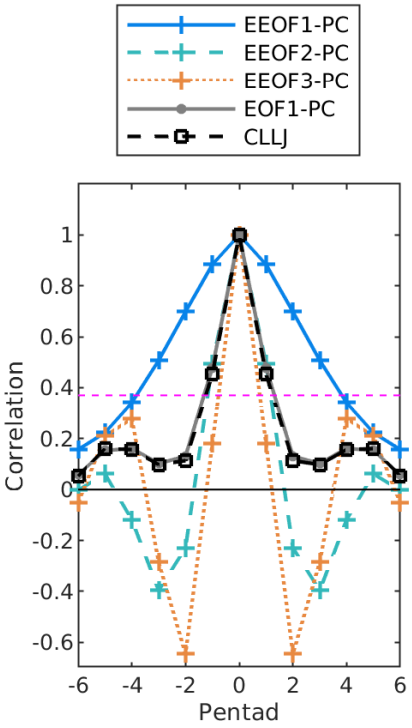

Figure 2.5: Autocorrelation of the principal components associated with the first three modes of pentad 925-hPa zonal wind variability over the Caribbean, for the extended EOF: EEOF1-PC (blue), EEOF2-PC (green) and EEOF3-PC (orange), and by the traditional EOF: EOF1-PC (grey). The autocorrelation of the CLLJ index (dashed black curve) is also shown for reference. The e^{-1} threshold is indicated with a dashed magenta line

displayed in Figures 2.6 to 2.8, in terms of linear regressions on the EEOF1-PC. These are shown for the entire five-pentad sequence (lags -2 to +2) in order to uncover potential precursor links with the CLLJ. The linear regressions of ERA-Interim, CHIRPS and TRMM rainfall, CFSR evaporation and BEST surface air temperature regressions are shown in the supplementary material (Figures 2.A.3, 2.A.4 and 2.A.5).

The most noticeable characteristic of the precipitation pattern is the nearly-zonal oceanic dipole featuring drier conditions over a large region extending from the subtropical Atlantic Ocean across the Caribbean to the Pacific coast of Central America (although excluding a smaller-scale region of intense rainfall off the coasts

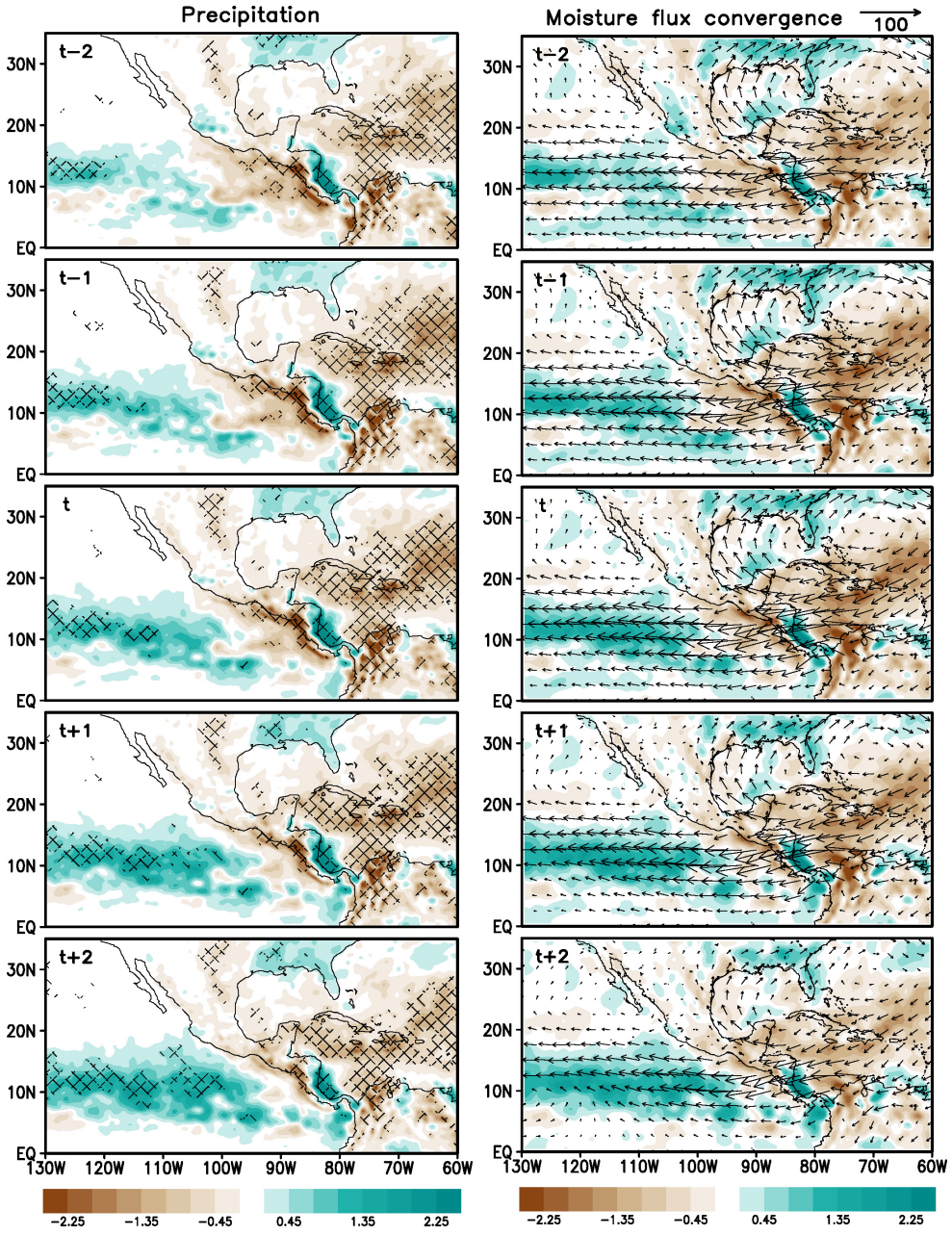

Figure 2.6: Regressed (left) CFSR precipitation [shades, mm day^{-1}] and (right) vertically-integrated stationary moisture flux anomalies [vectors, kg m^{-1} s^{-1}] and its convergence [shades, mm day^{-1}] onto the EEOF1-PC from $t = -2$ to $t = +2$ pentads. The 95% confidence interval is hatched in the precipitation regressions. Shading starts from $\pm$ 0.15 mm day^{-1} and has increments of 0.3 mm day^{-1}

of Nicaragua and Costa Rica), and excess rainfall over a zonally-elongated band in the Pacific between 9°-15°N (Figures 2.6 and 2.7). Interestingly, the two anomalies exhibit a different temporal evolution: the former is geographically stationary and has peak negative values at lag 0, concurrently with the temporal evolution of the CLLJ and of the divergence area upstream of the jet core (e.g., Whyte et al. 2008; Martinez et al. 2019). By contrast, the latter anomaly gradually increases expanding eastward while the CLLJ evolves, to reach maximum positive values at $t + 2$. Note that this progression is accompanied by a simultaneous weakening and shrinking of the precipitation deficit on the Pacific slope of Central America and the adjacent eastern tropical Pacific. Both features are largely associated with the gradual clockwise turning of the eastern tropical Pacific winds that generate meridional convergence of moist winds south of 10°N (not shown), favouring positive rainfall anomalies throughout the five-pentad sequence (more details in Section 2.3.3). Near the Pacific coast, reduced upwelling and ensuing coupled feedbacks with SSTs (Figure 2.8) and evaporation (Figure 2.A.5) contribute to the weakening of the dry anomaly (Magaña et al. 1999; Xie et al. 2005). A positive precipitation anomaly of up to 0.8 mm day^{-1} is also evident over the southeastern US: as the jet evolves, the core of the anomaly displays a progressive southeastward displacement with negligible changes in its magnitude. This indicates a link between the CLLJ and US hydroclimate, and is consistent with the findings of Weaver and Nigam (2011) on the inverse relationship between GPLLJ intensity and precipitation anomalies over the southeastern US at sub-monthly timescale. A weaker GPLLJ leads to larger positive rainfall anomalies closer to the southern coast of the US, from Louisiana to Florida.

Albeit spatially confined, a precipitation dipole develops across Central America: along the Caribbean coast of Central America and the western Caribbean Sea, increased rainfall associated with induced ascent at the CLLJ exit region, and drying to the west and off the Pacific coast because of strong subsidence associated with the CLLJ intensification (Figure 2.6; Hidalgo et al. 2015).

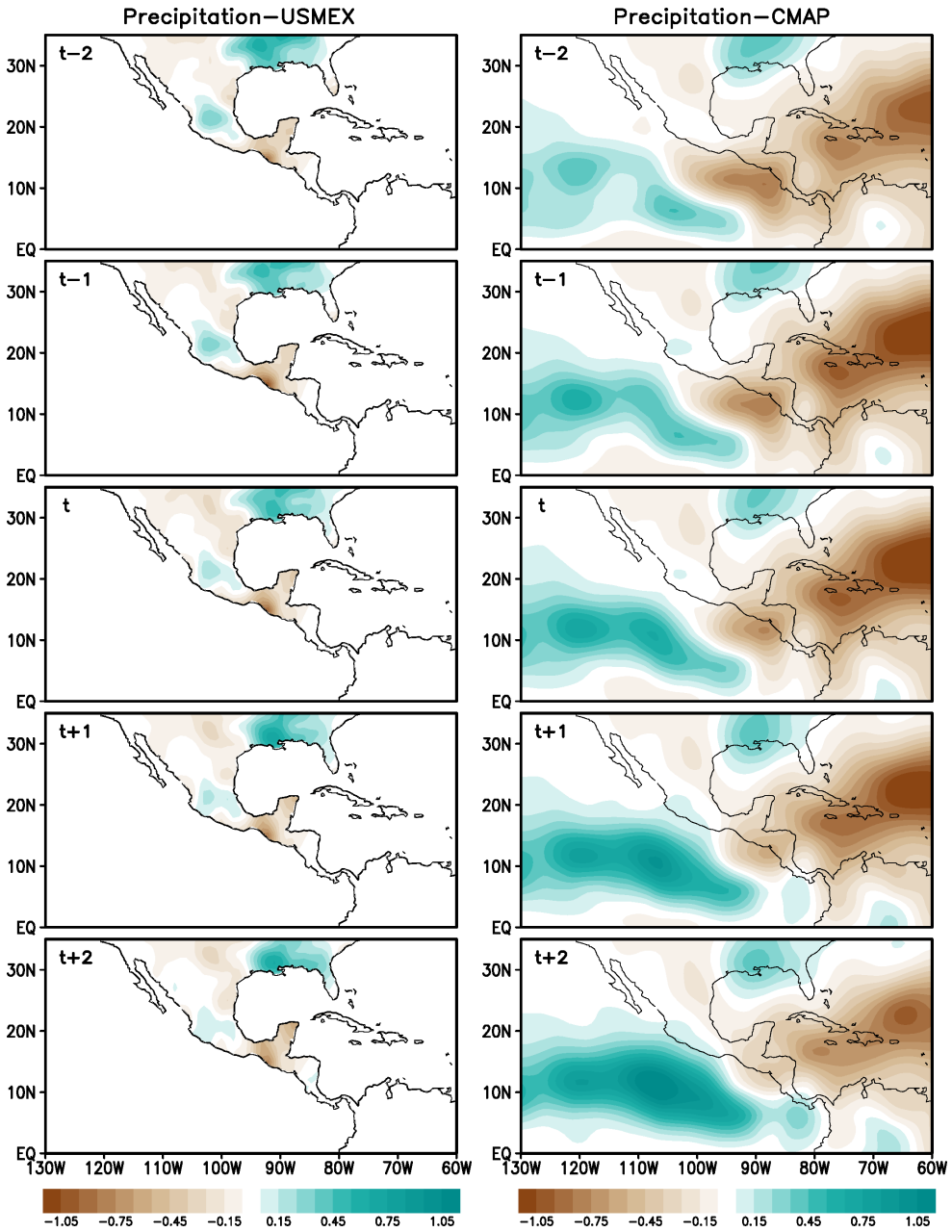

Figure 2.7: Regressed (left) 1979-2009 USMEX and (right) 1979-2010 CMAP precipitation [shades, mm day^{-1}] anomalies onto the EEOF1-PC from $t = -2$ to $t = +2$ pentads. Shading starts from $\pm$ 0.05 mm day^{-1} and has increments of 0.1 mm day^{-1}

Mountain gaps across Central America allow the passage of the CLLJ flow, linking the Caribbean and eastern tropical Pacific atmospheric circulation (e.g.,

Magaña and Caetano 2005; Xie et al. 2005; Romero-Centeno et al. 2007; Amador 2008; Herrera et al. 2015). Northeasterly wind anomalies occur over the mountain gaps of Tehuantepec (southern Mexico), Papagayo (west Costa Rica) and Panama, with peak values at lag 0. Of the three, the Papagayo jet exhibits the largest anomalies (up to 3 m s^{-1}). These gap winds are a fundamental mechanism for cross-basin moisture transport (Magaña and Caetano 2005; Durán-Quesada et al. 2010) and for the formation of ocean eddies along the eastern tropical Pacific and the upwelling associated with the Costa Rica Dome, a region of high biological productivity (Fiedler 2002).

The link between atmospheric circulation and precipitation can be further appreciated by analysing the spatio-temporal evolution of vertically-integrated moisture fluxes. The right column in Figure 2.6 displays the vertically-integrated stationary moisture transport and its convergence; note that the contribution of the transient component (in time) of these fluxes is generally of minor importance (Martinez et al. 2019). Moisture transport from the oceans and its convergence is crucial to generating precipitation in the western Caribbean region (e.g., Amador 1998; Wang 2007; Durán-Quesada et al. 2010; Hidalgo et al. 2015; Martinez et al. 2019). Moisture convergence anomalies show a remarkable similarity in pattern and magnitude to the precipitation ones, attesting for the secondary contribution of evaporation in the formation of the precipitation anomalies described above. In particular, the role of meridional moisture flux convergence over the tropical Pacific (south of 10°N) in modulating the rainfall maximum there is evident.

The surface temperature regression (Figure 2.8) also shows a coherent large-scale pattern and evolution. The initial extensive warm anomaly across the southern US and northern Mexico, progressively weakens and reduces in extent, while an area of increasing cold anomalies moves over the southeastern US. Interestingly, the wind regressions and the anomalous westerlies suggests a possible contribution of orographically-forced descent across the Rockies to the generation of the positive warmer temperature anomaly. Note that the warmer

SSTs along the Pacific coast, while linked to the positive temperature anomaly over north and central Mexico, exhibit an opposite evolution: initially confined to a narrow region offshore the Mexican coast, the anomaly extends westward and grows. Over the Caribbean Sea, a zonally-elongated area of cold SSTs, gradually amplifies while spreading westward across the Caribbean region, with peak values at lag $t+2$. The location of the largest cooling, south of the CLLJ maximum, and its rapid growth at negative lags are indicative of a strong dynamical modulation by the CLLJ via evaporative cooling and associated Ekman upwelling. Yet, the latter alone cannot fully account for the further SST cooling at positive lags, when the CLLJ actually weakens. Along the southern coast, strong upwelling forced by the CLLJ intensification takes place, which brings cold water to the surface (Inoue et al. 2002; Andrade and Barton 2005; Lee et al. 2007; Jouanno and Sheinbaum 2013). Two important upwelling systems identified as the Guajira (12°N, 72°W, Andrade and Barton 2005) and Margarita (10°N, 64°W) upwellings are well captured by the EEOF1-PC. Offshore, Ekman transport, vertical mixing and in lees degree (but equally important) vertical advection contribute to the south Caribbean cooling, although this last one is limited to a radius of 200-300 km downstream the upwelling area (Jouanno and Sheinbaum 2013). Finally, simultaneously to oceanic changes, land temperatures over Central America also progressively turn to negative values as the CLLJ evolves.

The pattern of sea level pressure (SLP, Figure 2.8) anomalies exhibits a quadrupole structure, with positive centres of action located over the subtropical portions of the North Atlantic and the eastern Pacific, and negative poles over the southern US and along the north equatorial Pacific. The predominant Atlantic anticyclonic anomaly, with peak magnitude at lag 0, corresponds to a strengthening and successive decline of the NASH; the anomalous low pressure system over the south-central US, decreases progressively from $t-2$ to $t+2$ (over a 25-day period); the Eastern Pacific anticylone to the west side of the Baja California peninsula weakens along the five-pentad sequence and; the intensified

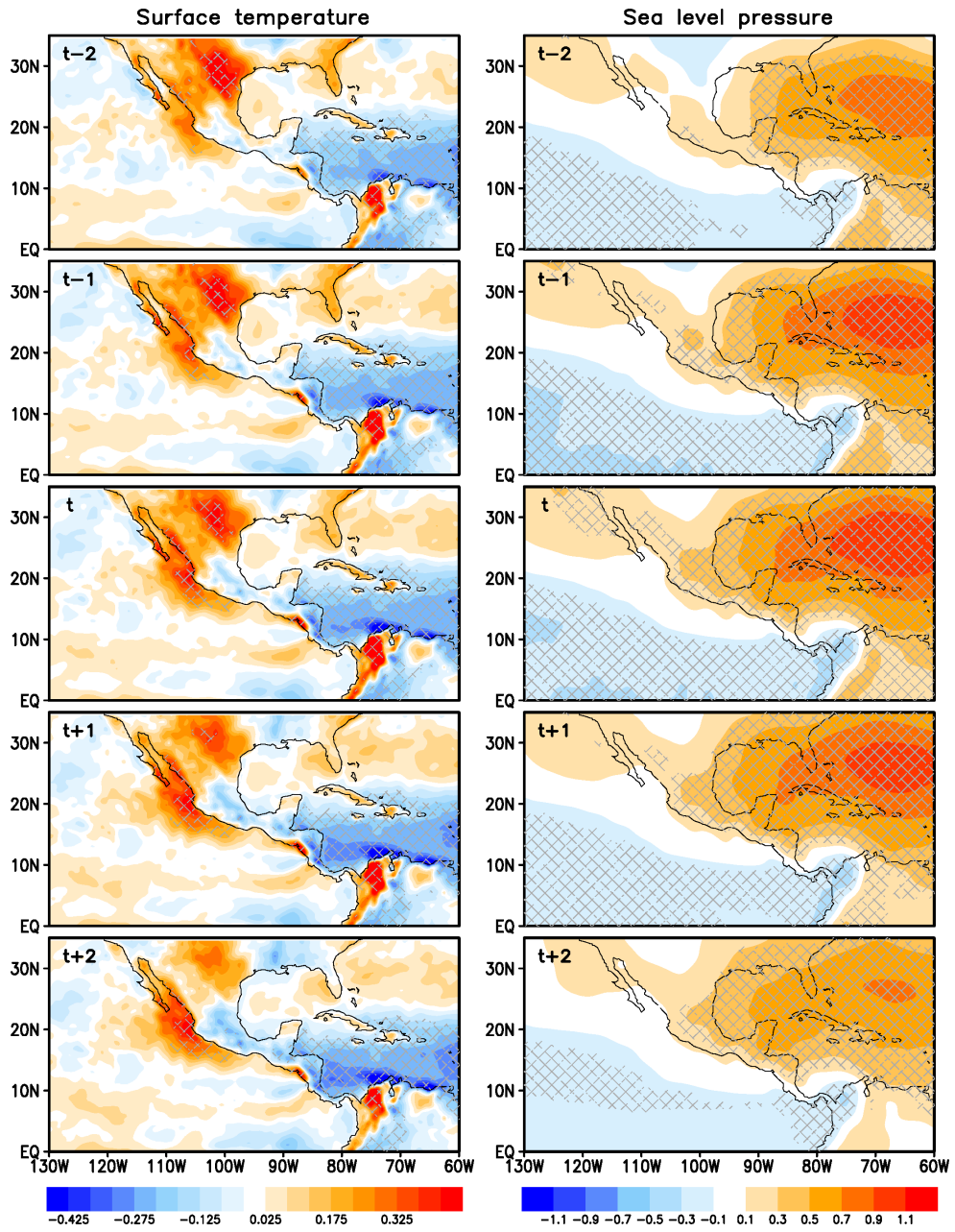

Figure 2.8: Regressed (left) surface skin temperature [°C] and (right) sea level pressure anomalies [hPa] onto the EEOF1-PC from $t = -2$ to $t = +2$ pentads. The 95% confidence interval is hatched

near-equatorial trough extends throughout the tropical Pacific with the highest anomalies (-0.6 hPa) occurring at $t-1$ (5 days before the CLLJ maximum). The

interaction among these pressure systems largely determines the wind fluctuations in the region.

The NASH and the low pressure system over the central US evolve in concert. In early and mid-summer, when solar radiation is maximum over the northern hemisphere, the surface heating over the central US landmass allows the formation of a thermal low that strengthens, along with subsidence over the adjacent subtropical North Atlantic and Pacific oceans (Small et al. 2007). By mid-summer, the thermal low weakens, allowing the NASH to intrude farther west and thus intensifying the CLLJ (Amador et al. 2006; Small et al. 2007; Wang 2007; Romero-Centeno et al. 2007; Cook and Vizy 2010). In the EEOF analysis, the interaction between the NASH and the thermal low helps explain the northward branch intensity fluctuations. A stronger SLP gradient between these two systems is observed in the initial pentad $t-2$ over northeastern Mexico and south-central US, resulting in a strong northerly flow. The SLP gradient then decreases gradually towards the last pentad $t+2$, weakening the northward branch flow. To the west, consistent flow from the Eastern Pacific anticyclone weakens along with the US thermal low.

The pressure gradient between the Caribbean and the eastern Pacific region, on the other hand, evolves in a different way. The positive NASH anomalies (that peak at lag 0), in combination with constant negative SLP anomalies over the tropical Pacific, lead to an enhanced SLP gradient (driven by the Caribbean) over Central America. As a result, the CLLJ reaches its strongest phase during the central pentad t.

2.3.3 Three-dimensional atmospheric circulation

In order to relate surface climate anomalies with the upper-level atmospheric circulation, Figure 2.9 shows the vertical cross-section of regressed vertical velocity and zonal wind averaged between 12°-16°N, where the core of the CLLJ is located. A direct vertical cell is observed between the low-level easterly flow of the CLLJ

and opposite upper-tropospheric westerlies, along with intense subsidence (up to 16 hPa day^{-1}) at the jet entrance (70°-75°W, eastern Caribbean) and strong ascent across the whole troposphere (up to -24 hPa day^{-1}) at the jet exit (80°-85°W, western Caribbean), where deep convection develops. The importance of this cell as a key dynamical feature over the Caribbean and adjacent regions has been highlighted in previous works (Amador 1998; Magaña and Caetano 2005; Andrade and Barton 2013; Herrera et al. 2015; Hidalgo et al. 2015). The subsidence at the jet entrance is amplified in the layers below 500 hPa, while the upward motion at the jet exit extends throughout the troposphere. The strength of this cell varies concurrently with the magnitude of the CLLJ: it intensifies during the CLLJ development phase (from $t-2$ to t) and weakens later on; also, as expected by the approximate balance between diabatic heating and vertical motion in the tropics, regions of stronger ascent correspond to rainfall maxima.

In-phase cross-basin links take place over the Central American mountain ranges, with the easterly mid-tropospheric flow from the Caribbean subsiding along the Pacific slope of Central America (Figure 2.9). In the eastern tropical Pacific (east of 95°W), in accordance with the evolution of precipitation anomalies described above (see Figure 2.6), a gradual intensification of upward motion occurs throughout the five-pentad sequence (Figure 2.9). Interestingly, this is associated with a westerly upper-tropospheric flow linking the Pacific to the Atlantic basin, where it reinforces the regional circulation cell and increases the upper-tropospheric subsidence in the western Caribbean (70°-80°W). This suggests an important role of remote forcing (i.e. originating outside of the Caribbean region, in this case the tropical Pacific) in modulating the evolution of the CLLJ and of the local rainfall pattern (e.g., Small et al. 2007).

A broader dynamical context for the CLLJ evolution discussed above can be achieved by examining the spatio-temporal characteristics of the upper-tropospheric circulation. To this end, 200-hPa velocity potential and associated divergent circulation are shown in Figure 2.10. The initial divergent outflow

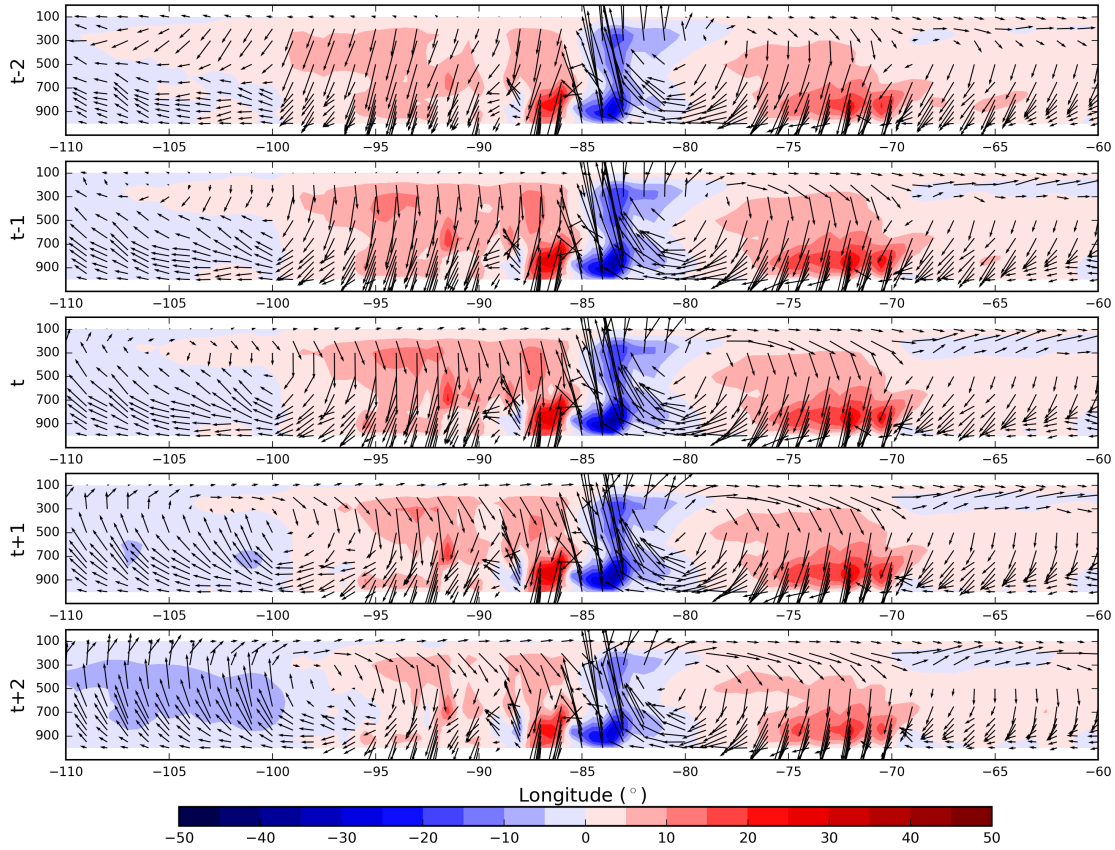

Figure 2.9: Longitude-height cross-sections of regressed vertical velocity [shades, hPa day^{-1}] and zonal wind anomalies [m s^{-1}] averaged over the CLLJ core latitudinal band (12°-16°N) onto the EEOF1-PC from $t = -2$ to $t = +2$ pentads

emanating from the southern US and the central Pacific, coincident with positive diabatic heating anomalies and excess rainfall, stand out. The southeastward and eastward flow, respectively, converges and subsides in the subtropical western Atlantic, where it reinforces the surface anticyclone. A secondary, yet important, dipole is noticeable in the CLLJ region, with divergence at its exit, the wet Caribbean slope of Central America, and convergence at the jet entrance. As the CLLJ develops and evolves, the Pacific center gradually moves southeastward toward the equator and deepens, consistently with the evolution of rainfall anomalies there, and the divergent circulation features a prominent zonal westerly flow from the Pacific to the subtropical eastern Atlantic.

The 200-hPa streamfunction anomalies associated with the variations of the

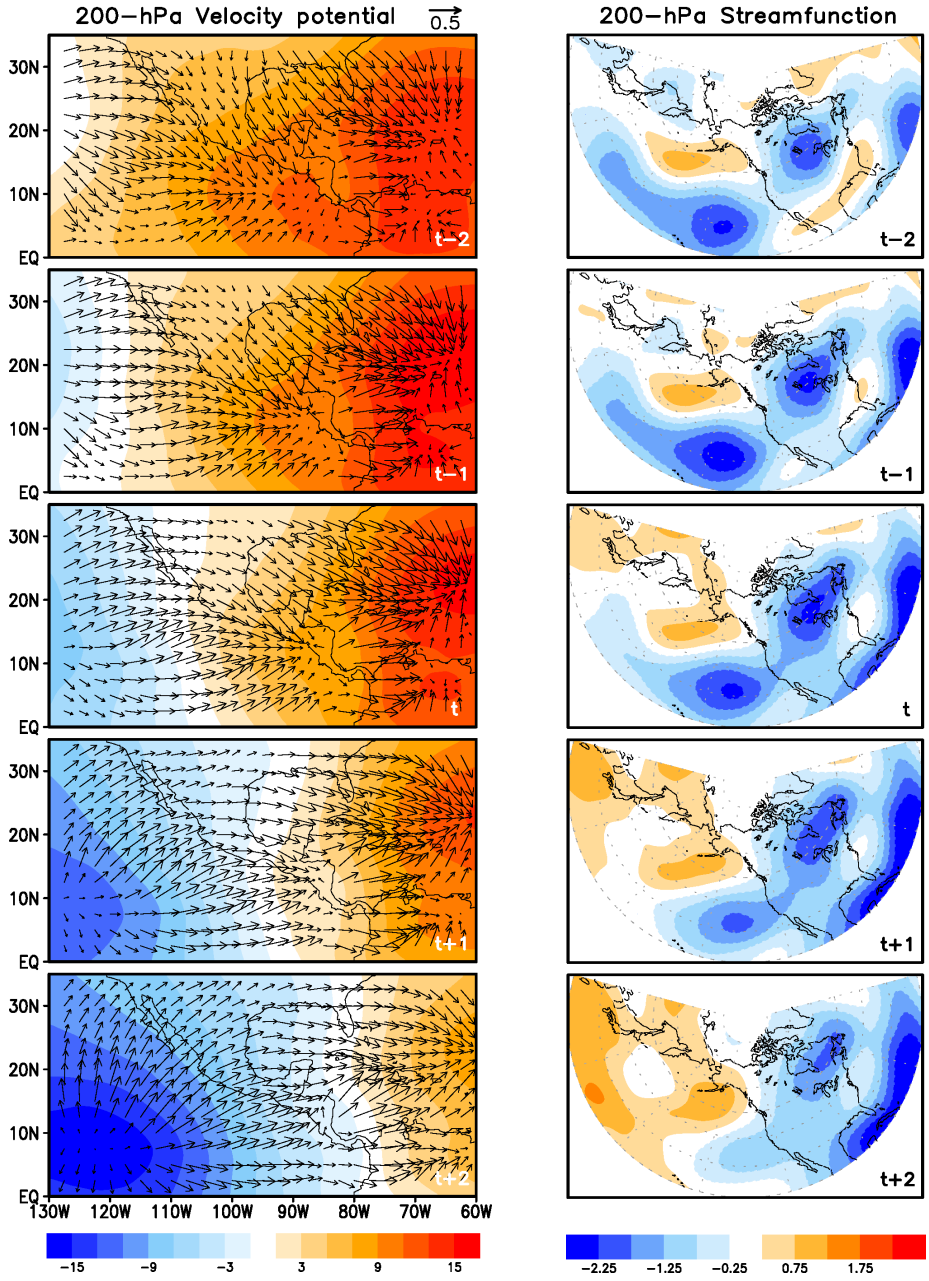

Figure 2.10: (left) Velocity potential [shades, 10^5 m^2 s^{-1}], divergent circulation [vectors, m s^{-1}] and (right) streamfunction [shades, 10^6 m^2 s^{-1}] of the 200-hPa regressed wind anomalies onto the EEOF1-PC from $t = -2$ to $t = +2$ pentads. Positive streamfunction values indicate anticyclonic circulation

CLLJ (Figure 2.10) display a large-scale coherent midlatitude pattern similar to that of the underlying sea-level pressure anomalies in an approximate equivalent

barotropic structure, despite the weaker upper-tropospheric anticyclone over the Caribbean. Note this level is optimal to examine the link between the CLLJ and tropical-extratropical teleconnection patterns (e.g., Weaver and Nigam 2008). The initial streamfunction pattern is dominated by a widespread deep trough over central northern America, bounded by anticyclonic anomalies over the eastern North Pacific and over the northern Gulf of Mexico. Both the Pacific anticyclone and the North American trough grow to lag -1 and lag 0, respectively. This pattern resembles the upper-tropospheric tripole associated with the CLLJ noted by Muñoz and Enfield (2011), albeit in terms of interannual jet fluctuations; a similar structure was also identified by Weaver and Nigam (2011) as precursor to the northward migration of the GPLLJ. This suggests the possible influence of extratropical hemispheric-wide waves in the atmospheric circulation on the CLLJ intensification. In particular, the eastern edge of the Pacific anticyclone is associated with anomalous westerlies impinging on the Rockies and subsequent downstream subsidence, suggesting a forcing mechanism on the thermal low. Conversely, the CLLJ decay phase appears to be accompanied by larger tropical anomalies, in both the eastern Pacific and Atlantic Oceans, consistently with the outflow and inflow centres in the 200-hPa divergent circulation.

2.3.4 Sensitivity analysis to the MJO and ENSO

One may ask whether the CLLJ sub-monthly characterisation discussed above, and particularly the Pacific branch, may be even partially linked to the two most significant modes of coupled variability of the region: the Madden-Julian Oscillation and El Niño Southern Oscillation (ENSO). The MJO is the largest contributor of intraseasonal variability in the tropics and although its effects are stronger over the western tropical Pacific, its influence has also been reported in other regions of the globe (Zhang 2013 and references therein). Over the eastern tropical Pacific, the MJO was found to modulate the intensity and number of tropical cyclones (Maloney and Hartmann 2000). Barlow and Salstein

(2006) reported an increase in local rainfall totals on the Pacific coast of Mexico and Central America due to active phases of the MJO. More recently, Martin and Schumacher (2011) suggested an intraseasonal modulation of the CLLJ and rainfall patterns in Mexico and Central America by the MJO throughout the year. However, the possible summer connections between the CLLJ and the MJO, and their dynamical mechanisms at sub-monthly timescale are yet to be explored.

Fluctuations in the intensity of the CLLJ have been suggested to be modulated by the SST gradient between the tropical Pacific and the Caribbean Sea-Atlantic domain (Enfield and Alfaro 1999; Small et al. 2007; Wang 2007; Martinez-Sanchez and Cavazos 2014; Fuentes-Franco et al. 2015), although this is a current debate (e.g., Maldonado et al. 2017). The CLLJ has been observed to strengthen when the inter-basin SST gradient increases (with a warmer-Pacific and cooler-Atlantic configuration), however, Whyte et al. 2008 found out that the spatial pattern of the CLLJ intensification depends on which specific basin is primarily modulating the temperature gradient. The CLLJ intensification during warm ENSO events has been related to an anomalous southward displacement of the ITCZ (Amador 2008; Hidalgo et al. 2015) and to the westward intrusion and strengthening of the NASH (Romero-Centeno et al. 2003), and has been consistently found in several studies using monthly-to-seasonal data (Romero-Centeno et al. 2003; Amador 2008; Whyte et al. 2008; Hidalgo et al. 2015). Our focus here is on the summer ENSO-CLLJ pentad-evolving relationship.

To isolate the MJO signal, MJO-related anomalies were calculated by; 1) linearly regressing circulation and surface climate variables on the MJO real-time multivariate indices 1 and 2 (RMM1 and RMM2, Wheeler and Hendon 2004); 2) multiplying the spatial patterns obtained in step 1 by the respective MJO index, and subtracting both fields from the original anomalies; 3) repeating the steps described above for the original fields (i.e. an EEOF analysis of the no-MJO 925-hPa zonal wind and subsequent regressions on its leading PC). To a first-order approximation and to the extent by which the MJO influence can be assumed to

be linear, the new patterns should have the MJO signal removed (e.g., Baxter and Nigam 2014). A similar method was used to remove the ENSO signal (e.g., Kucharski et al. 2009). The no-MJO and no-ENSO regressed fields were then removed from the original (all-signals) data to show the isolated effect of these two global modes. The RMM1 and RMM2 series are available online from the Bureau of Meteorology of the Australian Government. For representing the ENSO signal, the Niño 3.4 index, computed from CFSR data, was used. The MJO and ENSO regressed patterns of 925-hPa wind, precipitation and surface temperature are shown in Figure 2.11.

The explained variance of the EEOFs with no MJO and no ENSO signals is 16.0% and 16.3%, respectively, approximately 11% lower than the all-signals EEOF in both cases. It is interesting to notice that both the MJO and ENSO have similar imprint on sub-monthly climate variability in the broader Caribbean region. Over the Caribbean-Atlantic region, their influence is manifested as an intensification of the CLLJ throughout the five-pentad sequence and lengthening of its life cycle (Figure 2.11), which in turn extends the temporal response of air-sea interactions. The CLLJ reaches its highest anomalies between $t + 1$ and $t + 2$, 5 to 10 days later than in the all-signals EEOF analysis. In southern Mexico, northern Central America and the adjacent tropical Pacific, negative rainfall anomalies increase throughout the CLLJ intensification (from $t - 2$ to $t + 2$). Over the tropical Pacific, a gradual intensification of the easterly winds associated with these modes of variability, contributes to a progressive increase in rainfall anomalies there. The Papagayo and the Panama gap winds are also strengthened by the MJO and ENSO (Figure 2.11). Altogether, ENSO-related anomalies are weaker than the MJO ones.

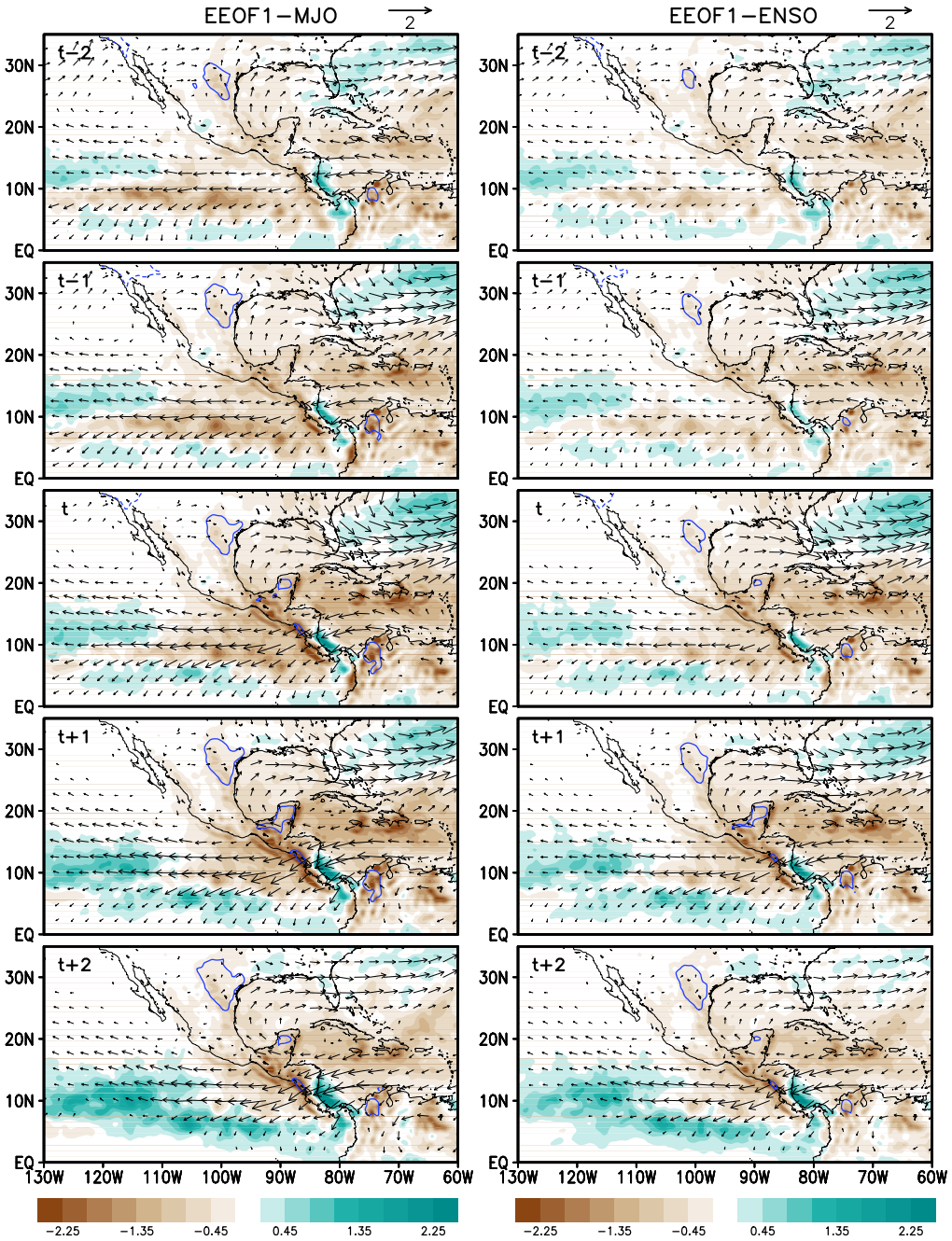

Figure 2.11: Regressed precipitation [shades, mm day^{-1}], surface skin temperature [contours, °C] and 925-hPa total wind anomalies [vectors, m s^{-1}] onto the EEOF1-PC for the data with (left) the MJO and (right) ENSO signals isolated from $t = -2$ to $t = +2$ pentads. Dashed (continuous) contours indicate the -0.3°C (+0.3 °C) isotherm. Shading starts from ± 0.15 mm day^{-1}

2.4 Summary, discussion and conclusions

The CLLJ is an important dynamical feature and key modulator of Mexican and Central American hydroclimate as it controls the transport of moisture from the Caribbean Sea to the nearby land areas, where it contributes to generating the 60% of annual precipitation received during the summer months. While seasonal and interannual characteristics of the CLLJ and related regional hydroclimate links have been extensively discussed (e.g., Amador et al. 2006; Romero-Centeno et al. 2007; Wang 2007; Amador 2008; Muñoz et al. 2008; Cook and Vizy 2010; Herrera et al. 2015; Hidalgo et al. 2015), its intraseasonal variability has received much less attention. Additionally, existing studies assumed stationarity of the spatial pattern of the winds by, for example, describing the CLLJ in terms of an area-average circulation index (e.g., Wang 2007; Muñoz et al. 2008). Even more importantly, Caribbean hydroclimate variability is modulated by a variety of high-frequency coupled land-ocean-atmosphere processes and feedbacks whose links can be aliased in seasonal-based investigations.

In this study we used the extended EOF analysis to characterise the prominent CLLJ spatio-temporal variability patterns, which allows to effectively build a dynamical portrayal of its climate links in the broader Caribbean region as well as to pinpoint precursor relationships. An schematic depicting the main circulation features as found by the EEOF analysis is shown in Figure 2.12. Notably, the signature of most of these dominant circulation features has also been identified in monthly-to-seasonal analyses (Amador 1998; Amador et al. 2006; Amador 2008; Hidalgo et al. 2015). Even though a traditional EOF analysis is also able to identify the CLLJ as the leading mode of Caribbean wind variability, it does not capture the intrinsic full wind evolution and is therefore unable to highlight non-concurrent wind-hydroclimate links.

The dynamical characterisation portrayed by the EEOF analysis reveals important links between the CLLJ and regional precipitation, temperature and circulation anomalies as well as the associated temporal phasing, including

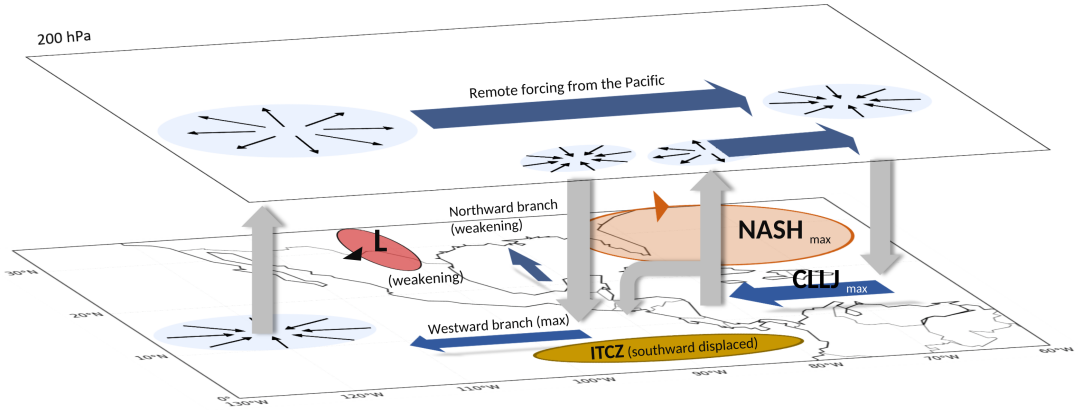

Figure 2.12: Schematic of the dominant circulation features associated with the CLLJ summer intensification ($t-2$ to t in the EEOF analysis). Blue arrows represent horizontal winds at 925 and 200 hPa and grey arrows vertical motion. Centres of convergence and divergence are indicated by blue circles and the corresponding circulation in black arrows. A thermal low (L) in northwest Mexico-central US is shown by a red ellipse. The North Atlantic Subtropical High is coloured in orange and the ITCZ in yellow. During the CLLJ weakening (t to $t+2$), the intensity of these related circulation features is reduced

the existence of key relationships with antecedent and lagged anomalies (i.e. anomalous thermal low over the Southern US and the Caribbean SST response, respectively), the interaction of the jet with large-scale dynamical circulation features (e.g., the NASH and its westward progression), and the role of inter-basin links between the Atlantic and the Pacific Oceans, which in turn feedback on the CLLJ evolution. The full nature of these relationships was only partially appreciated, if not overlooked, in previous works where the use of a stationary pattern of the CLLJ did not allow to build a unitary mechanistic picture. Notably, the EEOF-based findings provide a framework bridging conventional analyses at monthly/seasonal scale to the fundamental high-frequency variability of the CLLJ.

In addition to forcings of regional origin, wider-scale climate variability modes, namely the MJO and ENSO, are important contributors to the atmospheric circulation changes over the Caribbean. Their influence is manifested as an intensification of the CLLJ throughout the five-pentad sequence and a lengthening

of its life cycle (by up to 10 days), which in turn extends the temporal response of the air-sea interactions.

An EEOF analysis using the ERA-Interim 925-hPa winds showed similar patterns and temporal evolution over most of the domain with those of the CFSR, except over the Pacific Ocean, where the eastward branch is confined to the eastern tropical Pacific (Figure 2.A.3). Most of the precipitation and temperature features found in the CFSR are also present in the other analysed datasets (Figures 2.7, 2.A.3, 2.A.4 and 2.A.5), although with some differences. For instance, the Central America rainfall dipole is weaker and has a smaller spatial extension in TRMM than in CFSR, CMAP does not capture small-scale features due to its low resolution and the thermal low is less pronounced in BEST than in CFSR. Over the land, the largest precipitation discrepancies among the analysed datasets occur over the Yucatán peninsula, the southern tip of Mexico and the Central American countries, where the topographic configuration (formed by mountain ranges and coastal plains), the important influence from both ocean basins and the narrowness of the land domain make the estimates of precipitation highly variable for the different products. An overestimation from the CFSR anomalies with respect to the other analysed datasets is also noted. CFSR precipitation has been reported to have a positive moist bias (Lorenz and Kunstmann 2012; Sun et al. 2018), mainly due to inconsistencies of the precipitation minus evaporation values over both, ocean and land domains.

Finally, the identification of the above links, and in particular of the factors modulating sub-monthly moisture transport toward Central America, has important implications for the predictability of regional rainfall extreme events, such as flash floods and droughts (Gosling et al. 2011) and of the mid-summer drought experienced in southern Mexico and the Pacific coast of Central America (Herrera et al. 2015). Furthermore, a better understanding of the mechanisms underpinning climate variability in the highly-vulnerable Caribbean region is fundamental to more robustly quantify future anthropogenically-driven changes and thus to

develop more adequate and plausible mitigation and adaptation plans to regional climate change.

Appendix

2.A Supplementary figures

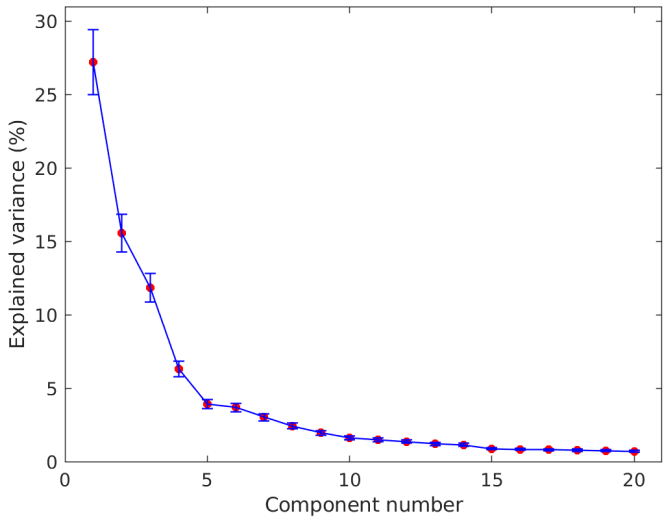

Figure 2.A.1: Scree plot of the twenty principal components of the 925-hPa zonal wind EEOF analysis and their explained variance. The error bars show one standard deviation of the sampling errors (North et al. 1982). The autocorrelation of the timeseries is accounted for in the estimation of the sampling errors (Santer et al. 2000)

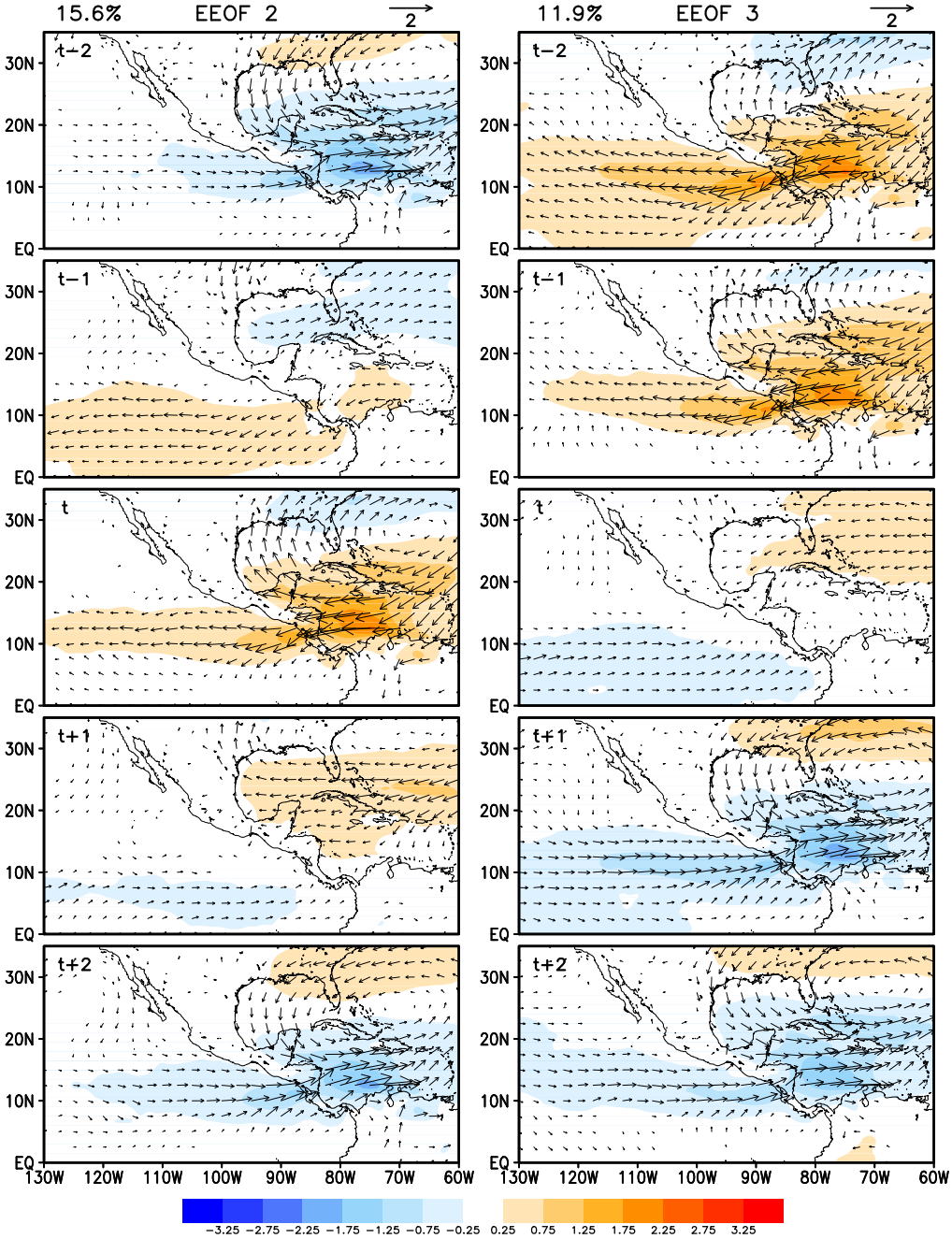

Figure 2.A.2: Regressed 925-hPa total wind [vectors, m s^{-1}] and its zonal component anomalies [shades, m s^{-1}] onto the (left) EEOF2-PC and (right) EEOF3-PC from $t = -2$ to $t = +2$ pentads. The explained variance of each mode is shown in the top left corner of each column

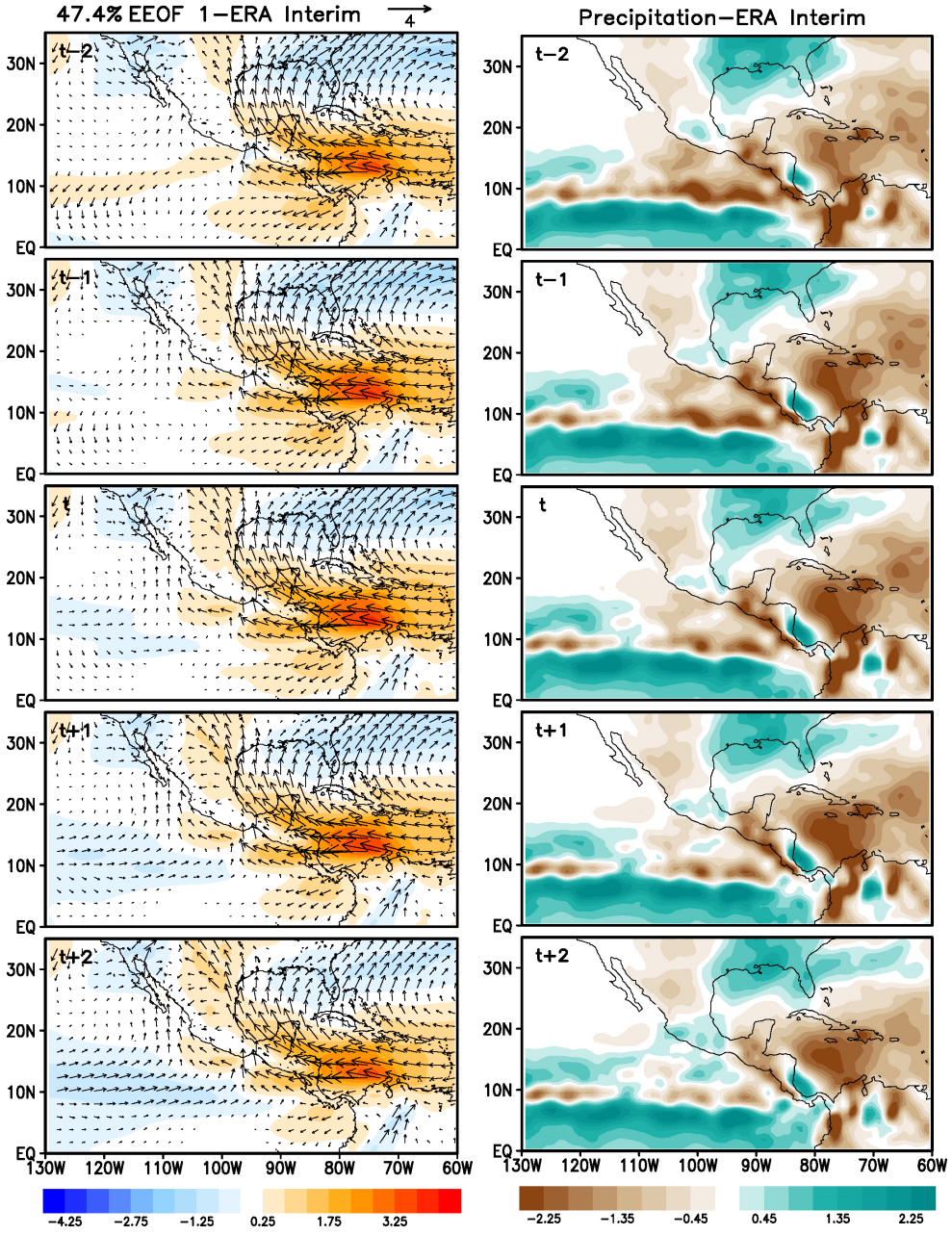

Figure 2.A.3: Regressed ERA-Interim (left) 925-hPa total winds [vectors, m s^{-1}] and its zonal component anomalies [shades, m s^{-1}] and (right) precipitation anomalies [shades, mm day^{-1}] onto the ERA-Interim EEOF1-PC from $t = -2$ to $t = +2$ pentads. Shading in precipitation starts from $\pm$ 0.15 mm day^{-1} and has increments of 0.3 mm day^{-1}

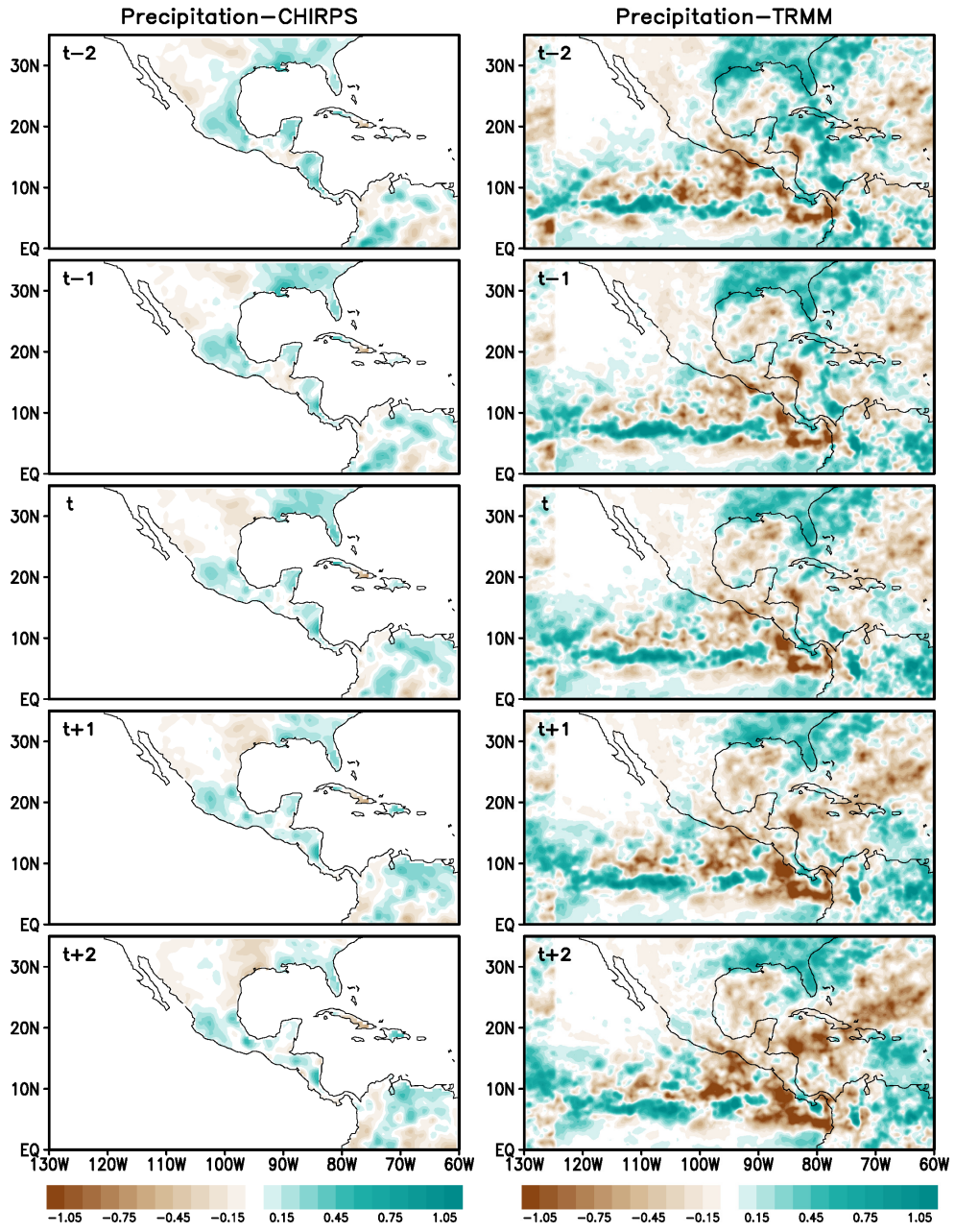

Figure 2.A.4: Regressed (left) 1981-2010 CHIRPS and (right) 1997-2010 TRMM precipitation anomalies [mm day^{-1}] onto the EEOF1-PC from $t = -2$ to $t = +2$ pentads. Shading starts from $\pm$ 0.05 mm day^{-1} and has increments of 0.1 mm day^{-1}

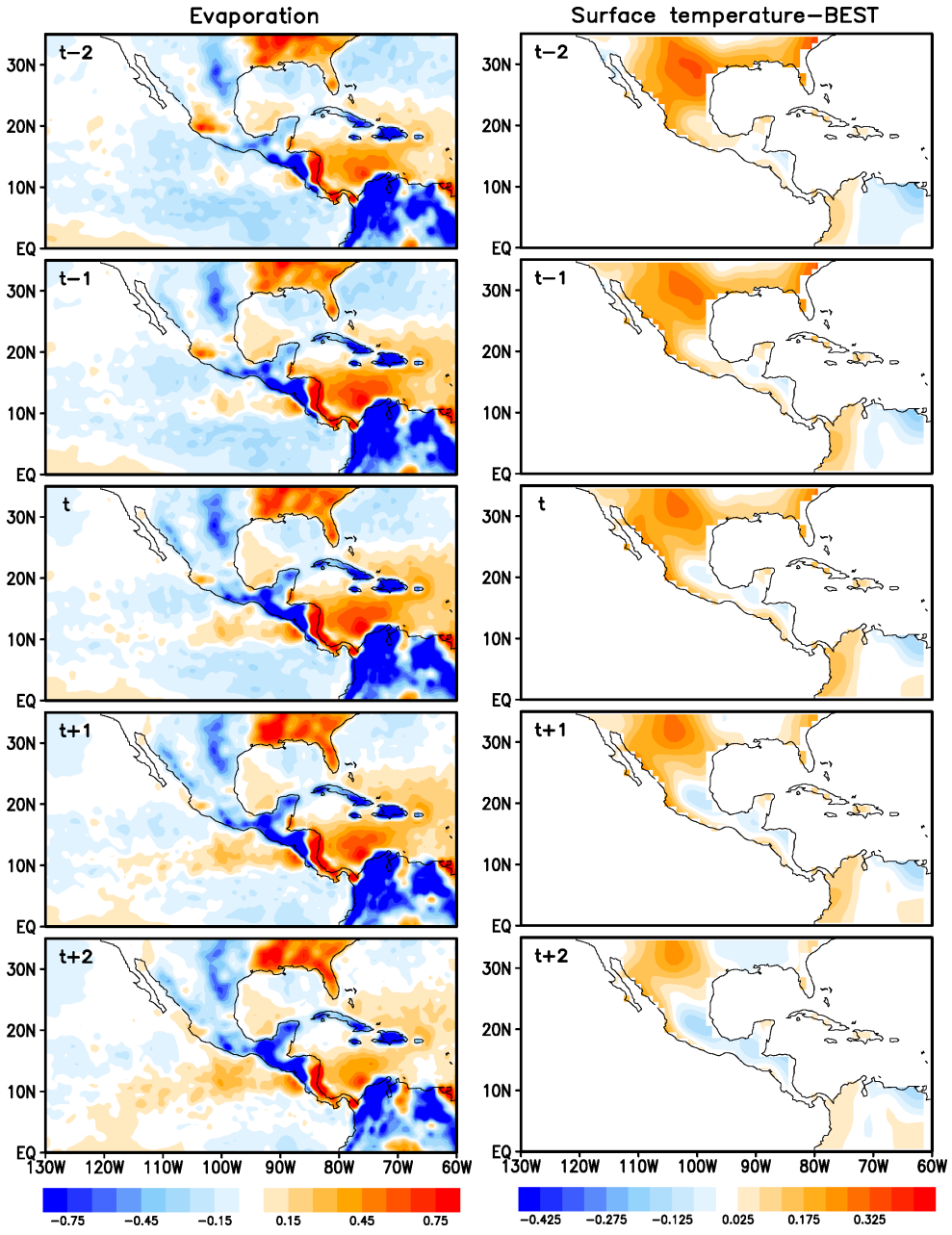

Figure 2.A.5: Regressed (left) 1979-2010 CFSR evaporation [mm day^{-1}] and (right) 1980-2010 BEST air surface temperature [°C] onto the EEOF1-PC from $t = -2$ to $t = +2$ pentads. Shading in evaporation starts from $\pm$ 0.05 mm day^{-1} and has increments of 0.1 mm day^{-1}. Shading in surface temperature starts from $\pm$ 0.025°C and has increments of 0.05°C

Chapter 3

Strong large-scale climate response to North American sulphate aerosols in CESM

This chapter is an adapted version of a paper published in Environmental Research Letters (García-Martínez, Bollasina and Undorf, October 2020 [1])

3.1 Introduction

In this chapter, we assess the summertime climate impact of North American anthropogenic sulphate aerosol emissions using a state-of-the-art climate model, the Community Earth System Model, and identify the underpinning mechanisms. In particular, we emphasise the fundamental role of atmospheric circulation adjustments, which show to be a key factor modulating the hydroclimate over Mexico and the US.

We contrast two sets of experiments of eight members each; an all-forcing ensemble, and an identical one but with North American aerosol emissions kept at their pre-industrial levels. The focus is on the period 1950-1975,

[1] https://doi.org/10.1088/1748-9326/abbe45

which encompasses the largest increase and subsequent peak in regional aerosol emissions, and features an anomalous cooling over the eastern US.

The remainder of the chapter is organised into four main sections. In Section 3.2, we describe the experiments and the methods used. The model validation is presented in Section 3.3. In Section 3.4, we portray the effects of North American anthropogenic aerosols on: the surface and low-level circulation (3.4.1), the radiation and cloud properties (3.4.2), and on the large-scale circulation (3.4.3). Finally, we present a summary, discussion and conclusions in Section 3.5.

3.2 Data and methods

This study makes use of 8-member ensembles of transient coupled experiments with the US National Center for Atmospheric Research (NCAR) Community Earth System Model version 1.2.2 (Hurrell et al. 2013). The model setup and the experiments used here were provided by Sabine Undorf and Massimo Bollasina and are thoroughly described in Undorf et al. (2018a). The atmospheric component is the Community Atmosphere Model (CAM) version 5.3 (Neale et al. 2012), which uses a 3-mode aerosol scheme (MAM3, Ghan et al. 2012) and includes a full prognostic representation of aerosol-cloud interactions (Ghan et al. 2012; Meehl et al. 2013).

We analyse an all-forcing ensemble (ALL) driven by time-varying historical emissions from both natural and anthropogenic sources, and a perturbed ensemble identical to ALL but with anthropogenic emissions of sulphate aerosols and sulphur dioxide from North America (continental United States and Canada) fixed at their pre-industrial levels (NoNA). Assuming linearity in the combined responses (which has been shown to be a reasonable approach, e.g.; Polson et al. 2014), the difference ALL minus NoNA indicates, to a first order approximation, the impact of North American aerosols. Note that non-linear interactions between

aerosols and other forcings (such as GHGs and remote aerosols) are removed in the NoNA ensemble, as these only arise when North American aerosols are present. Such an assumption is routinely made in studies investigating the impact of global forcing factors (e.g., Gillett et al. 2016), and more specifically, that of regional aerosol emissions (e.g., Bollasina et al. 2014; Persad and Caldeira 2018; Undorf et al. 2018b; Westervelt et al. 2018; Wilcox et al. 2019).

We also use several observational datasets to evaluate the present-day model performance: surface temperature from the Climatic Research Unit (CRU) of the University of East Anglia (CRU TS 4.01, at 0.5° resolution, CRU et al. 2017), the Berkeley Global surface temperatures (at 1° resolution, Rohde et al. 2013), and the GISS Surface Temperature Analysis (GISTEMP, at 2° resolution, Hansen et al. 2010); precipitation from CRU (CRU TS 3.26, at 0.5° resolution, CRU et al. 2019) and from the Global Precipitation Climatology Centre (GPCC v7, at 1° resolution, Becker et al. 2013); and wind fields from the National Centers for Environmental Prediction (NCEP) - NCAR reanalysis (NCEP-NCAR, at 2.5° resolution, Kalnay et al. 1996).

The analysis focuses on summer (June-August), when a large percentage of annual precipitation falls over most of the region (over 60% for southern Mexico and up to 40% for southeast US). The emphasis is on the period 1950-1975, when the cooling trend over the southern US-northern Mexico was the largest (see discussion in Section 3.4). This period encompasses the most pronounced near-linear increase in North American aerosol emissions since pre-industrial times to their peak in the 1970s (see Section 3.4; Smith et al. 2011; Hoesly et al. 2018).

Temporal changes are identified by least-square linear trends. To detect changes externally forced by anthropogenic aerosols, trends are computed for ensemble mean quantities which allows to largely filter out internal variability. A two-tailed Student's t test is used to assess the significance (at the 95% confidence level) of the difference in the ensemble-mean response between the ALL and NoNA experiments. The extent to which the robustness of the results is affected

by internal variability of the climate system is qualitatively estimated by the agreement on the sign of the trends across individual ensemble members.

3.3 CESM validation

Figure 3.1 shows the present day (1979-2005) summer climatology of near-surface variables for observations and the CESM_ALL ensemble mean. In general, the model reproduces the main summer features of these near-surface variables. Maxima of surface temperatures are found in northern Mexico and the south and eastern US, while minimum temperatures are found over the mountain region in central Mexico and the northwest US. GPCC precipitation is large along the Pacific coast of Mexico, southern Mexico and in Central America. CESM_ALL captures this feature, although with weaker values, particularly over southern Mexico and Central America. The North Atlantic Subtropical High and the Eastern Pacific High pressure systems are well represented by the model. Near-surface winds in CESM_ALL show overestimated easterlies over both, the Caribbean and the Pacific region, with respect to those of the NCEP-NCAR reanalysis.

The Community Earth System Model v1.2.2 has been successfully used for analysing the effect of sulphate aerosols from North America and Europe on the North Atlantic climate (Undorf et al. 2018a). In particular, for North America during the second half of the 20^{th} century, the model captures the major temperature and precipitation trend patterns. The model reproduces the cooling trend over northern Mexico and the eastern US, although the centre of minimum temperatures is found slightly north of the observed centre (Figure 3.2). The sign of the simulated precipitation trend (Figure 3.2) is in agreement with the observations in the US and northern Mexico (although much weaker); in southern Mexico and Central America the model overestimates the magnitude and spatial extent of the reduced precipitation trend. This is likely due to the model resolution

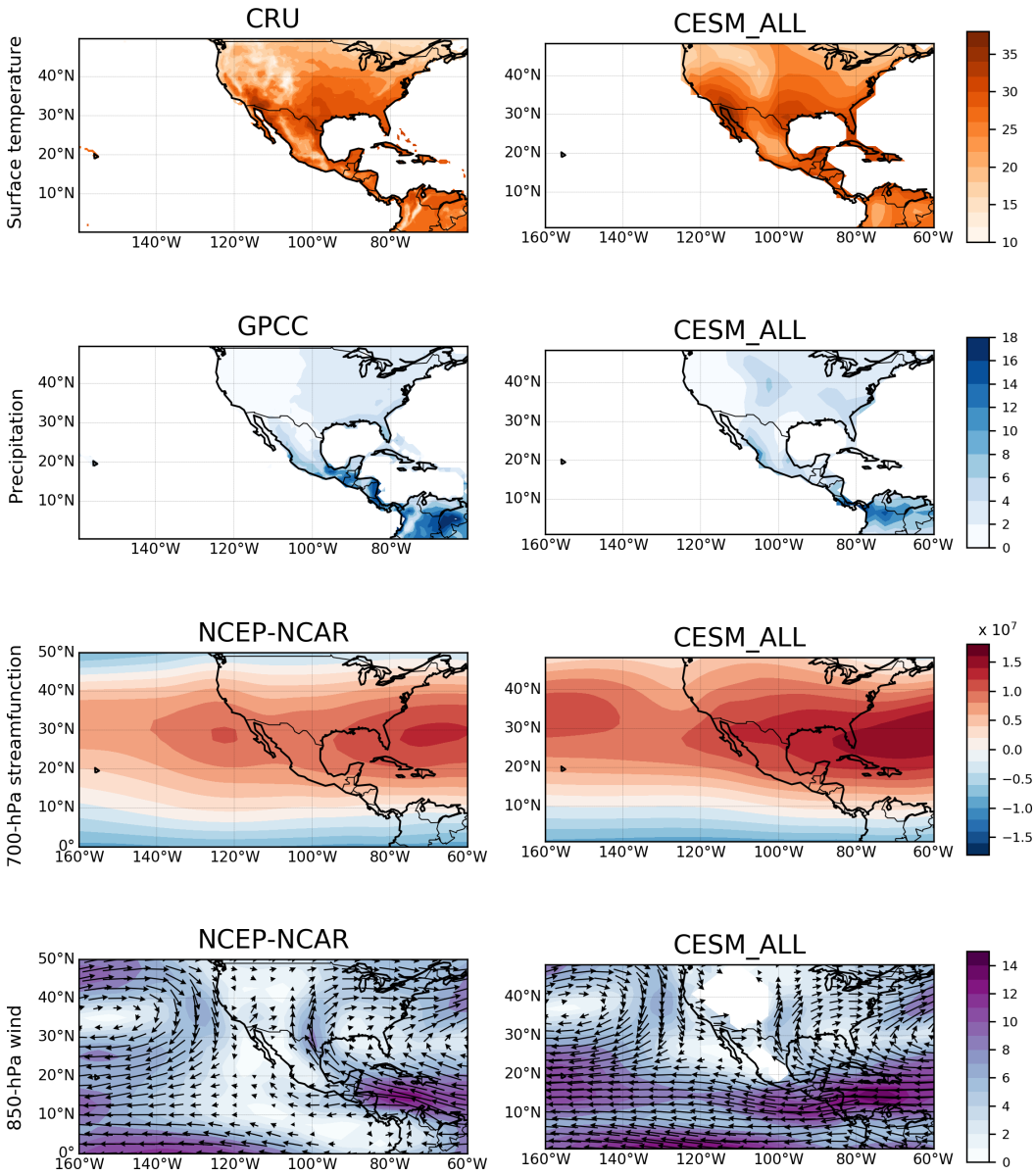

Figure 3.1: 1979-2005 observed and simulated summer (JJA) climatology of surface temperature [°C], precipitation [mm day^{-1}], 700-hPa streamfunction [m^{-2} s^{-1}] and 850-hPa wind [m s^{-1}]

not being enough to solve the small scale processes in this topographically-complex terrain.

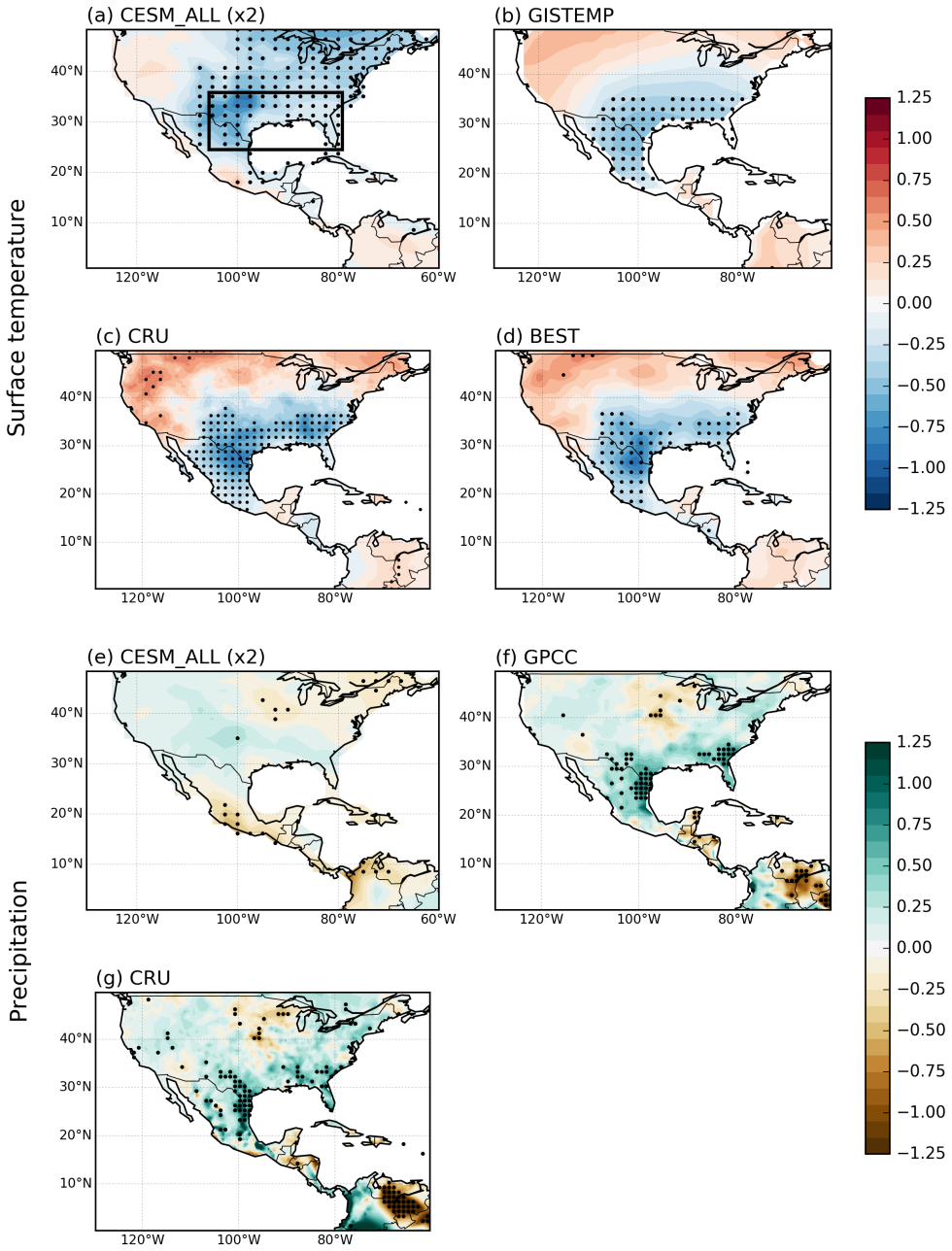

Figure 3.2: (a)-(d) Simulated and observed 1950-1975 summer surface temperature trends [°C decade^{-1}] for: (a) CESM_ALL, (b) GISTEMP, (c) CRU and (d) BEST. (e)-(f) As (a)-(d) but for precipitation trends [(mm day^{-1}) decade^{-1}] using: (e) CESM_ALL, (f) GPCC and (g) CRU. The significance of the trends at the 95% confidence level is stippled. The CESM_ALL trends in (a) and (e) are multiplied by a factor of 2. The stippling in (c), (d) and (g) has been regridded for clarity

3.4 Climate response to North American sulphate aerosols

3.4.1 Surface climate and circulation changes

At global scale, the climate response to increased sulphate aerosols (see Figure 3.3(a)-(b)) features, in accordance with induced changes in the global energy balance, an overall cooling (-0.02°C per decade), particularly strong in the Northern Hemisphere (where aerosol emissions are located; -0.03°C per decade), as well as a global-mean precipitation reduction (-0.003 mm day^{-1} per decade, or about 1% of the model summer climatology) accompanied by a southern shift of the intertropical convergence zone towards the warmer hemisphere (not shown). This is consistent with previous studies (e.g., Ridley et al. 2015; Allen et al. 2015; Westervelt et al. 2018). At regional scale, the climate response patterns display substantial spatial variability and result from the interplay between thermodynamical and dynamical adjustments to aerosol forcing, as well as local feedback mechanisms.

To place the analysis into context, Figure 3.3(c)-(d) compares observed and simulated near-surface temperature trends over the southeastern US (black box in Figure 3.2(a)) as a function of the start and end years during the 20^{th} century. A striking feature is the marked 1950-1975 observed cooling trend (Figure 3.3(c), ∼-0.4°C, statistically significant at the 95% confidence level), and the successive warming to present-day. While the largest temperature anomalies are located over the south-central US, they are part of a coherent large-scale pattern: the cooling is spatially extensive and spread over the eastern US and northern Mexico, accompanied by a weak warming over the western US (Figure 3.2(a)). This spatial structure is consistent among various observational datasets (Figure 3.2(b)-(d)) and is in agreement with previous studies (e.g., Leibensperger et al. 2012; Yu et al. 2014; Mascioli et al. 2017). Albeit of weaker magnitude, the CESM_ALL

ensemble is able to capture the magnitude and spatial pattern of the observed 1950-1975 temperature trend reasonably well, in particular the core cooling over the southern US (Figures 3.3(d) and 3.2(a)-(d)). Notably, the cooling is robust across the 8 ensemble members (Figure 3.4), suggesting it to be primarily due to external forcing. The underestimated magnitude of the cooling in CESM_ALL, however, suggests a potential role of natural variability, or could also be the result of model biases and/or a compensation among different internal coupled processes (e.g., Stevens and Feingold 2009).

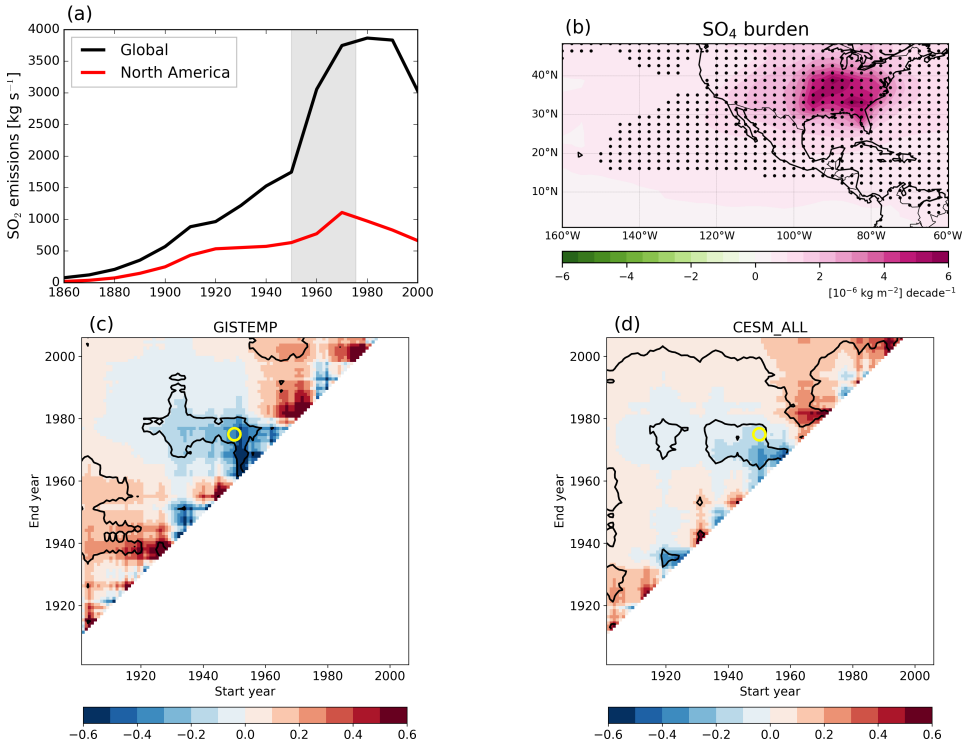

Figure 3.3: (a) Historical global (black) and North American (red) SO_2 emissions [kg s^{-1}] (data from Lamarque et al. 2010). The period 1950-1975 is shaded in grey. (b) Difference of the 1950-1975 linear trends (ALL minus NoNA) of sulphate burden [(10^{-6} kg m^{-2}) $decade^{-1}$]. Black dots indicate significance at the 95% confidence level. (c) Observed and (d) simulated summer surface temperature trends [°C $decade^{-1}$] for southeast US [80-105°W, 25-35°N, box in Figure 3.2(a)] as a function of the start and end years in the 20^{th} century. Trends over all periods of at least 10 years are plotted. The yellow circle shows the 1950-1975 trend. Significance at the 95% confidence level is denoted by black contours

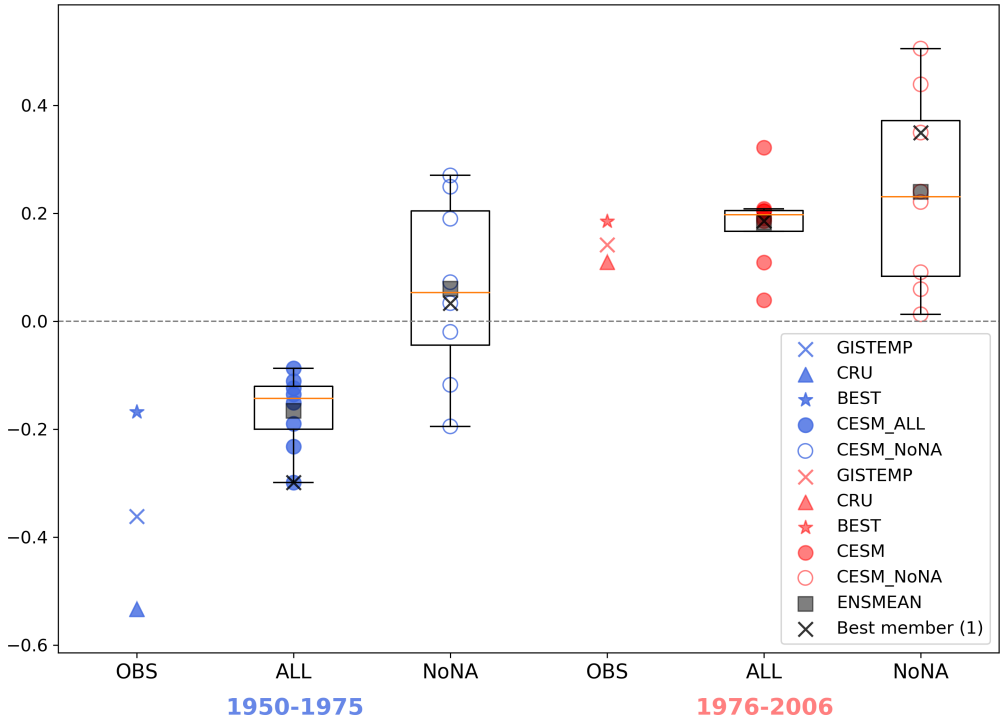

Figure 3.4: Area-averaged mean (orange line), 25^{th}-75^{th} percentile spread (black box) and ensemble minimum and maximum (black whiskers) of surface temperature trends [°C decade^{-1}] in southeastern US [80-105°W, 25-35°N, black box in Figure 3.2] for CESM_ALL and CESM_NoNA (ensemble mean and individual members) during 1950-1975 and 1976-2006. The observed (GISTEMP, CRU and BEST) area-average trends are also shown for reference

Sulphate aerosols are found to be a key driver of the temperature anomalies described above. The large sulphate burden over the eastern US (Figure 3.3(b)) results in a significant regional surface cooling (up to -0.5°C per decade, Figure 3.5(a)), enhancing the all-forcing trend and, although weaker, showing a similar spatial pattern to observations (Figure 3.2(a)-(d)). Note that the largest negative temperature trends are located to the west of the region of maximum SO_4 burden and the cooling extends to the Gulf of Mexico and the North Atlantic Ocean (Figure 3.5(a)). Furthermore, aerosols appear responsible for the weak warming along the western US and southern Mexico.

The land precipitation response to increased sulphate aerosols (Figure 3.5(b)), while modest over the emission region, features a large-scale wettening of up to

0.15 mm day^{-1} per decade over the Great Plains, the southern US and northern Mexico, accompanied by a significant drying (-0.25 mm day^{-1} per decade) over western Mexico. The aerosol imprint is recognisable in the all-forcing pattern, and the latter is broadly consistent with the observed precipitation trends, although with some regional differences and of weaker magnitude (Figure 3.2(e)-(g)). Over the ocean, widespread drying is found over the western North Atlantic and the Gulf of Mexico, while a dipole of zonally-elongated anomalies forms over the north-equatorial eastern Pacific (Figure 3.5(b)), suggestive of an aerosol-driven anomalous southwestward shift of the climatological rainfall.

The surface temperature and precipitation changes discussed above are associated with pronounced regional atmospheric circulation anomalies. Changes in the lower-tropospheric atmospheric circulation modulate heat and moisture transport and its convergence over land, an important component of the regional atmospheric water balance (Mo et al. 2005; Nigam and Ruiz-Barradas 2006; Durán-Quesada et al. 2010; Amador et al. 2016). Additionally, possible variations in the relative contribution of moisture convergence and evaporation may have crucial implications for land water resources and storage under climate change (e.g., Ruiz-Barradas and Nigam 2006).

The 700-hPa streamfunction (Figure 3.5(c)) shows the development of a low-tropospheric high pressure anomaly over the western North Atlantic with a corresponding pressure decrease towards the subtropical and equatorial Pacific, consistent with a thermodynamical response to the anomalous surface cooling from increased sulphate aerosols and subsequent mass redistribution. However, the centre of the anticyclonic anomaly is not geographically collocated with the largest increase in aerosols over the northeastern US but is displaced northeastward over the Atlantic. This is suggestive of an atmospheric adjustment to aerosol changes, resulting in a large-scale dynamical response pattern extending beyond the source region.

As a result, the North Atlantic subtropical high, a key dynamical feature mod-

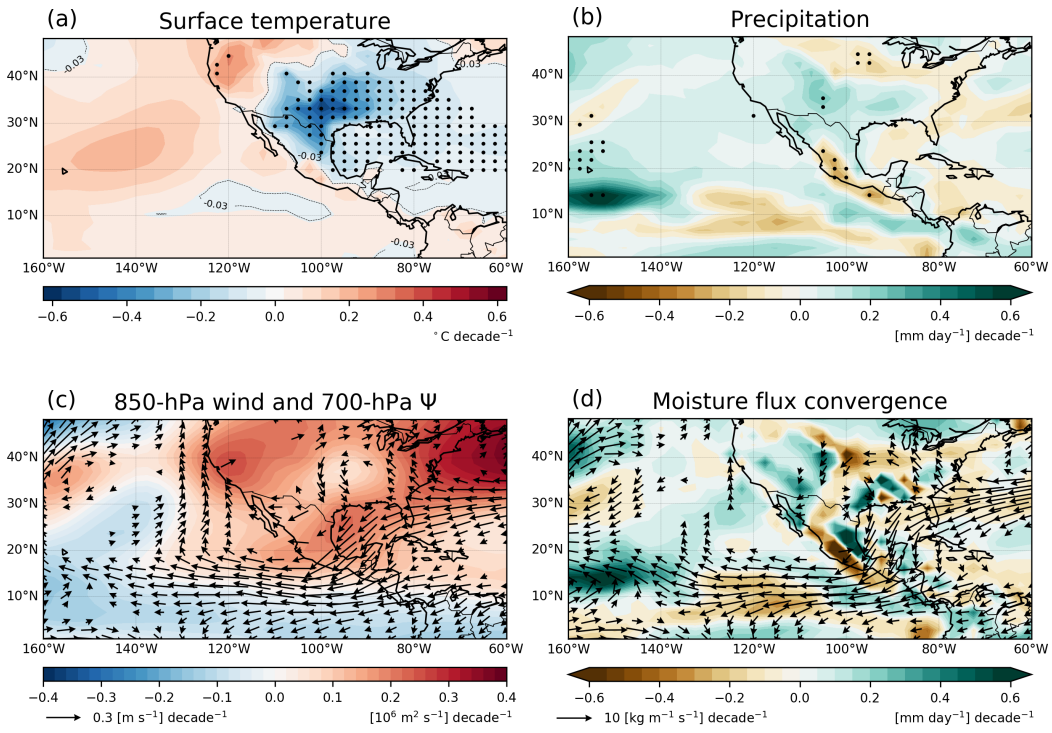

Figure 3.5: Difference of the 1950-1975 linear trends (ALL minus NoNA) of: (a) surface temperature [°C decade^{-1}], (b) precipitation [(mm day^{-1}) decade^{-1}], (c) 850-hPa wind [vectors, (m s^{-1}) decade $^{-1}$] and 700-hPa streamfunction [ψ, shades, (10^6 m^2 s^{-1}) decade^{-1}], and (d) vertically integrated moisture flux [vectors, (kg m^{-1} s^{-1}) decade^{-1}] and its convergence [shades, (mm day^{-1}) decade^{-1}]. Positive streamfunction values indicate anticyclonic circulation. Significance at the 95% confidence level is stippled, (a)-(b) only. The agreement on the sign of the trends for (a) and (b) across individual ensemble members is shown in Figure 3.A.1

ulating moisture transport towards Mexico and the central-eastern US, intensifies, especially on its northern flank, and extends southwestward across central Mexico (Figure 3.5(c)). Anomalous low-tropospheric easterlies blow over the subtropical western Atlantic (Figure 3.5(c)) obstructing the climatological southerlies over the southern US and deflecting the climatological easterlies over the Caribbean southward, which leads to anomalous moisture flux divergence over the eastern seaboard of the US and the northern Gulf of Mexico (Figure 3.5(d)). The interaction between the enhanced easterly moisture transport and the elevated topography of central Mexico favours positive rainfall trends on the Atlantic side,

while suppressing rainfall on the Pacific side. A stronger northeastward pressure gradient over the eastern tropical Pacific reinforces the climatological easterlies but also induces anomalous divergence, leading to anomalous drying there and the precipitation shift mentioned above.

The 850-hPa flow associated with the anomalous Atlantic high displays a secondary branch with cyclonic rotation over the eastern US that later joins the flow over the Gulf of Mexico (Figure 3.5(c)). Correspondingly, the anomalous northerly stationary moisture fluxes across the continental US oppose their climatology (e.g., Ruiz-Barradas and Nigam 2006), and feature divergence over the Great Plains (Figure 3.5(d)). The contribution of this drier northerly flow to the positive precipitation anomaly of the region turns out to be negligible, which suggests a key role of dynamically-induced convergence, rather than transport. Further evidence for this is provided by changes in the 700-hPa circulation (Figure 3.5(c)), the lowest available level above regional topography, which hints to a plausible dynamical link with the moisture convergence pattern via Sverdrup balance and induced vertical motion. We will discuss this link below. The leading role of evaporation anomalies (Figure 3.A.2) is striking over the southwest US and northern Mexico, a dynamically active region enclosing the northern edge of the North American monsoon, where water recycling is particularly large (evaporation largely exceeds precipitation), and compensates for the regional anomalous vertically-integrated moisture divergence.

3.4.2 Aerosol-radiation-cloud interactions

An examination of the changes in radiation and clouds sheds light on the realisation of the regional aerosol impact. Increased sulphate loading (Figure 3.3(b)) leads to a marked reduction in all-sky and clear-sky downwelling shortwave radiation at the surface (Figure 3.6(a)-(b)), with decreases of up to -7 and 1.25 W m^{-2} per decade, respectively, over the southeastern US. There is also a decrease of -4 W m^{-2} per decade at the top of the atmosphere (TOA, not

shown). Shortwave cloud forcing (i.e. the difference between all-sky and clear-sky shortwave radiation) changes are predominant over the aerosol emission region (up to 80% of the all-sky changes), suggesting aerosol-cloud interactions to play a critical role there. Clear-sky shortwave radiation anomalies at the surface and TOA display considerable similarity, reflecting the scattering properties of sulphate aerosols. Over the central and western US, both surface and TOA all-sky radiation changes display a decrease while the corresponding clear-sky anomalies are negligible, indicative of increased radiation scattering by more abundant clouds and associated precipitation (Figure 3.5(b)). Similarly, the positive all-sky radiation flux anomalies over western Mexico and further west over the subtropical Pacific are related to drier conditions.

Changes in various cloud characteristics (Figure 3.6(c)-(f)) show similar large-scale response patterns consistent with radiation and precipitation anomalies. Low-level cloud cover (Figure 3.6(c)) features a widespread and significant positive trend over central and eastern US. These changes are accompanied by a significant increase in cloud droplet concentration (Figure 3.6(e)) and, although more confined to the east, by a decrease in the droplet effective radius (Figure 3.6(f)), a manifestation of the cloud-albedo effect in the presence of more abundant cloud condensation nuclei and assuming negligible changes in liquid water (Twomey 1977). However, liquid water path shows a pronounced increase over the eastern US (Figure 3.6(d)), possibly resulting from more abundant droplets held in clouds rather than precipitating out (the cloud-lifetime aerosol effect; Albrecht 1989) and from an enhanced moistened flux from the Atlantic Ocean. We note that in a large domain of the eastern US there is an increase in the droplet effective radius (excepting the easternmost region mentioned above). A plausible explanation for this is the circulation-driven increase in liquid water path overcompensating for any microphysical-driven decrease in the droplet size. This highlights the complexity of the interplay between cloud microphysics and dynamics in addition to the important role of aerosol-cloud interactions found here. Decreased liquid

water path and cloud fraction occur over the north-equatorial Pacific, consistent with the diminished rainfall and enhanced net shortwave radiation at the surface. Anomalies of the opposite sign stretch in a nearly zonal fashion, from the western coast of Central America towards the tropical Pacific, contributing, together with enhanced evaporation (Figure 3.A.2) by stronger easterlies, to cooling SSTs. The negative SST anomaly is then further spread westward by wind-driven advection. Over the northern Gulf of Mexico, dimming by widespread aerosols leads to cooler SSTs, which locally act to strengthen the anticyclone, as well as, regionally, to enhance the thermal contrast between the Atlantic and Pacific basins and thus the pressure gradient and associated flow.

3.4.3 Large-scale dynamics

Given the link between continental surface anomalies and those in the regional circulation, as well as with anomalies over the adjoining oceanic basins (which are known to modulate North American hydroclimate; Kushnir et al. 2010; Burgman and Jang 2015), it is important to examine the large-scale dynamical context, aiding to an improved mechanistic understanding of how these interactions occur. The pattern of anomalous 500-hPa vertical velocity (not shown) bears a strong resemblance to that of rainfall: wetter (drier) areas generally correspond to ascent (descent), as expected from the approximate balance between diabatic heating and mid-tropospheric vertical motion in the tropics and subtropics. This is clearly discernible over the Pacific and Atlantic oceans, far from land and orographic effects (e.g., across Mexico and the southwestern US). The precipitation excess over the central US and northeastern Mexico is also accompanied by widespread ascent, while an area of strong subsidence is located over the drier northern central US.

The 200-hPa geopotential height and meridional wind anomalies (Figure 3.7(a)) further reveal a coherent wave pattern across the Pacific-North American region towards the extratropical Atlantic, indicating that the surface anomalies

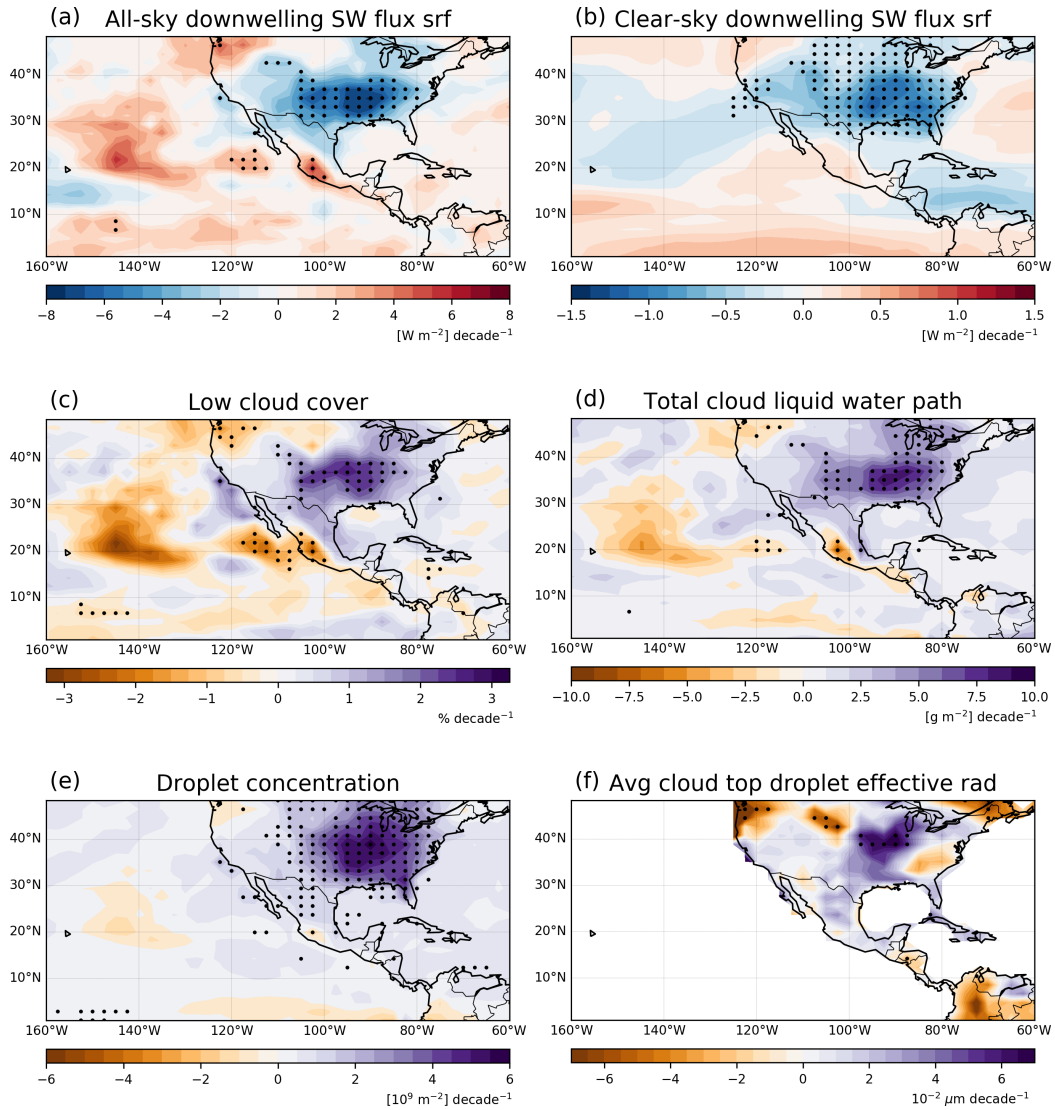

Figure 3.6: As Figure 3.5 but for: (a) all-sky downwelling shortwave radiation at the surface [(W m^{-2}) $decade^{-1}$], (b) clear-sky downwelling shortwave radiation at the surface [(W m^{-2}) $decade^{-1}$], (c) low cloud cover [% $decade^{-1}$], (d) total cloud liquid water path [(g m^{-2}) $decade^{-1}$], (e) vertically integrated droplet concentration [10^9 m^{-2} $decade^{-1}$], and (f) average cloud top droplet effective radius [10^{-2} μm $decade^{-1}$]. In (a) and (b), negative values are upward fluxes and indicate cooling. Significance at the 95% confidence level is stippled

over the eastern US and Mexico are embedded in a hemispheric-wide upper-tropospheric teleconnection pattern. The equivalent-barotropic nature of the anomalies over North America (with a slight westward tilt with height) is

suggestive of a remotely-forced stationary wave response (e.g., Qin and Robinson 1993). Interestingly, the anomalous height pattern resembles the stationary wave forced by diabatic heating in the central Pacific (Ting 1994); also the tri-polar pattern across North America bears striking resemblance to the summertime wave pattern associated with variability of the Great Plains low level jet (Weaver and Nigam 2011) and is further reminiscent of the summer hemispheric-wide wave train identified by Ding and Wang (2005). Insights into the nature of this remote forcing are provided by Figures 3.5(b) and 3.7; the precipitation anomaly (dipole) over the central Pacific results in vertically-integrated diabatic heating anomalies (up to +0.16 K day^{-1} per decade in the positive core, assuming all the heating is due to condensation) and an upper-tropospheric outflow.

Yet, teleconnection patterns are not necessarily generated over the region of the forcing but can be displaced far downstream as determined by the Rossby wave source (RWS; Sardeshmukh and Hoskins 1988). A wave source dipole coincident with convection anomalies in the central north-equatorial Pacific is clearly recognisable (3.7(b)-(c)); strong meridional divergent outflow associated with the rainfall anomalies coexist with large meridional vorticity gradients due to the Asian-Pacific jet (e.g., Sardeshmukh and Hoskins 1988; Qin and Robinson 1993; Weaver and Nigam 2008). The RWS distribution features other centres in the extratropics, which can be interpreted as secondary sources generated by the quasi-geostrophic adjustment of the circulation to the wave generated in the primary source region.

The anomalous hemispheric-wide wave pattern identified above, initially instigated by circulation anomalies over the eastern US and of remote central Pacific origin, in turn has an important imprint downstream in modulating the continental aerosol-related signal. In agreement with the Sverdrup vorticity balance (e.g., Rodwell and Hoskins 2001), strong descent and convection suppression occurs to the east of the upper-tropospheric anomalous ridge and southward flow over the northern Great Plains. Conversely, off the coast of the northeastern US, ascent is

associated with northward flow on the eastern flank of an anomalous trough. Correspondingly, a dry (wet) anomaly is seen in the precipitation distribution (Figure 3.5(b)). A full mechanistic explanation of the dynamics underlying the formation of the continental precipitation pattern shown in Figure 3.5(b) requires, however, to account also for the interaction between upper-tropospheric wave dynamics and the Rockies: anomalous northeasterlies, part of the anomalous upstream anticyclonic circulation, impinge on the eastern slope of the Rockies (around 30-40°N, 105°W), generating low-tropospheric convergence and ascent, and thus positive precipitation anomalies. It is also noteworthy that the wave pattern across the eastern US, notably the location of the anticyclone over the northern Atlantic, is largely coherent with the near-surface circulation anomalies. Particularly, the low-tropospheric anticyclone over the eastern US is displaced northeastward over the ocean, despite the strong land negative radiative forcing. The surface extension of the upper-level anomalies is thus indicative of an interesting modulation of the aerosol sub-regional imprint by the subsequent large-scale circulation response instigated by induced tropical anomalies.

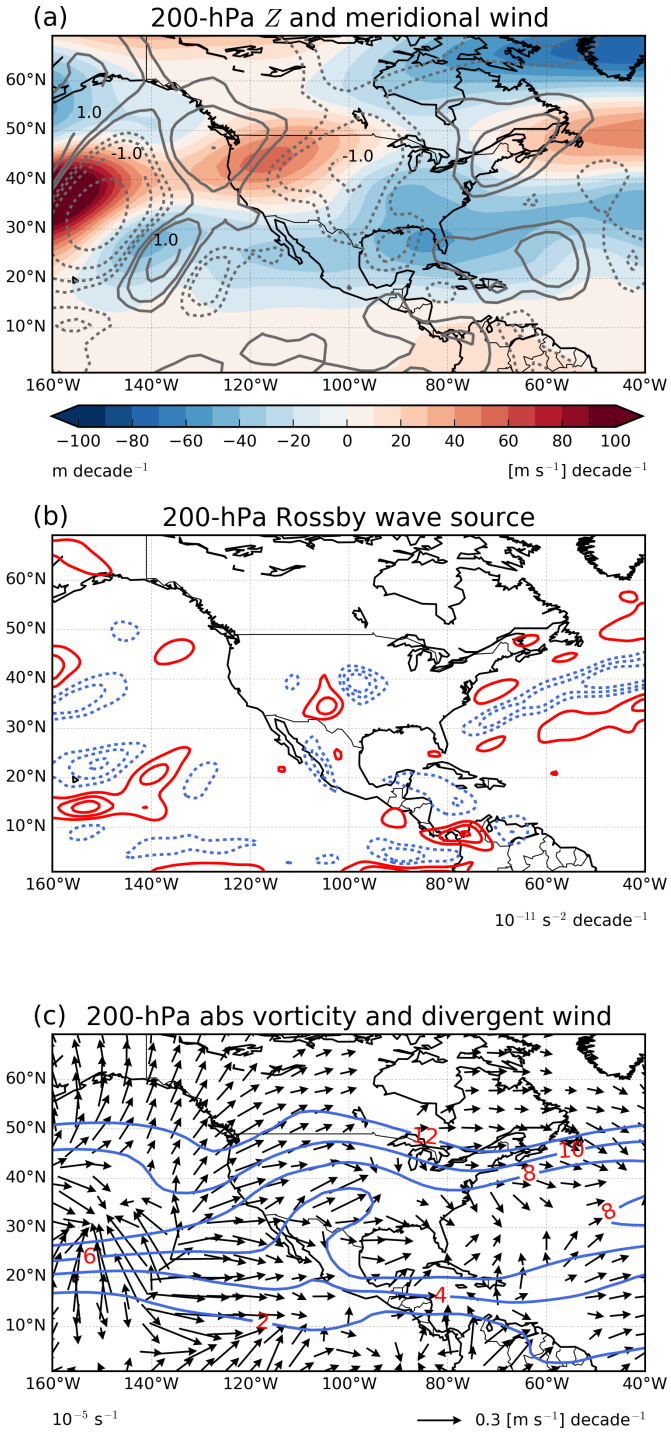

Figure 3.7: As Figure 3.5 but for the 200-hPa circulation: (a) geopotential height [Z, shades, m decade^{-1}] and meridional wind [grey contours, (m s^{-1}) decade^{-1}], (b) Rossby wave source [10^{-11} s^{-2} decade^{-1}], and (c) absolute vorticity [blue contours, 10^{-5} s^{-1}] and divergent wind [vectors, (m s^{-1}) decade^{-1}]. Negative contours are dashed in (a) and (b). The contours shown in (a) are ±0.25, ±0.5, ±1, ±2, and ±3. The contours shown in (b) are ±0.4, ±0.8, and ±1.2. Note that the absolute vorticity is shown as climatological values

3.5 Summary, discussion and conclusions

This work sought to characterise the summertime climate response to increased North American sulphate aerosols and to understand the underlying mechanisms, particularly the role of atmospheric circulation adjustments –a key factor modulating the conspicuous moisture transport and related hydroclimate over Mexico and the US. The focus is on the period 1950-1975, which encompasses the largest increase and subsequent peak in aerosol emissions, and features an anomalous cooling over the eastern US amidst the general continental warming –the "warming hole"–, whose drivers are still the subject of a controversial debate. We used two sets of historical experiments conducted with the CESM model to isolate the impact of regional aerosol changes: a set of all-forcing experiments and an identical one but with North American aerosol emissions kept at their pre-industrial levels.

Regionally, increased aerosols result in widespread large cooling over the central and eastern US and northern Mexico and weak warming over the western US and southern Mexico. Precipitation reduces along the eastern coast of the US, opposed to the wetter US continental interior. This is accompanied by a strengthening and westward expansion of the NASH and subsequent intensification of the low-level easterlies and associated moisture transport across the Gulf of Mexico and the eastern north-equatorial Pacific. Both aerosol-radiation and aerosol-cloud interactions contribute to generating these anomalies. At larger scale, a zonal precipitation dipole appears over the eastern tropical Pacific, in contrast with the more meridional and weaker response in the Atlantic sector. The induced anomalous diabatic heating generates a coherent upper-tropospheric signal in the mid-latitudes from the Pacific to the Atlantic basin, which in turn modulates the local aerosol imprint over North America. This emphasises the prominent role of adjustments in the atmospheric circulation and the interplay between local and remote influences in realising the impact of North American aerosols.

One may wonder whether European aerosols, which also increased during the 1950-1975 period by a similar amount, had any influence. Analysis of an additional 8-member all-forcing ensemble with fixed European sulphate aerosol emissions at pre-industrial levels shows that the temperature and precipitation response patterns over Mexico and the US are of smaller magnitude than those driven by North American aerosols (not shown). Aerosols are transported over the subtropical Atlantic basin by the climatological circulation. However, cooling of the underlying SST is minor (-0.03°C per decade), with negligible changes in lower-tropospheric winds. Instead, regional aerosol dimming induces a large anomalous anticyclone over northeastern Europe extending throughout the troposphere, which in turn leads to an upper-tropospheric wave-train propagating across Eurasia (similarly to Undorf 2019). This reaches the maximum amplitude over Eastern Asia when interacting with the Asian Jet, and then progressively weakens while crossing the eastern Pacific and the US.

It is further reasonable to ask whether an aerosol signature is discernible also after the late 1970s, when stringent regulations aimed at improving air quality led to a rapid aerosol decline over the US (halved in the following 30 years, Smith et al. 2011). To ascertain this, we analyse the period 1976-2006. Observations show a warming trend over the whole domain, particularly large over the western US, western Mexico, and the northeastern US and southeastern Canada (Figure 3.A.3(b)-(d)), while the temperature increase is relatively modest over the central US. Also, an overall wettening, with the largest increase over the southeastern US and the Great Plains, is observed (Figure 3.A.3(f)-(g)). The ALL experiments reproduce the above features well (Figure 3.A.3(a) and (e)). Analysis of the NoNA experiments indicate that aerosols, although decreasing during this period, produce cooling over the central and western US, and enhanced precipitation over the southern US and part of the Great Plains. Despite opposite aerosol variations, these anomalous response patterns bear strong resemblance to those during the earlier period, hinting to a common driving mechanism.

Support to their dynamically-rooted origin is found in the anomalous rainfall pattern over the Pacific (Figure 3.A.1): decreased aerosols result in a nearly-uniform northward precipitation shift, with a core over the north-equatorial basin west of 135°W, which generates a wave-like upper-tropospheric response downstream (not shown) similarly to that of the 1950-1975 period. This further emphasises the role of Pacific anomalies as a key factor modulating the aerosol-driven continental anomalies as well as the fundamental contribution of large-scale circulation adjustments.

Although our findings are based on ensemble experiments with 8 members each, the potential role of the internal variability in modulating multi-decadal climate variations over North America cannot be conclusively assessed. In this respect, the use of large ensembles, such as the CESM-LENS (Kay et al. 2015), would help to more robustly isolate the external component in the presence of internally-driven fluctuations.

Furthermore, the results presented here are based on one model only and so they rely on the model's representation of aerosol, cloud, and circulation interactions, which could differ from those in other climate models and/or the real world given the large uncertainties associated with anthropogenic aerosols and their climate interactions. For instance, the aerosol effective radiative forcing (ERF) in CESM1 is known to be large (Zelinka et al. 2014), which could give a stronger climate response to aerosols than that in other climate models. This will depend on how much of the total contribution to the ERF is coming from the processes that drive the regional climate response identified. Despite these limitations, the important role of regional aerosols and their large-scale footprint found here can translate into implications for near-future projections of hydroclimate variability over Mexico and the US, which affects not just seasonal mean quantities but also climate extremes (see Section 3.B and Figure 3.B.1). With SO_2 emissions considerably reduced in the US, and the expectation of a continued global decline throughout the 21^{st} century, this study

sheds light upon possible ongoing and future regional climate responses to changes in anthropogenic forcing.

Appendix

3.A Supplementary figures

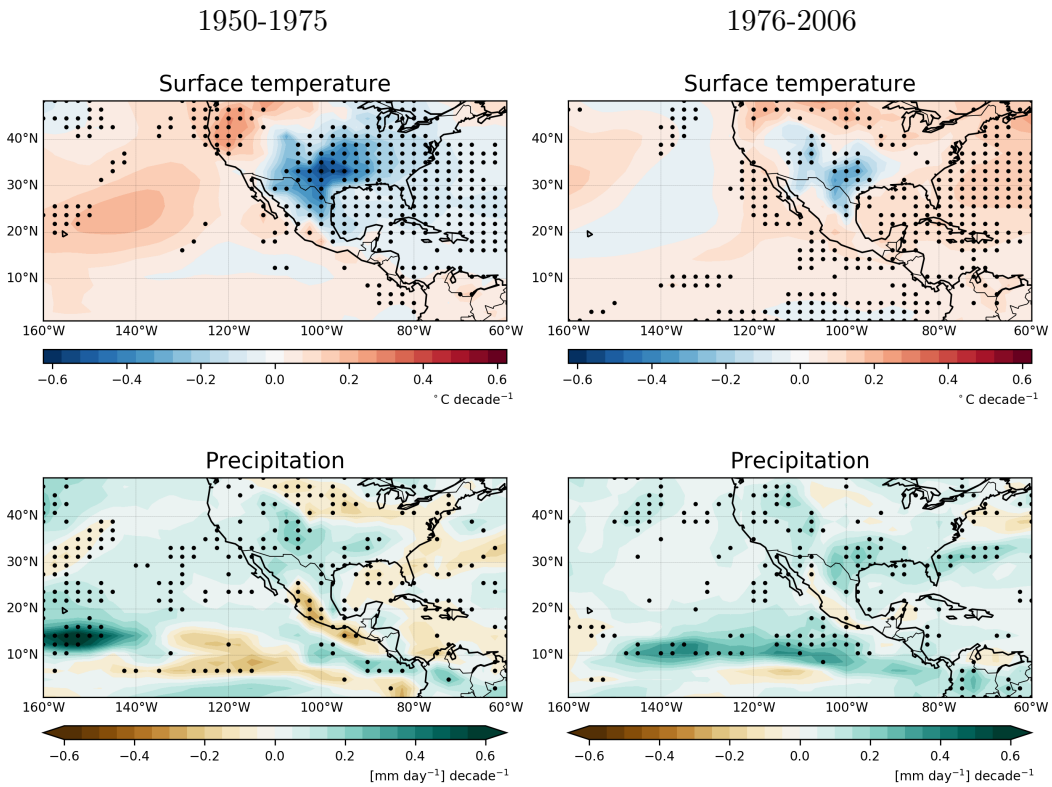

Figure 3.A.1: Linear trends difference (ALL minus NoNA) of surface temperature [°C decade^{-1}] and precipitation [(mm day^{-1}) decade^{-1}] for (left) 1950-1975 and (right) 1976-2006. Grid points where at least six members (out of eight) agree on the sign of the trend are stippled

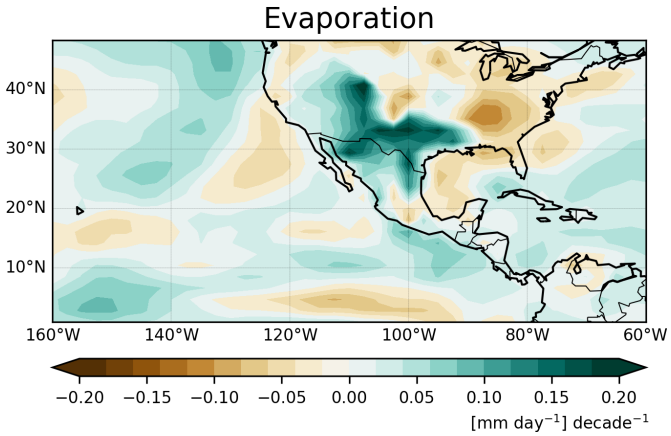

Figure 3.A.2: Difference of the 1950-1975 linear trends (ALL minus NoNA) of evaporation [(mm day^{-1}) decade^{-1}]

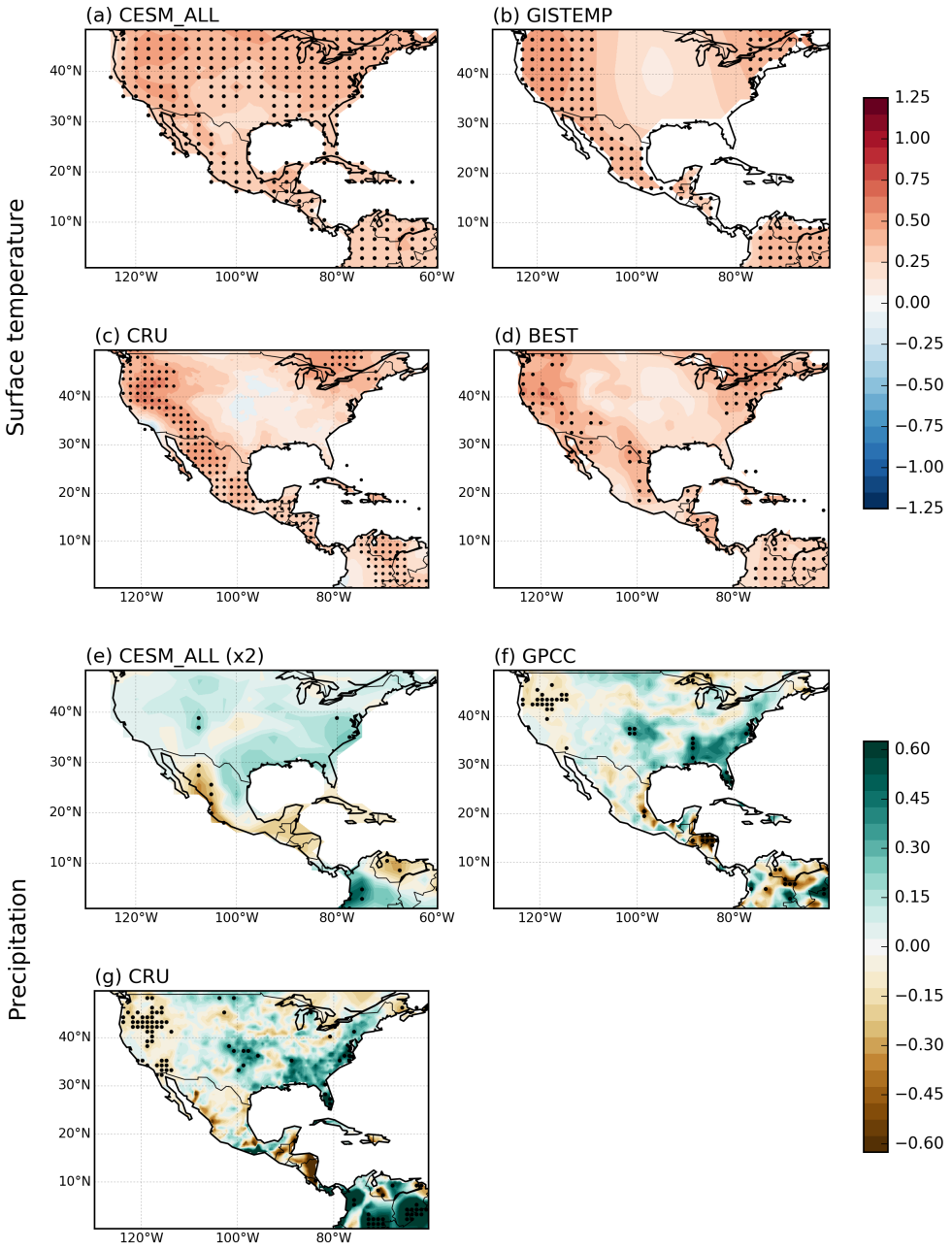

Figure 3.A.3: (a)-(d) Simulated and observed 1976-2006 summer surface temperature trends [°C decade^{-1}] for: (a) CESM_ALL, (b) GISTEMP, (c) CRU and (d) BEST. (e)-(f) As (a)-(d) but for precipitation trends [(mm day^{-1}) decade^{-1}] using: (e) CESM_ALL, (f) GPCC and (g) CRU. The significance of the trends at the 95% confidence level is stippled. The CESM_ALLtrends in (e) are multiplied by a factor of 2. The stippling in (c), (d) and (g) has been regridded for clarity

3.B Response of temperature and precipitation extremes to sulphate aerosols

The response of climate extremes to increased anthropogenic aerosols is explored using two indices from the ones defined by the Expert Team on Climate Change Detection and Indices (ETCCDI, Alexander et al. 2006; Zhang et al. 2011); the monthly maximum value of daily maximum temperature (TXx) and the monthly maximum 1-day precipitation (Rx1day). Interestingly, the aerosol impact is not limited to seasonal-mean anomalies, but is also evident in changes to regional climate extremes. Figure 3.B.1 shows the 1950-1975 linear trends of these two indices for observations (HADEX2, Donat et al. 2013), the all-forcing experiment (ALL) and the difference of the ensemble trends (ALL minus NoNA). The analysed period featured a substantial decrease in TXx and an increase in Rx1day over southeast US (1°C per decade and 4 mm per decade, respectively). Note that the core of these anomalies is collocated with the largest anomalies in the seasonal mean patterns. The model is able to capture the observed trend patterns although with weaker magnitudes. This analysis, albeit not exhaustive, indicates that increased anthropogenic aerosols had an impact not only on the mean climate, but also on the extreme climate conditions (e.g., colder days and more intense rainfall in southeast US), warranting to be further investigated.

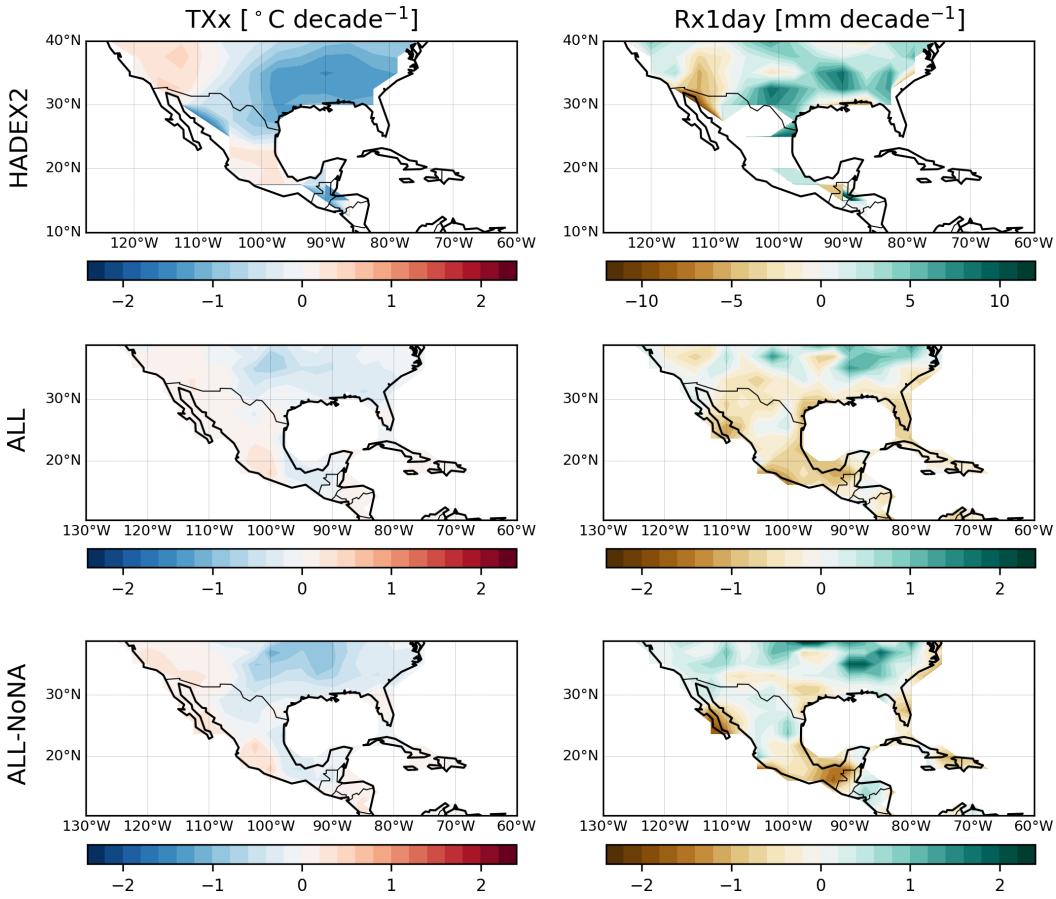

Figure 3.B.1: 1950-1975 linear trends of TXx [°C decade^{-1}] and Rx1day [mm decade^{-1}] extreme indices for: (top panels) HADEX2, (middle panels) CESM ALL and (bottom panels) CESM ALL minus NoNA

Chapter 4

Anthropogenic influence on three types of heat waves over Mexico and the US in the CESM Large Ensemble

4.1 Introduction

In this chapter, we study summer heat waves over Mexico and the United States, a climate extreme that severely impacts human health and ecosystems worldwide. In particular, our objectives are threefold. First, we characterise three independent types of heat waves: compound, daytime and nighttime, during two periods with different anthropogenic forcing, 1950-1975 and 1980-2005. Secondly, we distinguish the relative contribution from anthropogenic aerosols and greenhouse gases in the heat wave changes during each period. Finally, we identify the physical mechanisms associated with the changes in HWs.

We use three sets of experiments from the Community Earth System Model Large Ensemble; an all forcing set (composed by 40 members), and two individual forcing sets (of 20 members each), where global emissions of either aerosols or

GHGs are fixed at 1920 levels. Additionally, observations from the Berkeley Global surface temperatures are used to validate the model. The temporal changes are assessed by computing the linear trends of ensemble-mean quantities.

The chapter is organised as follows. Section 4.2 includes the data and methods description (4.2.1) and the HWs definition (4.2.2). The CESM-LENS performance is evaluated in Section 4.3. In Section 4.4.1, the probability density functions of maximum and minimum temperature are shown. The HWs climatology is then presented in Section 4.4.2, followed by their trends in Section 4.4.3. The HWs response to anthropogenic forcing and the associated dynamical mechanisms are described in Sections 4.4.4 and 4.4.5, respectively. Finally, a summary, discussion and conclusions follow in Section 4.5.

4.2 Data and methods

4.2.1 Observations and the CESM-LENS

Daily maximum and daily minimum temperature (TX and TN, respectively) are obtained from the Berkeley Global surface temperatures dataset (at 1° resolution, Rohde et al. 2013) and from the Community Earth System Model version 1 Large Ensemble (CESM-LENS, at 1° resolution, Kay et al. 2015). The atmospheric component of CESM-LENS is the Community Atmosphere Model version 5.2. We analyse 40 members of the all-forcing simulations (ALLF), where each ensemble member is initialised from different atmospheric conditions (generated by random air temperature perturbations of the order of 10^{-14} K) and run with the same historical radiative forcings. In addition, we make use of two "single forcing" large ensembles, of 20 members each, that are identical to the ALLF one, but with either aerosol (XAER) or greenhouse gas emissions (XGHG) fixed at 1920 levels. We analyse the summers (June-August) of two periods with contrasting historical aerosol trends over North America: 1950-1975 (aerosols increasing) and 1980-2005 (aerosols decreasing).

4.2.2 Heat wave definition

A heat wave is defined as a period of excessive hot weather conditions that last for at least three consecutive days and/or nights. In this work, we use a surface temperature threshold relative to the local climate (i.e. a threshold temperature value is computed for each grid point) to identify a heat wave event. This ensures that hot weather events are properly identified based on the local conditions, which are widely varied across the large domain analysed here. The relative threshold of each summer day (from June 1st to August 31st) corresponds to the climatological (1950-2005) daily 90^{th} percentile of TX and TN based on 15-day samples centred on the day in question. This gives a total sample number of 15 x 56 = 840 days to compute the percentiles (Della-Marta et al. 2007).

We distinguish among three independent heat waves types (Chen and Li 2017; Su and Dong 2019a,b);

1. $Compound = TX > 90^{th}$ percentile & $TN > 90^{th}$ percentile — at least three consecutive days with simultaneous hot days and hot nights

2. $Daytime = TX > 90^{th}$ percentile & $TN < 90^{th}$ percentile — at least three consecutive hot days with mild nights

3. $Nighttime = TN > 90^{th}$ percentile & $TX < 90^{th}$ percentile — at least three consecutive hot nights with mild days

As shown in previous studies (e.g., Chen and Li 2017; Su and Dong 2019a,b; Wang et al. 2020), the 90^{th} percentile is an adequate choice to keep enough heat wave occurrences that properly represent extreme events.

To characterise each of these heat wave types, we compute their frequency (HWF), duration (HWD) and intensity (HWI). The frequency is the total number of heat wave events per summer. The duration represents the average number of consecutive days that meet the criteria outlined above. The intensity indicates the amplitude of the heat wave, and it is estimated as the mean accumulated

heat stress during a heat wave event. In particular for each heat wave type, the intensity is computed as (Chen and Li 2017):

$$Compound\_HWI = \sum_{t=1}^{t=duration} (TX - TX\_threshold(t)) + (TN - TN\_threshold(t))$$

$$Daytime\_HWI = \sum_{t=1}^{t=duration} (TX - TX\_threshold(t))$$

$$Nighttime\_HWI = \sum_{t=1}^{t=duration} (TN - TN\_threshold(t))$$

We estimate the temporal changes by using least-square linear trends. As we are interested in identifying externally-forced changes associated with anthropogenic aerosols and GHGs, the trends are computed for ensemble mean quantities which allows to largely filter-out internal variability. Linear trends are computed for the frequency, duration and intensity of each heat wave type for two different periods: 1950-1975 and 1980-2005.

4.3 CESM-LENS performance assessment

We start by evaluating the ability of the model to reproduce the observed linear trends in TX and TN, the base variables to compute the HW metrics. The trends of TX and TN for BEST and the ALLF ensemble during 1950-1975 and 1980-2005 are shown in Figure 4.1. The observed 1950-1975 TX trend displays a cooling pattern in central and southeast US that extends to most of the Mexican territory and a similar spatial pattern, but weaker, for TN. The ALLF ensemble captures the cooling trends in TX and TN, although weaker in magnitude and with negative trends extending to the central-north and central-east US. During 1980-2005, substantial warming is observed throughout the domain for both

TX and TN, with localised areas of negative trends. For TX, a cooling trend patch extends from the southeast US corner to the central US. For TN, negative trends are observed in west and southern Mexico. The ALLF ensemble shows strong warming in all the analysed continental domain but no cooling trends over the above mentioned regions. The standard deviation across the ALLF ensemble members for TX and TN (not shown) shows these two regions to have the largest model uncertainties, so the discrepancies are likely due, in part, to internal variability.

Next we show the range of the TX and TN trends simulated across the 40 members of the ALLF ensemble (Figures 4.A.1-4.A.4) and some of the members that are closest to observations (Figure 4.2), in order to compare them to the observed trends (Figure 4.1). A noticeable feature is that the trends show a variety of spatial patterns, amplitude and polarity, as expected due to the contribution of internal variability, even under the same external radiative forcing. It is therefore possible to find members that show patterns with different sign, amplitude and location to those of the observations. However, by using a relatively large number of simulations, one could expect some of them to be close to observations (e.g., Figure 4.2). The first noticeable feature in Figures 4.A.1 and 4.A.3 is that during 1950-1975, there is a clear dominating cooling TX and TN trend in most of the members over large parts of the domain, while during 1980-2005 a warming trend is evident (Figures 4.A.2 and 4.A.4). Furthermore, there are some members that show a remarkable similar trend with that of the observations, particularly for TX, where trends are stronger. For instance, members 27, 28, 29 and 34 successfully reproduce the TX and TN cooling over the southeast US and the warming in the northeast US in 1950-1975 (Figures 4.A.1 and 4.A.3). For the later period (1980-2005), members 10, and 35 resemble the observed spatial patterns of TX and TN trends (Figures 4.A.2 and 4.A.4), and member 23 is one of the very few that captures a hint of cooling over Mexico during the second period (Figure 4.2).

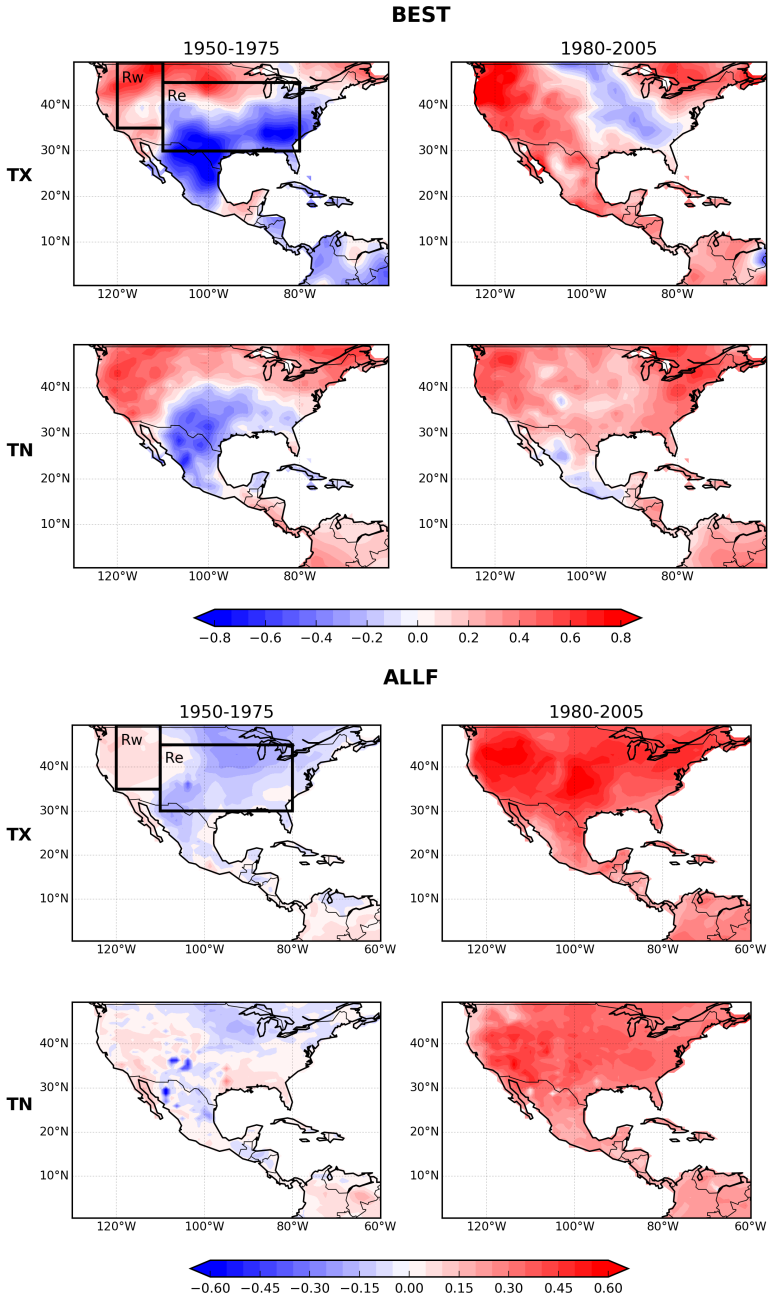

Figure 4.1: Summer TX and TN trends [°C decade^{-1}] during (left) 1950-1975 and (right) 1980-2005 in observations (top four panels) and the ALLF CESM-LENS ensemble (bottom four panels). Two of the focus regions in west (Rw), and mid-to-east US (Re) are showed in boxes

In Figure 4.3 we present the distribution of the area-averaged TX and TN summer trends (1950-1975 and 1980-2005) for two regions in east (Re) and

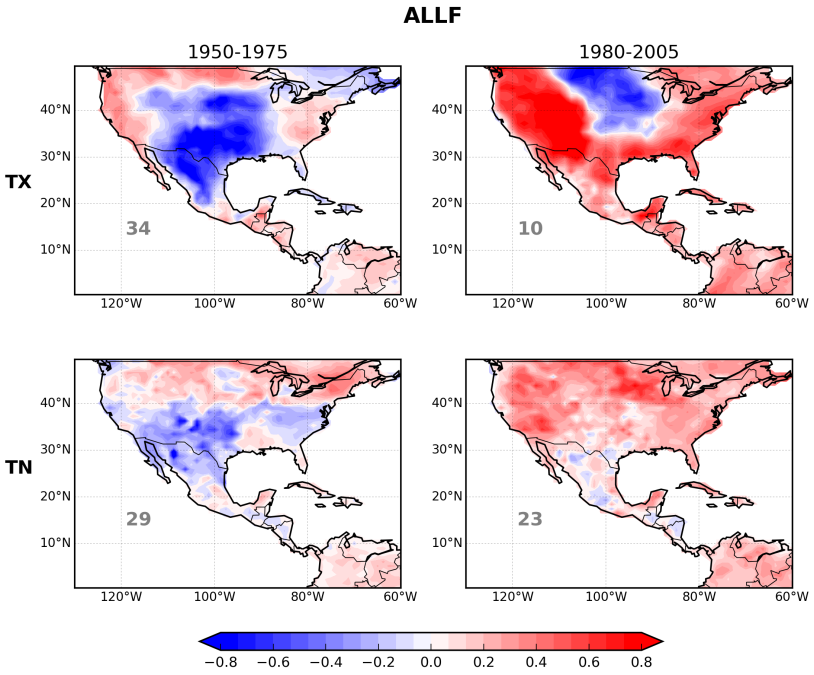

Figure 4.2: Summer TX and TN ALLF trends [°C decade^{-1}] for selected members during (left) 1950-1975 and (right) 1980-2005. The number of the member shown is located at the bottom left of each plot

west (Rw) US across the 40 ALLF ensemble members and the mean-value for observations. For all the cases but one (TN-Rw in 1950-1975), the observed trend lies within the respective ensemble distribution. The histograms for TX and TN show a similar behaviour; most of the ALLF ensemble members are close to the observed trends in Re during 1950-1975 and in Rw for the period 1980-2005. The largest discrepancy occurs in the 1980-2005 TX trend over Re, where the observed mean-value is close to zero (with sub-regions of strong cooling and strong warming cancelling each other out), whereas the ensemble-mean trend is 0.4°C per decade. From the respective histogram and Figure 4.A.2, we can see that only about 8 members are within ±0.2 °C per decade of the observed trend there. The rest of the members show a warming instead. The second largest discrepancy between the model and observations is found in the 1950-1975 TN trend over Rw, where none of the members get the amplitude of the area-averaged observed warming.

These discrepancies are likely due to natural variability, which dominates over external forcing in the respective region and period used.

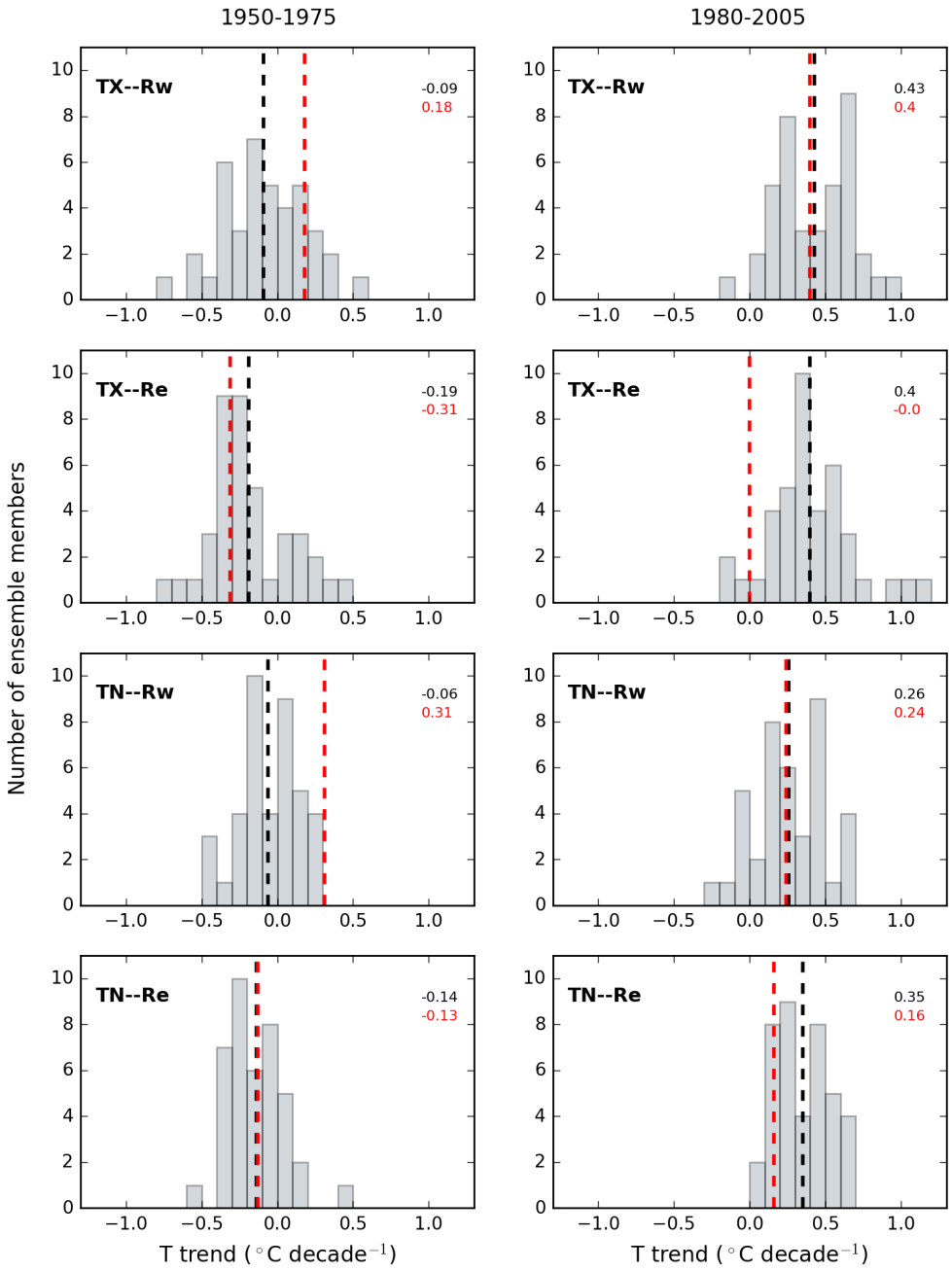

Figure 4.3: Distribution of area-averaged summer TX and TN trends [°C decade^{-1}] in west and east US (see boxes in Figure 4.1) across the 40 members of the ALLF ensemble for the periods (left) 1950-1975 and (right) 1980-2005. The black vertical dashed line indicates the ensemble-mean of the distribution, and the red vertical line the observed mean from BEST (values shown in the top right corner of each panel). The distribution is shown in bins of 0.1°C decade^{-1}

4.4 Changes in compound, daytime and nighttime heat waves: anthropogenic drivers and mechanisms

4.4.1 Probability density functions of TX and TN

To explore the background of heat waves in terms of the maximum and minimum temperature fields and to further assess the model performance, the probability density function (PDF) of observed and simulated daily TX and TN anomalies is computed for two area-averaged regions in west [110-120°W, 35-50°N] and east [80-110°W, 30-45°N] US for different periods (Figure 4.4). To better identify any possible shifts in the temperature anomalies, we present sub-period differences for both study periods, 1950-1975 and 1980-2005, as an analogous to the corresponding linear trends. The PDF distributions show an overall good match of the ALLF ensemble to the observations in both periods for the two selected regions in east and west US. The most notorious discrepancy is a slight TX sub-estimation in the ALLF ensemble compared to BEST in the east US, however, the largest model-observation differences in this and all other PDFs are rather small (of the order of 10^{-1} $^{\circ}C^{-1}$ for a certain anomaly value).

The east and west US regions show some similar behaviours but also dissimilarities in their distribution shapes. The mean of the distributions (values in the top right corner of each plot in Figure 4.4) show negative differences in the first period and positive ones in the second period in both observed and simulated TX and TN over the east and west, showing that the model is able to reproduce the general cooling-to-warming transition from the earlier to the recent period observed over the US. Regarding the distributions, the PDFs for west US are more skewed towards warm anomalies than for the east, particularly in TX. This is coherent with the spatial patterns of trends shown in Figure 4.1. A second difference is that the distribution for the east US has a lower kurtosis than that

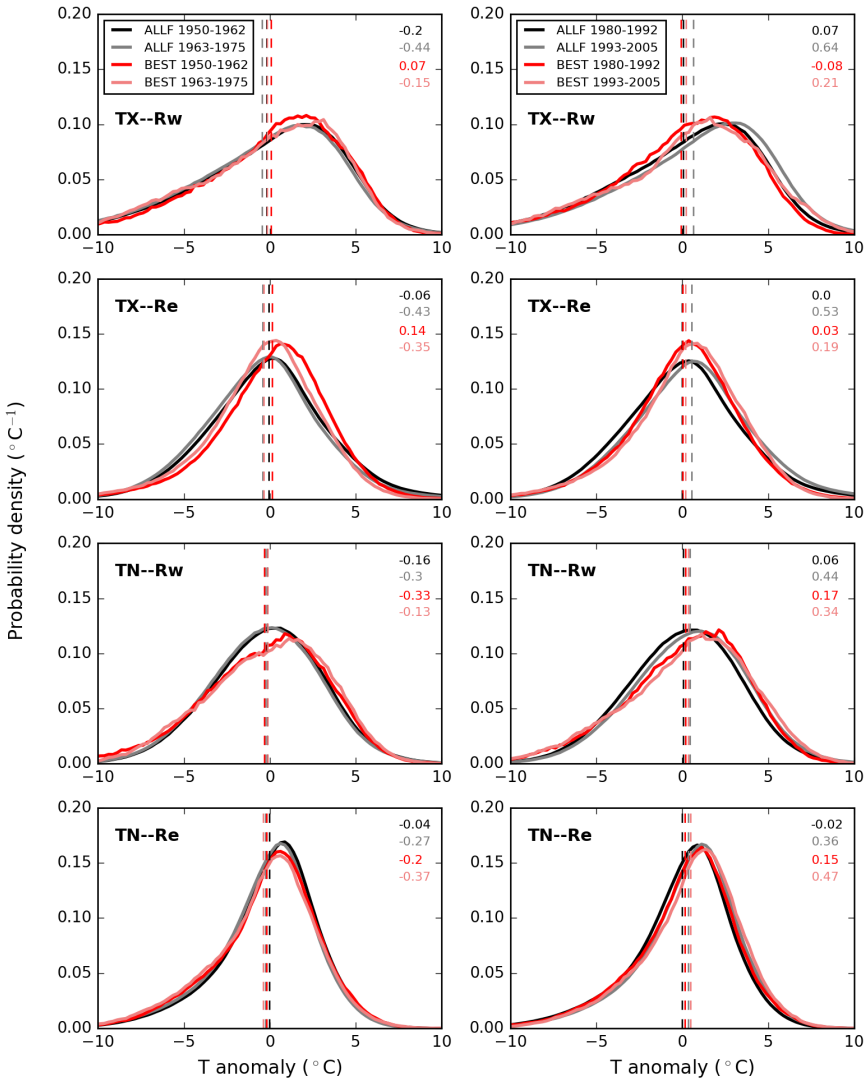

Figure 4.4: Probability density of TX (top four panels) and TN (bottom four panels) [$^{\circ}C^{-1}$] for two regions in west (Rw) and east US (Re). See boxes in Figure 4.1. The PDFs are shown for both halves of each analysed period (1950-1962, 1963-1975, 1980-1992 and 1993-2005): black and grey for ALLF, red and pink for BEST. The PDFs are computed using summer daily data from all gridpoints within the selected regions from all ensemble members to ensure robustness. The vertical dashed lines represent the mean of each distribution (values shown in the top right corner of each panel)

of the west, showing a higher probability of a smaller range of anomalies to occur in the east region.

To better show the small differences in the PDF distributions, we estimate

the PDF change for 1950-1975 and 1980-2005 by doing the difference between the later and earlier halves in each of the periods. These plots are shown in Figure 4.5. A positive PDF change indicates an increase in the probability of a certain temperature anomaly to occur. The opposite is true for a negative PDF change. Note that the ALLF PDFs are constructed with 40 realisations (to ensure robustness) while observations have only one. All gridpoints within the selected domains (Re and Rw) are used. This difference in the number of input data (much larger for ALLF than for BEST) makes the ALLF PDF curves more stable (i.e. less noisy) than those of observations. Interestingly, there is a similar behaviour in the PDF change for both TX and TN over the east and west US. In the first period, there is a higher probability for negative anomalies to occur, while there is a lower chance of positive anomalies. On the contrary, in the second period, the probability for negative anomalies decreases, while the probability for positive anomalies increases. This analysis shows that, along with the substantial spatial trend changes, there were also shifts in the PDF distribution of daily TX and TN between the two periods over the US. Specifically, there is a clear tendency towards cooler temperatures in 1950-1975 and towards warmer temperatures in 1980-2005.

Now we turn the analysis to the contribution of anthropogenic forcing in the PDF distributions. In Figure 4.6 we present the PDF of the XAER and XGHG ensembles (with fixed aerosols and fixed GHGs, respectively), while Figure 4.7 shows the changes in the PDF distributions per period per individual forcing. We find that the XAER and XGHG experiments show probability density curves of similar amplitude to those of the ALLF ensemble (Figure 4.4). In order to better identify the contribution of aerosols and GHGs to the ALLF PDFs, we can look at the differences in the mean distributions of each ensemble. The ALLF minus XAER mean distribution shows that, during 1950-1975, on average, aerosols decreased the probability distributions more than -0.32°C^{-1} (with the largest being -0.47°C^{-1} for TX over west US), while GHGs increased it by 0.13-

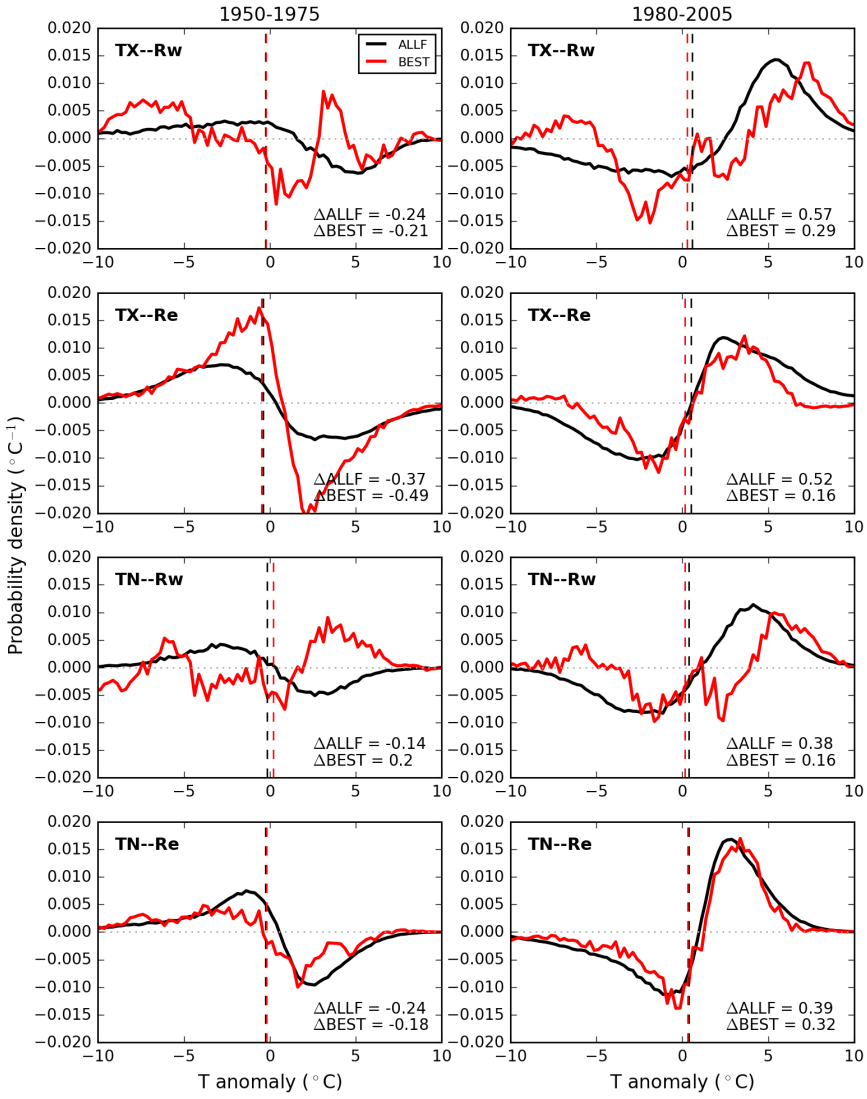

Figure 4.5: Change in the probability density of TX (top four panels) and TN (bottom four panels) [$^{\circ}C^{-1}$] for two regions in west (Rw) and east US (Re). See boxes in Figure 4.1. The curves are obtained by subtracting the PDF of the first half of each analysed period from the PDF of the respective second half (e.g., the 1963-1975 PDF minus the 1950-1962 PDF). The difference is shown in black for ALLF and red for BEST. The vertical dashed lines represent the mean change of each distribution (values shown in the bottom right corner of each panel)

$0.37^{\circ}C^{-1}$. In contrast, during 1980-2005, with aerosol emissions decreasing and GHGs continuously rising, the probability density increased in all cases (TX and TN in both west and east US) by up to $0.47^{\circ}C^{-1}$.

As shown before, the PDF changes found in TX and TN vary in line with

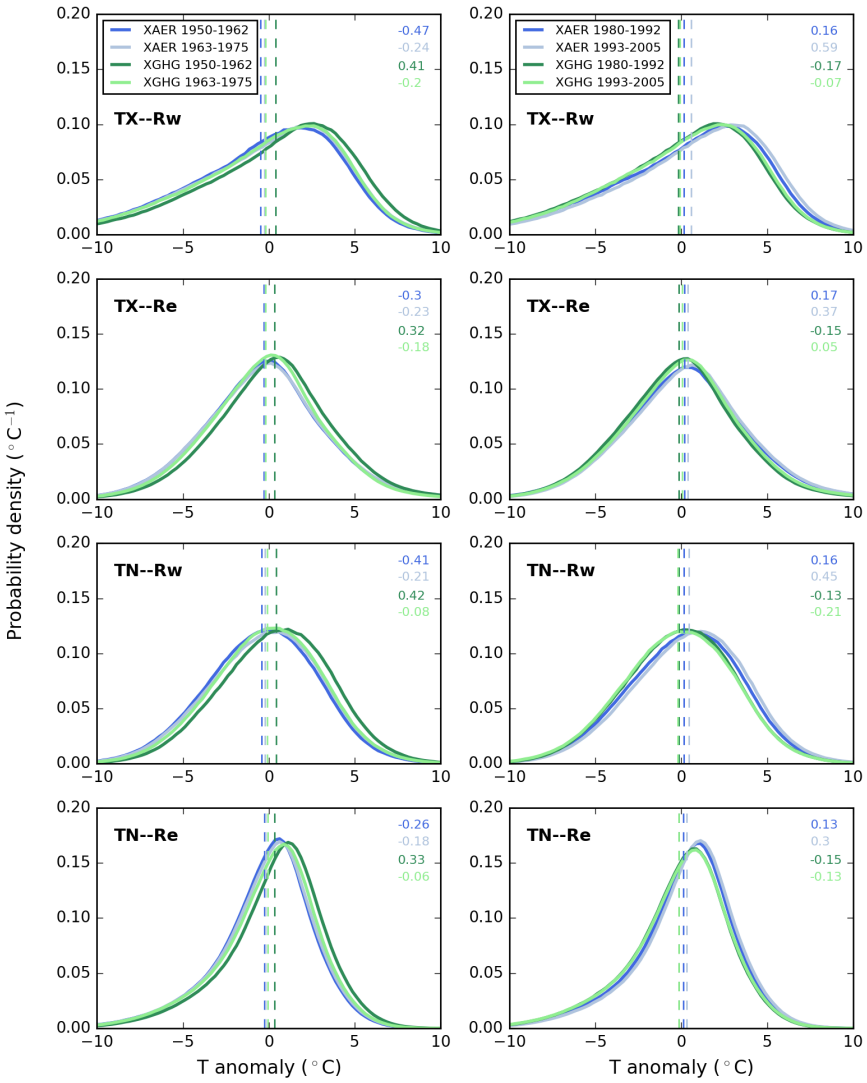

Figure 4.6: As Figure 4.4 but for the ensembles with fixed aerosols (XAER, blues) and fixed GHGs (XGHG, greens)

the evolution of anthropogenic aerosol and GHG emissions. This is further appreciated in the changes of the PDFs. During 1950-1975, the XAER ensemble (Figure 4.7) shows inverse curves to those in the ALLF (Figure 4.5), indicating that, under fixed aerosol emissions, the change in the probability distribution would be of the opposite polarity. The XGHG ensemble, on the other hand, presents similar curves to the ALLF. This shows that the contribution form anthropogenic aerosols is greater than that of GHGs in the earlier period. The

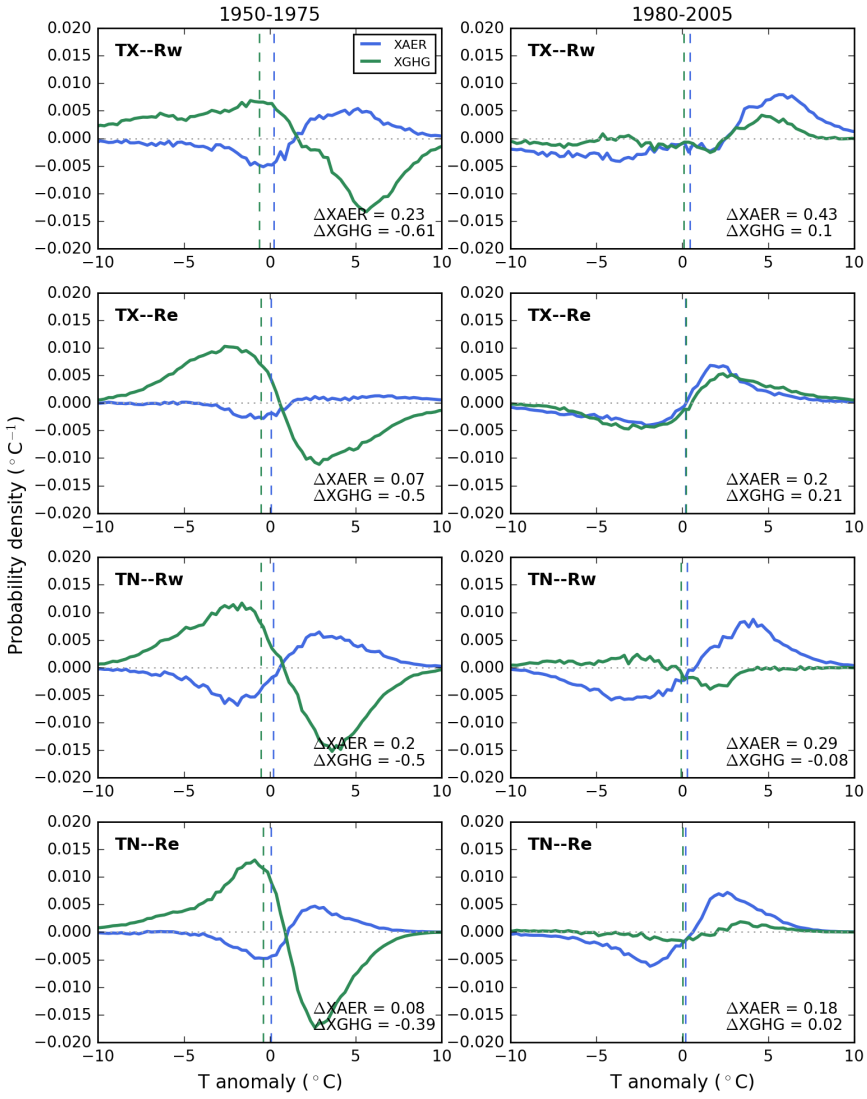

Figure 4.7: As Figure 4.5 but for the ensembles with fixed aerosols (XAER, blues) and fixed GHGs (XGHG, greens)

more recent period shows a different story. Here, both XAER and XGHG have curves similar to the ALLF ones (with the exception of TN over west US in XAER). This similarities evidence that both, reduced aerosols and increased GHGs, contributed to the observed probability density during 1980-2005.

In this section we showed that the CESM Large Ensemble is a reliable tool to carry out this study, both for its skill to simulate the evolution, spatial patterns and probability density functions of TX and TN over the study region, and for the

robustness of its results, achieved by the relatively large size of its ensembles (of 40 and 20 members in the ALLF and single forcing experiments, respectively). In the following sections we will investigate the heat wave changes during the selected periods and the contribution from anthropogenic aerosols and GHGs. We will do so with good confidence in the experiments used.

4.4.2 Climatology of heat waves

First we describe the most prominent observed characteristics of each of the three heat wave types. In Figures 4.8 and 4.9, we present the BEST summer mean values for the three HW indicators analysed here: frequency, duration and intensity. The summer means are computed for the periods 1950-1975 and 1980-2005 to identify potential differences between them. Each HW type clearly shows a preferred location of occurrence. Compound HWs are mainly observed over the eastern half of the US and California, while daytime and nighttime HWs are more frequent over Mexico and southeast US. Most of these regions experience up to 2 HW events per summer (or more in the second period). Their duration also varies by HW type and by region. However, all three HW types show a considerable increase in duration during the second period. The longest HW events take place in California for the compound HWs, in southern Mexico for the daytime HWs and in southeast US for the nighttime type, all with a maximum length of up to 4 days on average. The most intense HW events are observed in the compound type (with mean accumulated heat stress of up to 4°C per event) over most of the US domain, followed by the daytime HWs, where maximum values (1.2 °C per event) are found over the southeast US and Mexico. Nighttime HWs are not as intense as the other two types.

The CESM-Large Ensemble reproduces the spatial pattern and magnitude of these features fairly well (Figures 4.10 and 4.11). There are, however, some regional differences. The largest discrepancies during the first period occur in the nighttime HWs over Mexico, with a lower frequency and shorter duration in the

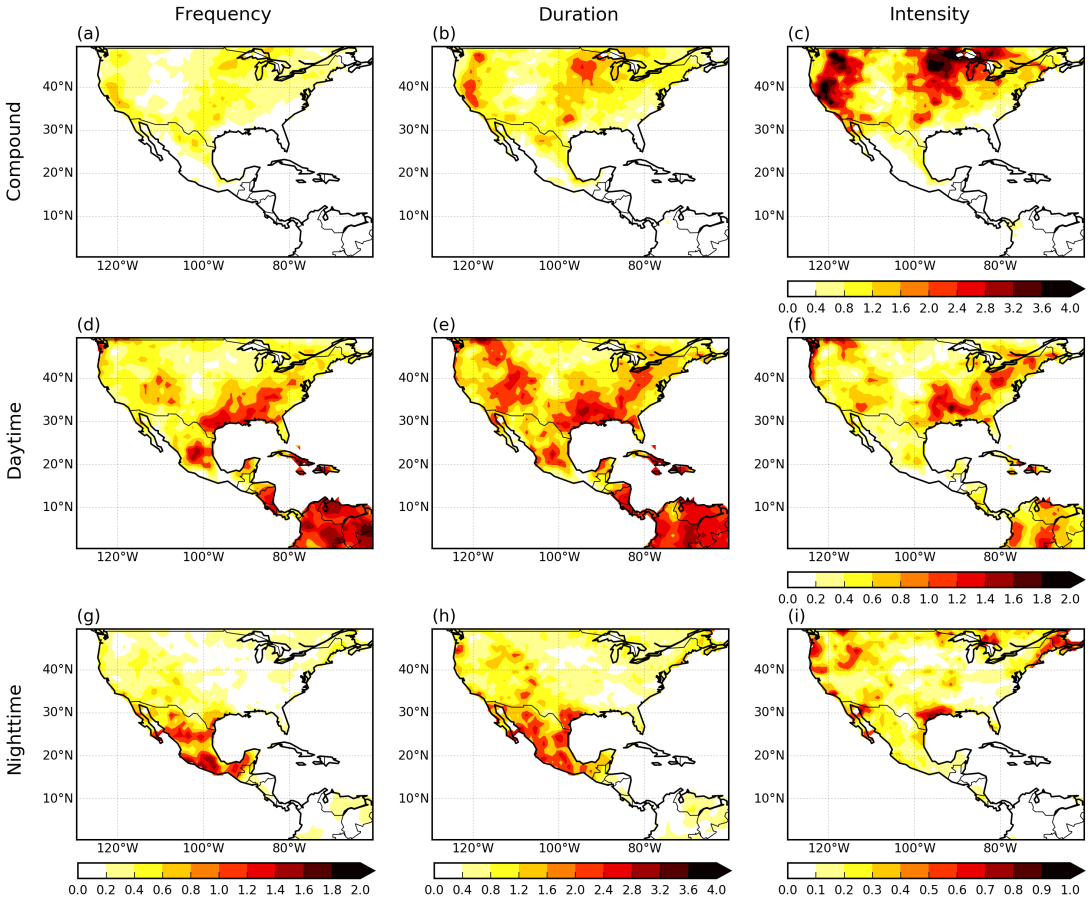

Figure 4.8: BEST 1950-1975 climatology for frequency [HWs summer^{-1}], duration [days event^{-1}] and intensity [°C HW^{-1}] of compound, daytime and nighttime heat waves

CESM-LENS compared to those of BEST. A second noticeable difference during the first period are more intense simulated daytime HWs than observed. During the second period, there is a sub-estimation of the compound HWs in all three indicators over most of the US (except in California) and in the nighttime intensity over southeast US. On the other hand, an overestimation occurs in daytime HWs over Mexico and the southeast US. Overall, a general increase in all three metrics indicates more frequent, longer and more intense HW events in the recent period, particularly for the identified key regions in both, observations and the model. To better quantify these temporal changes, we present linear trends of the frequency, duration and intensity of each HW type in the following section.

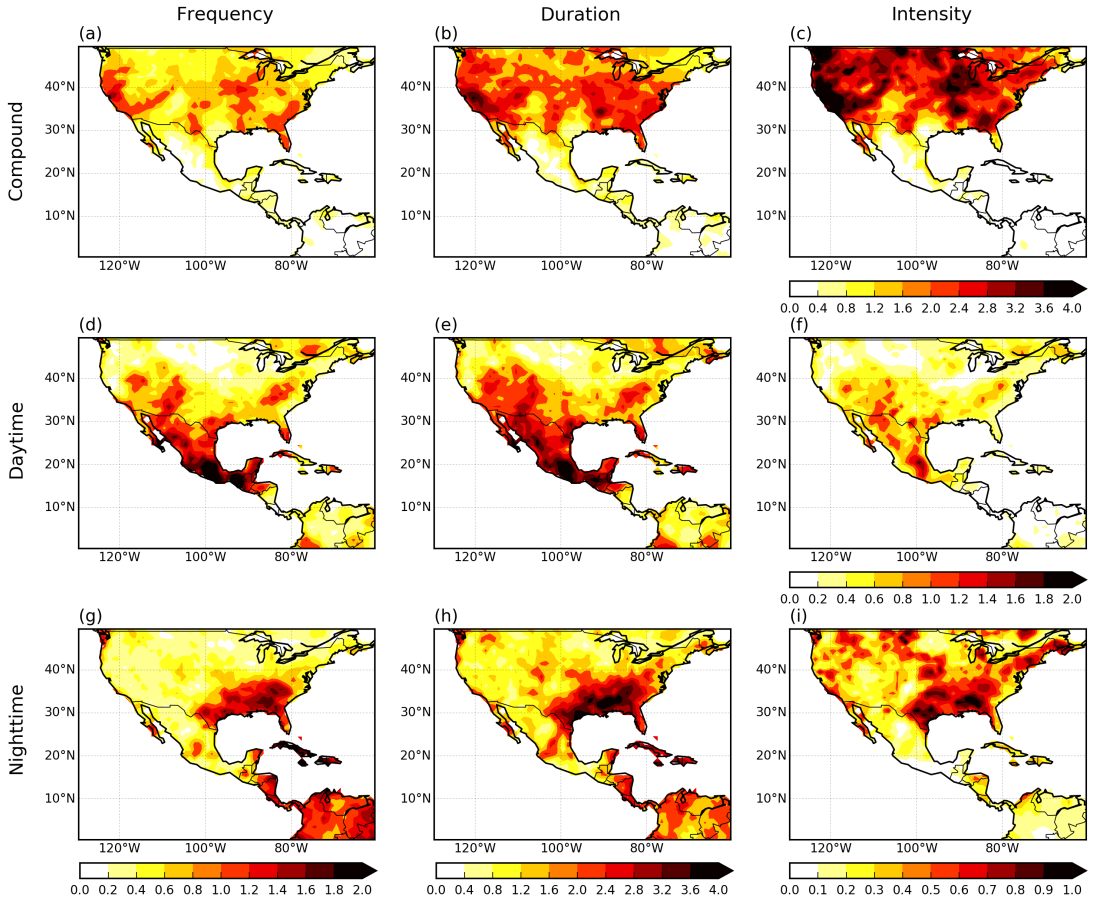

Figure 4.9: BEST 1980-2005 climatology for frequency [HWs summer^{-1}], duration [days event^{-1}] and intensity [°C HW^{-1}] of compound, daytime and nighttime heat waves

4.4.3 Identification of heat wave trends

As observed in the climatology of the analysed indicators, the largest trends of each heat wave type occur over different regions across the domain, indicating a preferred location of occurrence depending on the HW type. The frequency, duration and intensity trends for both periods (1950-1975 and 1980-2005) in each HW type (compound, daytime and nighttime) are presented for observations in Figures 4.12 and 4.13 and for the ALLF ensemble in Figures 4.14 and 4.15. An inter-comparison of the three heat wave types during the two periods is described below.

The compound HWs underwent a decrease in their frequency, duration and

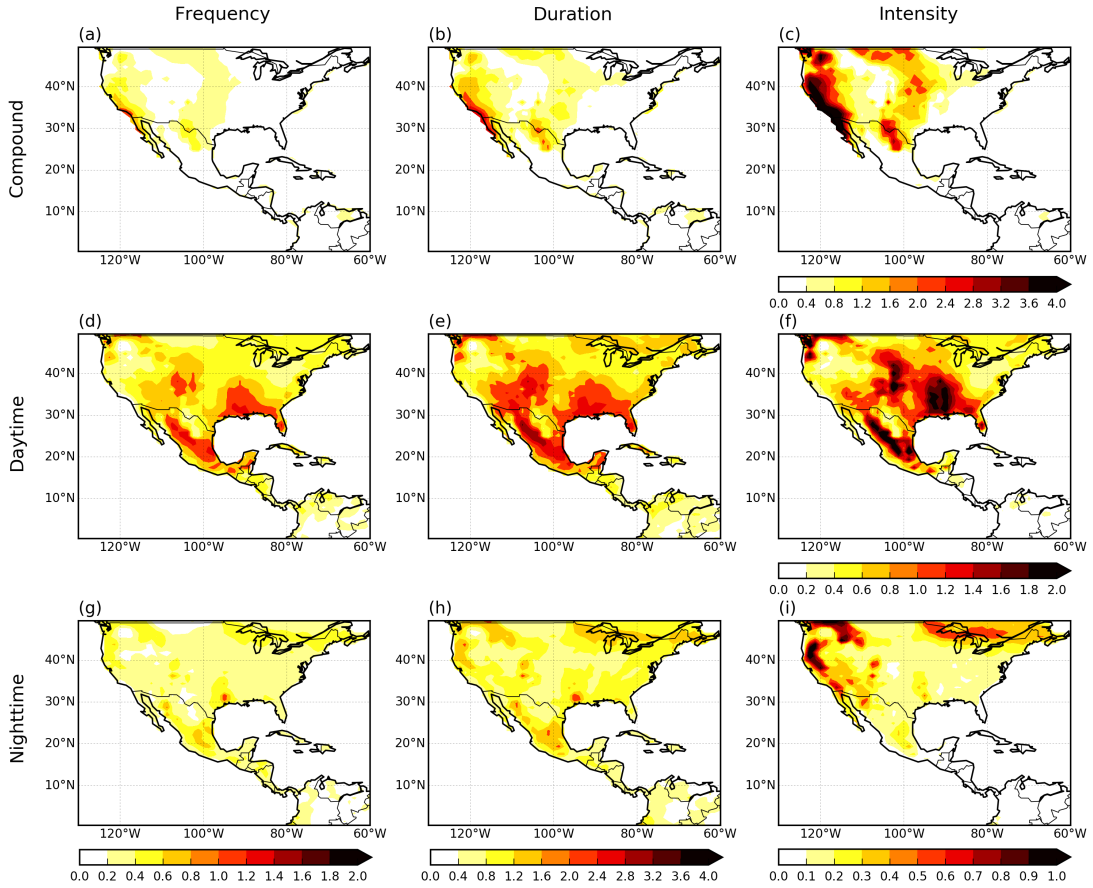

Figure 4.10: ALLF 1950-1975 climatology for frequency [HWs summer^{-1}], duration [days event^{-1}] and intensity [°C HW^{-1}] of compound, daytime and nighttime heat waves

intensity over the central US during 1950-1975 (Figure 4.12(a)-(c)). A second important (but opposite-sign) trend is observed in northwest US, where an increase in the HW frequency, duration and intensity occurs. The largest trends in the daytime HWs during this first period are found in the southeast corner of the US and northern Mexico (Figure 4.12(d)-(f)), where a strong decrease in the number of HW events per summer and their duration took place. Along with these negative trend patterns, a region of positive daytime HWF, HWD and HWI trends is found in northwest US, forming a trend dipole with the largest values in the northwest and southeast of the US. Conversely, the nighttime HWs show weak positive trends across the whole US region in the three HW indicators

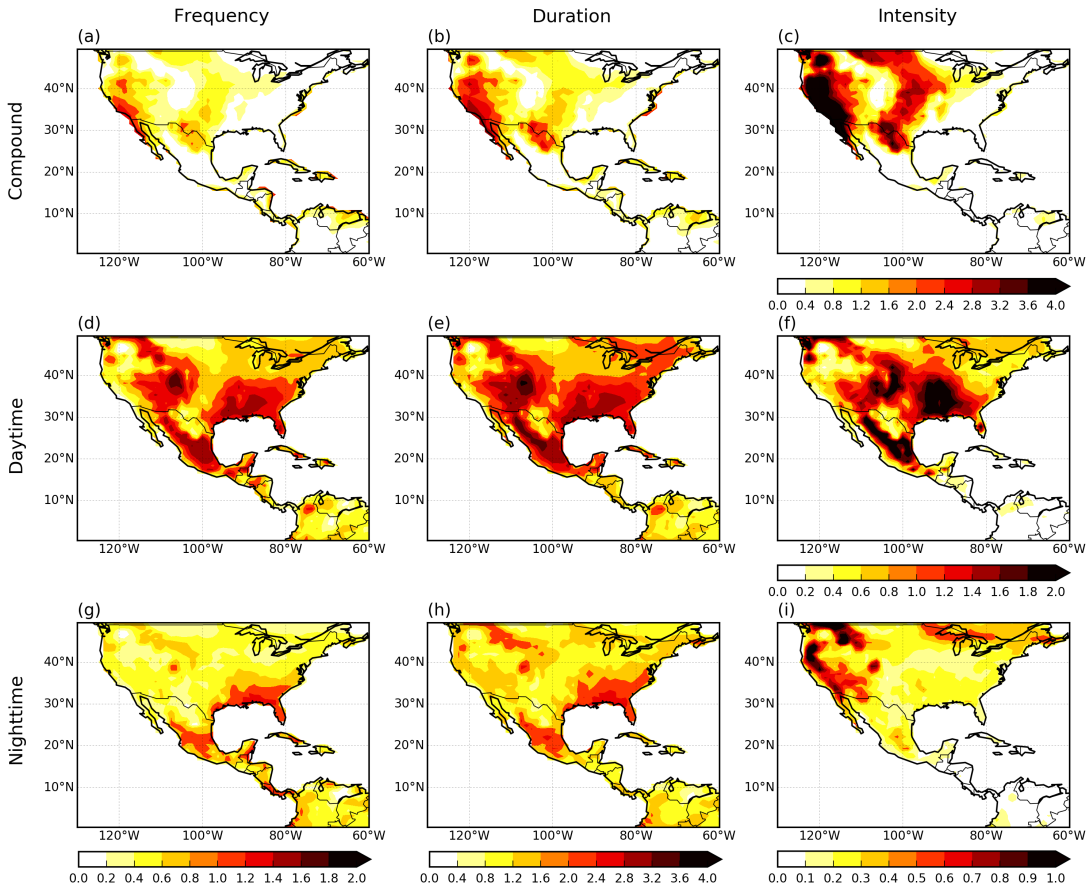

Figure 4.11: ALLF 1980-2005 climatology for frequency [HWs summer^{-1}], duration [days event^{-1}] and intensity [°C HW^{-1}] of compound, daytime and nighttime heat waves

(Figures 4.12(g)-(i)), while western Mexico exhibits negative trends in the HW's frequency, and duration. The intensity (HWI) shows little change compared to other regions within the period (e.g., trend values are ±0.5 °C per decade).

In the following decades (1980-2005), most of these features in the three HW types changed significantly. The frequency, duration and intensity of the compound HWs increased throughout most of the US (Figure 4.13(a)-(c)). In the daytime HWs (Figure 4.13(d)-(f)), the three indicators also show an increase in the frequency, duration and intensity of HWs over the southeast domain and large positive trends over the southwest US. A change in the trend sign occurred over Mexico, where large positive trends indicate more frequent, longer and more

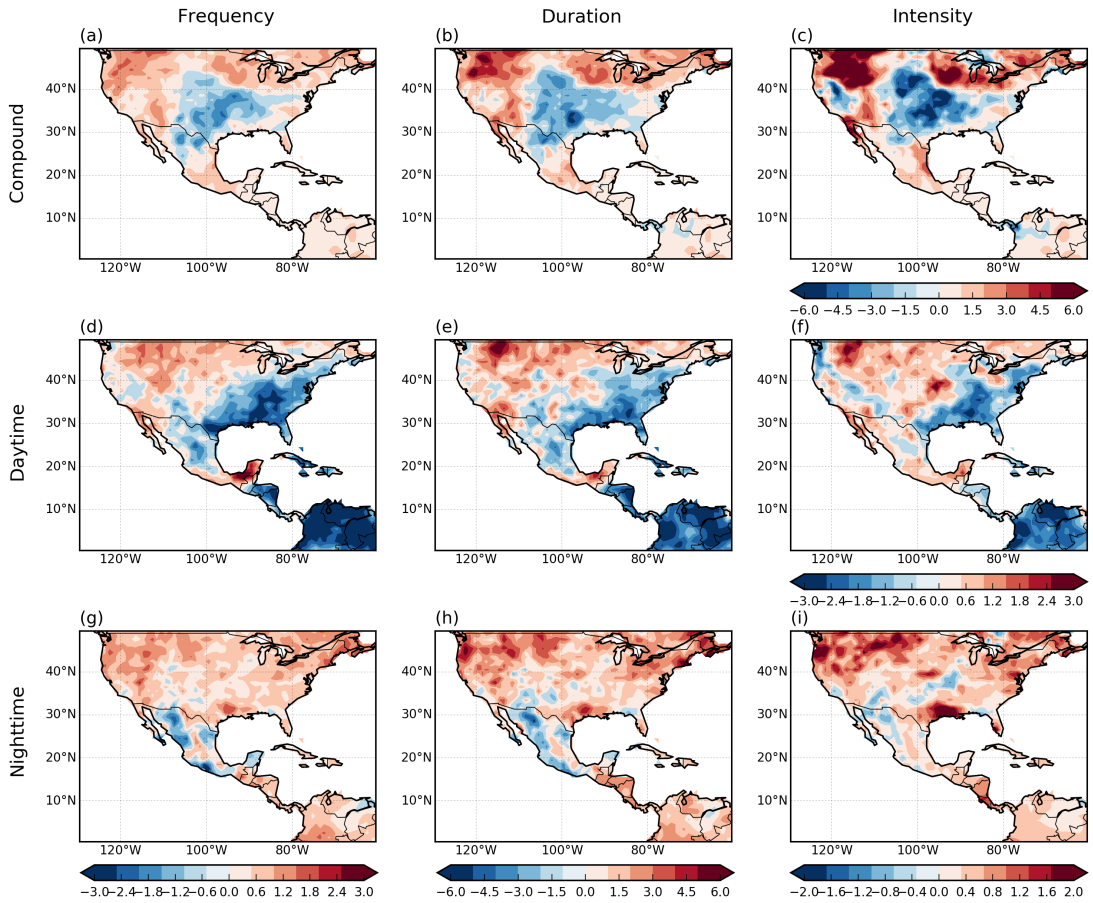

Figure 4.12: BEST 1950-1975 trends for frequency [HWs summer^{-1}], duration [days event^{-1}] and intensity [°C HW^{-1}] of compound, daytime and nighttime heat waves

intense daytime HWs during the recent period (Figure 4.13(d)-(f)). The nighttime HWs also showed significant changes with respect to the first period (Figure 4.13(g)-(i)). Over the US, a dipole with negative trends in west US and positive ones over the west US is observed in the three metrics. Over northern Mexico, there was an increase in the HWF, HWD and HWI, while opposite-sign trends were observed to the south.

The ALLF ensemble does an overall good job in simulating the HW metrics analysed, although some regional differences are found when comparing with the BEST dataset. The model reproduces the 1950-1975 negative trend pattern over the central US in the compound HWs and the positive one over the northwest US,

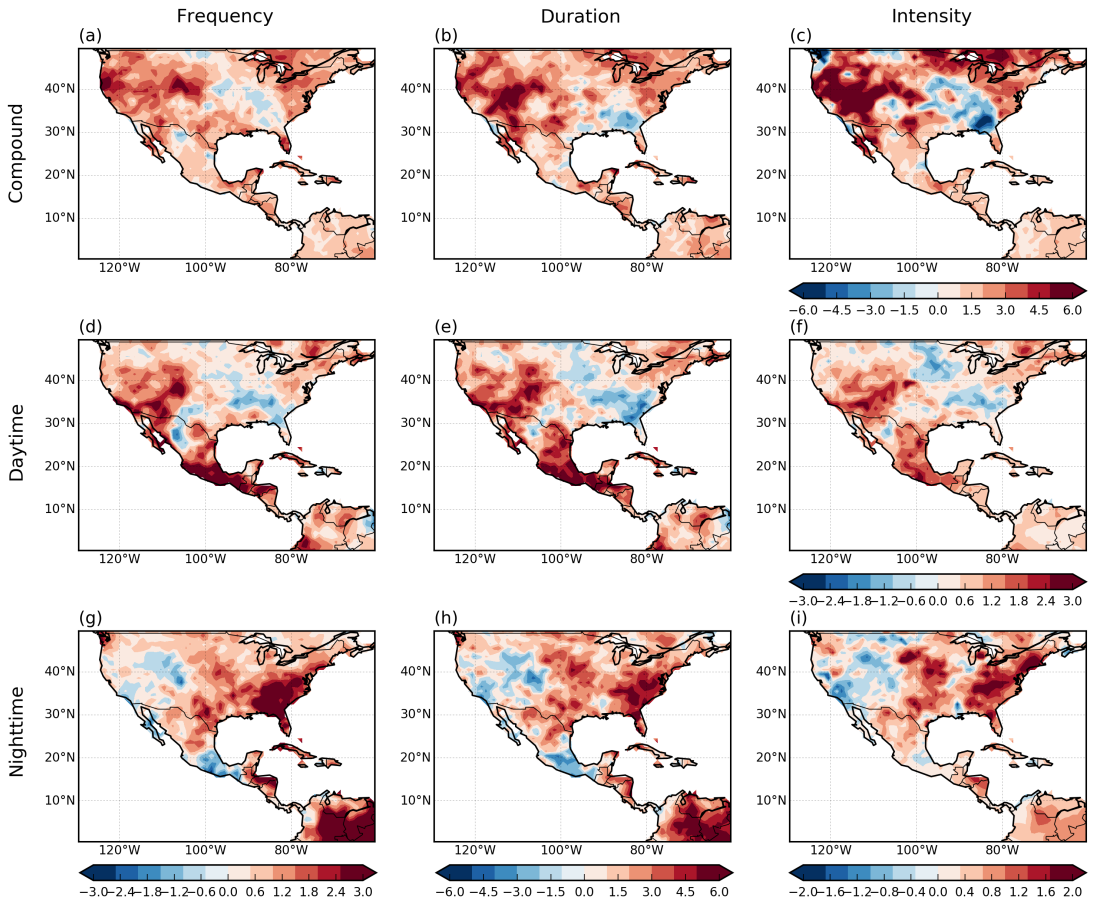

Figure 4.13: BEST 1980-2005 trends for frequency [HWs summer^{-1}], duration [days event^{-1}] and intensity [°C HW^{-1}] of compound, daytime and nighttime heat waves

although with weaker values (Figure 4.14(a)-(c)). The daytime HWs also show the observed pattern in the first period, although with the negative trend in the three metrics more spatially extended (Figure 4.14(d)-(f)). As in observations, the simulated nighttime HWs also show the smallest trends of the three HW types over the US and negative trends over some regions of northern Mexico (Figure 4.14(g)-(i)). In the second period, the magnitude and location of the largest trends is well simulated. The model shows an increase in all three metrics for the three HW types. However, it does not show some observed regional negative trends. In particular; there is no negative trends over the southeast US in the compound HWs (Figure 4.15(a)-(c)); the decrease in HW indicators over east US in the

daytime HWs is not identified (Figure 4.15(d)-(f)); and the centre of negative trend over west US in the nighttime HWs is not portrayed (Figure 4.15(g)-(i)).

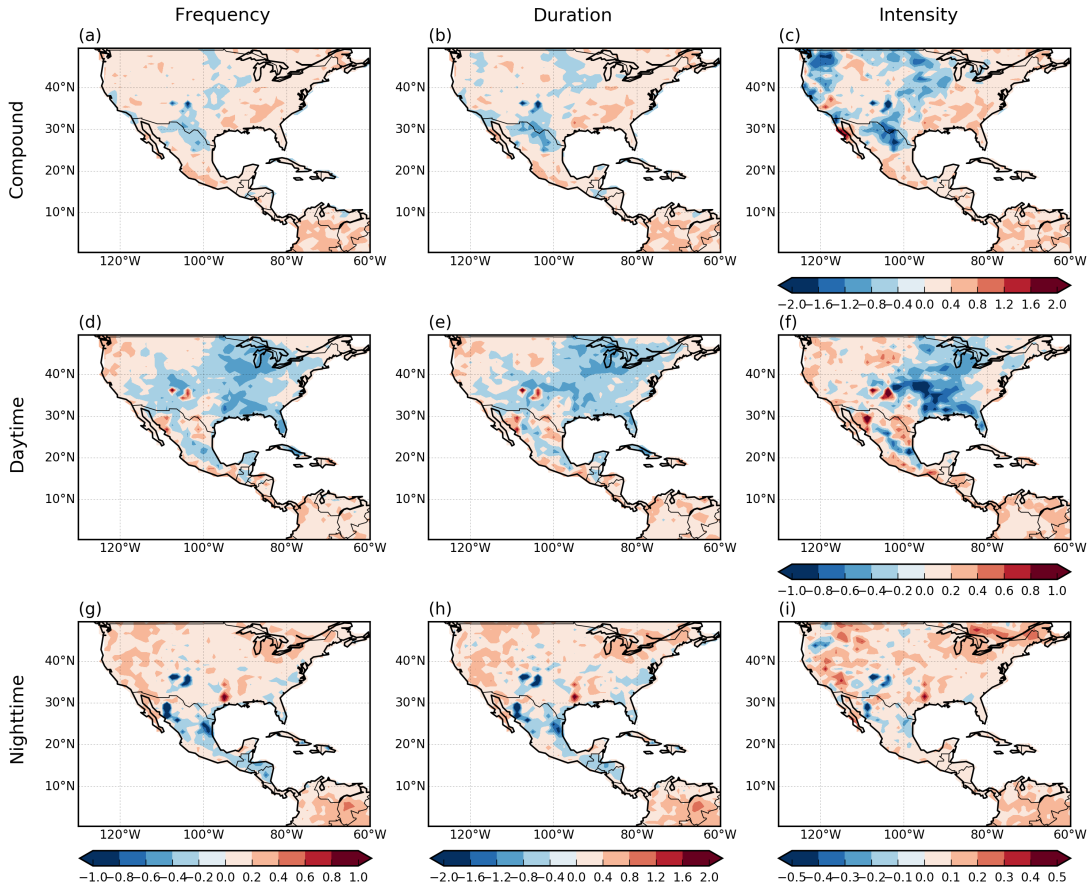

Figure 4.14: ALLF 1950-1975 trends for frequency [HWs summer^{-1}], duration [days event^{-1}] and intensity [°C HW^{-1}] of compound, daytime and nighttime heat waves

4.4.4 Simulated responses of heat wave metrics to anthropogenic aerosols and greenhouse gases

In this section we will identify the contribution of single anthropogenic forcing agents to changes in HWs during each period. In Figures 4.16 to 4.19, we present the spatial trend patterns of frequency, duration and intensity for the three types of heat waves in response to the individual forcing from anthropogenic aerosols and

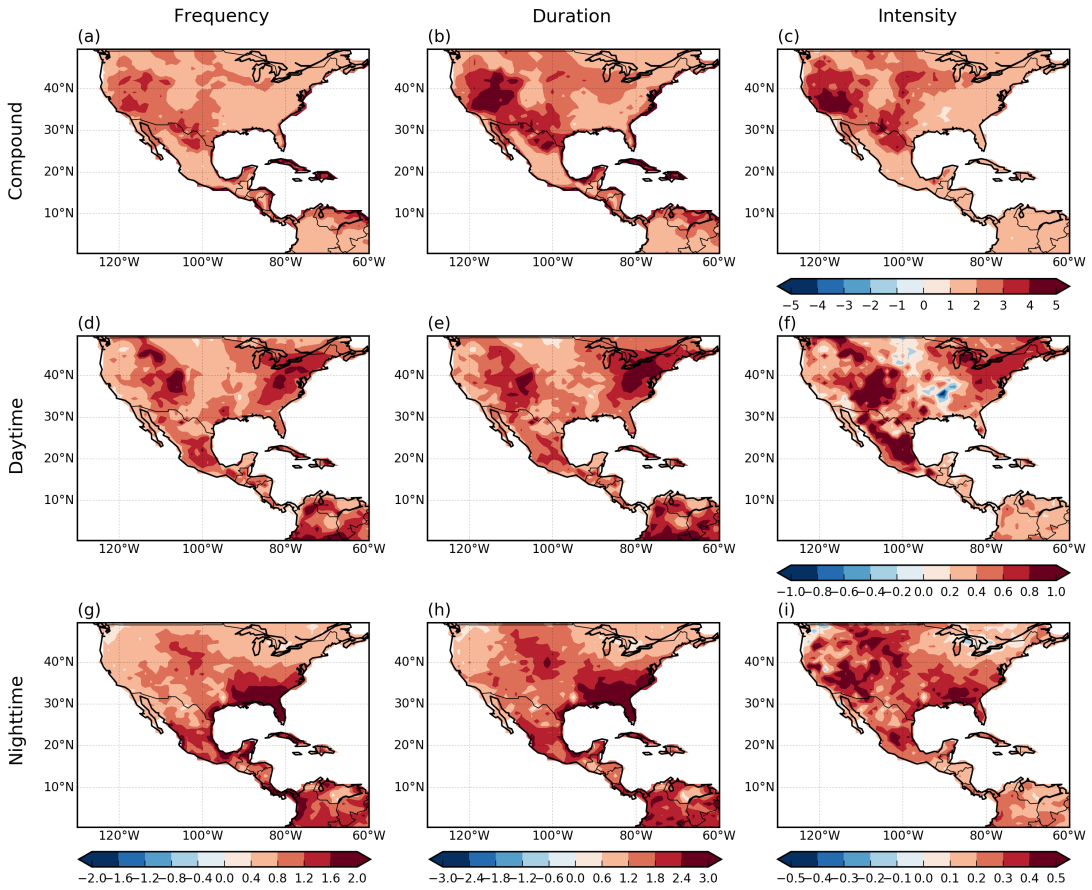

Figure 4.15: ALLF 1980-2005 trends for frequency [HWs summer^{-1}], duration [days event^{-1}] and intensity [°C HW^{-1}] of compound, daytime and nighttime heat waves

greenhouse gases for each analysed period. These isolated signals were obtained from subtracting the XAER and XGHG from the ALLF simulations, respectively.

During 1950-1975, the increase in aerosol emissions dominated the daytime HWs response to external forcing over most parts of the study domain (Figure 4.16(d)-(f)), while the other two HW types show a regional dependence to the dominating forcing. In the compound HWs, both, aerosols and GHGs show the largest trend values over central and west US, although of opposite sign (negative for aerosols and positive for GHGs, Figures 4.16(a)-(c) and 4.17(a)-(c)). However, in central US the factor dominating the trends is the aerosol forcing, while GHGs are stronger over west US. In the nighttime HWs, there is a strong influence of aerosols, particularly over the southeast US and Mexico (Figure 4.16(g)-(i)). Over

the southeast US, however, their effect is cancelled out by GHGs (Figure 4.17(g)-(i)), resulting in homogeneously weak positive trends in the ALLF simulations there (Figure 4.14(g)-(i)).

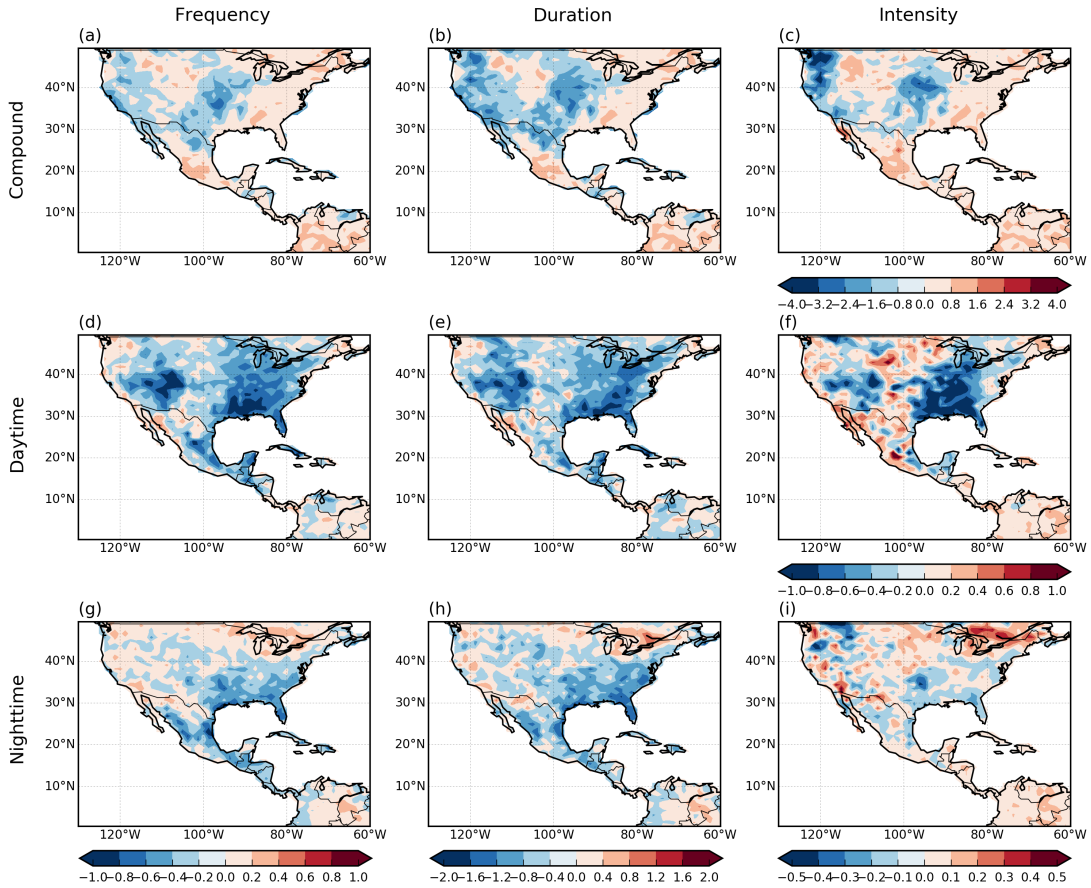

Figure 4.16: ALLF-XAER 1950-1975 trends for frequency [HWs summer^{-1}], duration [days event^{-1}] and intensity [°C HW^{-1}] of compound, daytime and nighttime heat waves

In the period from 1980 to 2005, there is a clear warming signal in all three HW types over the whole analysed domain, although with some regional enhancements (Figure 4.15). The resemblance of all three HW types of the GHGs experiments (Figure 4.19(a)-(i)) with those of the ALLF is evident, indicating a dominant role of the GHGs during this second period. The largest trends forced by the GHGs are located over the northern Mexico, west and central US in the compound HWs (Figure 4.19(a)-(c)); in the northeast US and over a meridional corridor

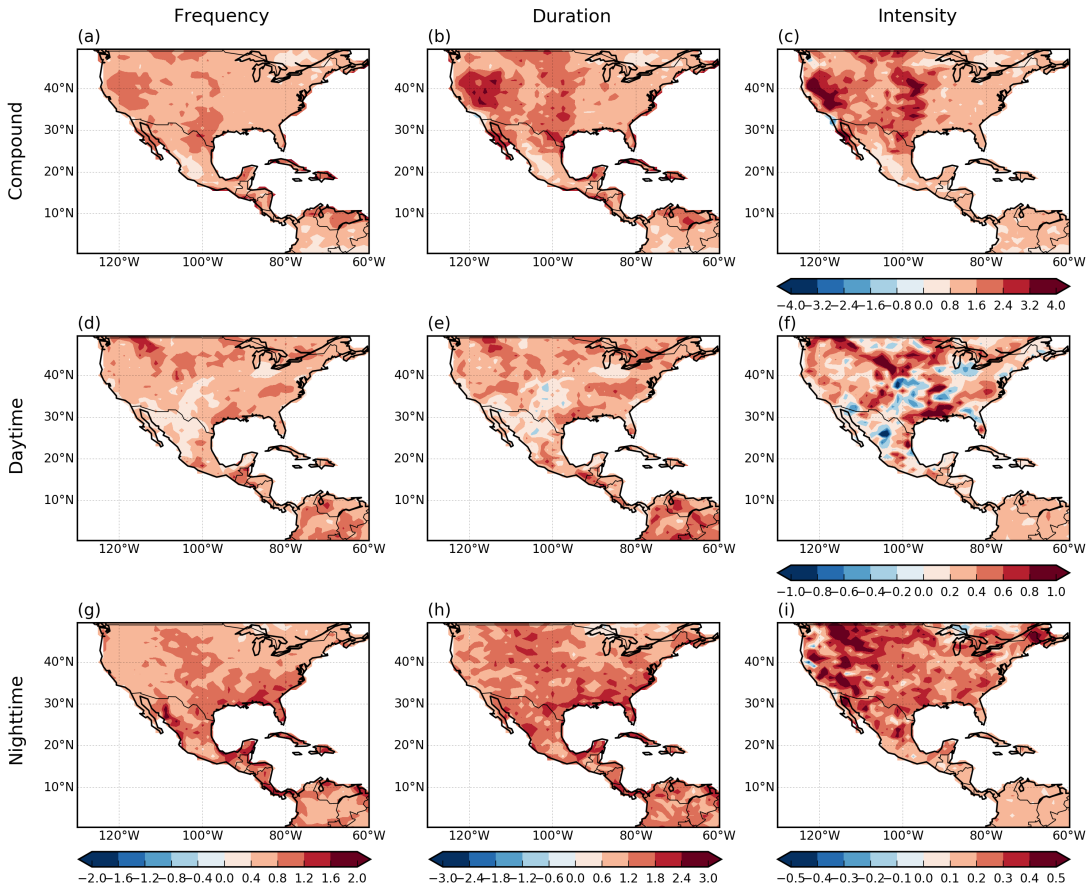

Figure 4.17: ALLF-XGHG 1950-1975 trends for frequency [HWs summer^{-1}], duration [days event^{-1}] and intensity [°C HW^{-1}] of compound, daytime and nighttime heat waves

that crosses Mexico and the US from 100 to 115°W in the daytime HWs (Figure 4.19(d)-(f)); and in the southeast US and southern Mexico in the nighttime type (Figure 4.19(g)-(i)). The aerosols decrease due to air quality regulations in North America from the 1990s also contributed to the increase in surface temperature (Leibensperger et al. 2012) and to the subsequent increase in extreme hot events (Wang et al. 2020), reinforcing the positive trends, particularly those of daytime HWs (Figure 4.18(d)-(f)).

Notably, we find that the sign of the trend and relative contribution from aerosols changed from one period to the other throughout the domain, in response to their temporal evolution (increasing in the first period and decreasing in the

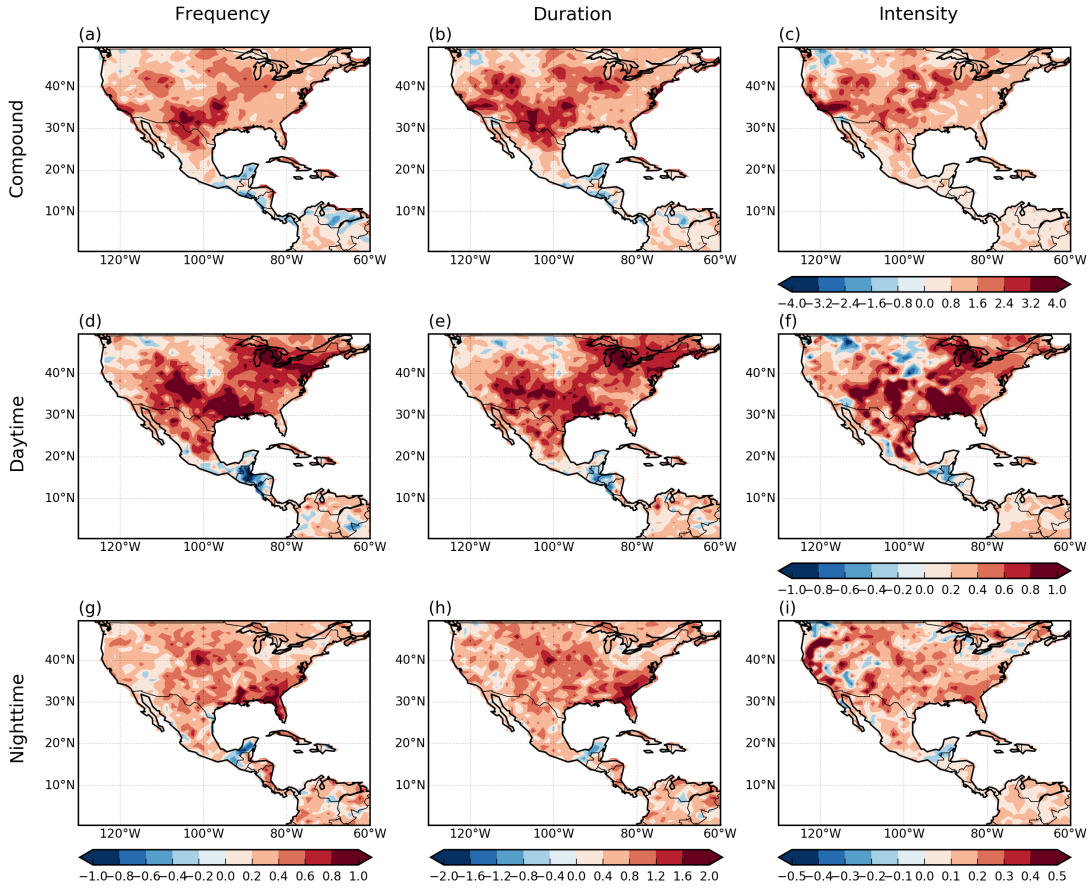

Figure 4.18: ALLF-XAER 1980-2005 trends for frequency [HWs summer^{-1}], duration [days event^{-1}] and intensity [°C HW^{-1}] of compound, daytime and nighttime heat waves

second one). The contribution from GHG, on the other hand, shows a general increase in the magnitude of the trends towards the second period, in line with the current global warming trend.

4.4.5 Dynamics of heat wave changes

Our results show an overall increase in the HW metrics in most of the analysed domain during the recent period, hinting to substantial changes in the atmospheric conditions and associated forcing. Argüeso et al. (2016) showed that seasonal mean temperature changes –rather than changes in temperature variability– are the main contributor to heat wave changes in most regions of the globe.

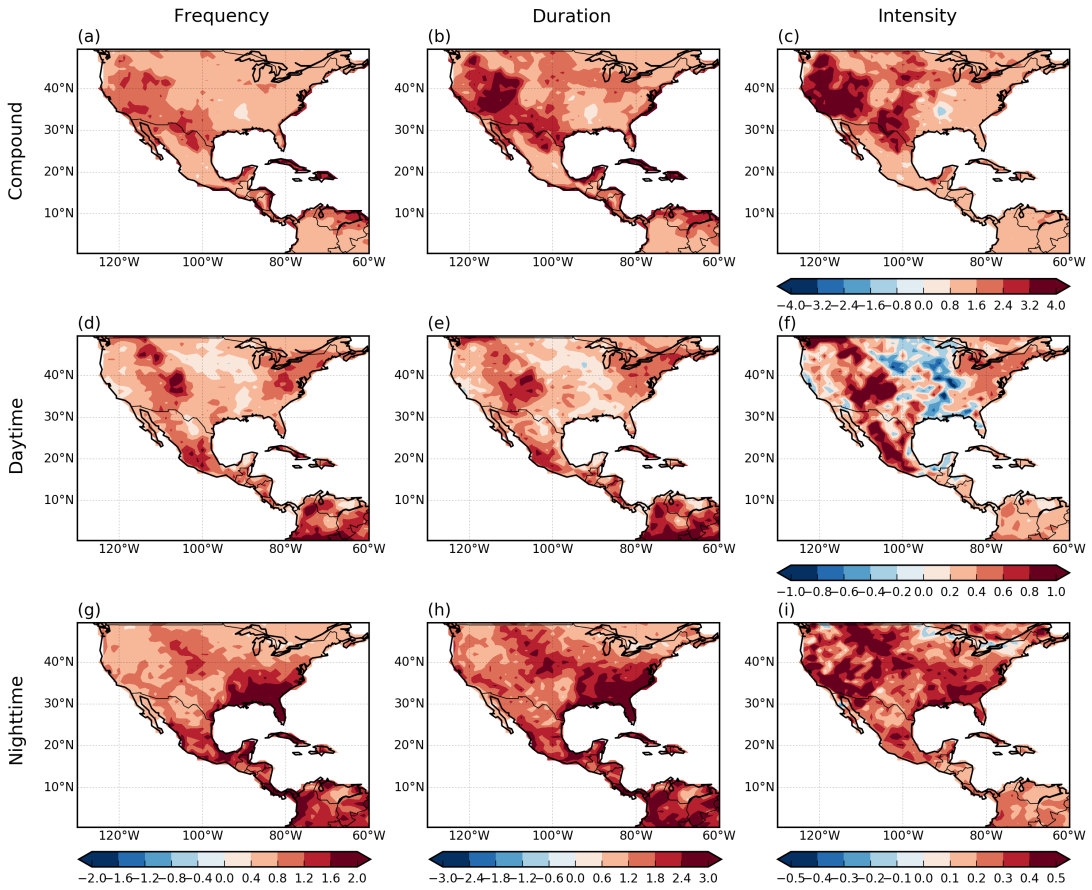

Figure 4.19: ALLF-XGHG 1980-2005 trends for frequency [HWs summer^{-1}], duration [days event^{-1}] and intensity [°C HW^{-1}] of compound, daytime and nighttime heat waves

It is therefore reasonable to analyse the summer-mean state of key fields to better understand the physical mechanisms associated with changes in the HW characteristics. Below we analyse the mechanisms associated with the changes induced by aerosols and GHGs in each of the three HW types.

The summer linear trends for key fields in response to aerosol changes are shown in Figure 4.20. The 1950-1975 aerosol increase is clearly recognisable in the SO_4 burden, where a significant positive trend is found over the east US (Figure 4.20(a)). There is a subsequent decrease in the net shortwave flux at the surface (Figure 4.20(b)), caused by surface dimming from the aerosol direct effect. As a result, surface temperature (mean and maximum) decreases during this

period (Figure 4.20(c)-(d)). Along with these changes, an increase in low cloud cover is found over the core aerosol emission region and surroundings (east and central US, Figure 4.20(e)) due to an increase in cloud condensation nuclei (CCN) there. These cloud changes are accompanied by an increase in the droplet number concentration (Figure 4.20(f)), due to more CCN being available. Also, with more CCN present, precipitation becomes less efficient (as raindrop formation occurs more slowly, Figure 4.20(g)) and the total cloud liquid water path, and therefore the droplet effective radius, increase (Figure 4.20(h)-(i)). These changes suggest the large negative trends in the frequency, duration and intensity of daytime and compound heatwaves to be the result of important aerosol-radiation interactions. During 1980-2005, with aerosols significantly decreased, these variables show, in general, opposite-sign trends, pointing to the same response to aerosols but in the opposite direction.

Figure 4.21 shows the summer linear trends for key fields forced by the evolution of GHGs during 1980-2005. The continuous rise in GHG emissions warms the atmosphere throughout the domain (the greenhouse effect), inducing a significant increase in the longwave net radiation at the surface (Figure 4.21(a)). This warming effect is further enhanced by an increase in the moisture available at low levels, particularly over the eastern and northern halves of the US (Figure 4.21(b)). Theses changes in the radiative fluxes are evident in the maximum and minimum temperatures (Figure 4.21(c)-(d)), where significant warming is observed in the whole analysed domain, with the largest trends localised over the land (in western US and southern Mexico for TX and in southeast US for TN). A GHG-driven polar expansion of the Hadley cell and the amplified land-sea thermal contrast cause changes in the local circulation. The North Atlantic Sub-tropical High pressure system strengthens (Figure 4.21(f)), favouring more moisture transport from the Gulf of Mexico into the southeast US, and its convergence over this continental region. In addition, the warmer land surface increases evaporation in most parts of this region (Figure 4.21(e)), allowing cloud

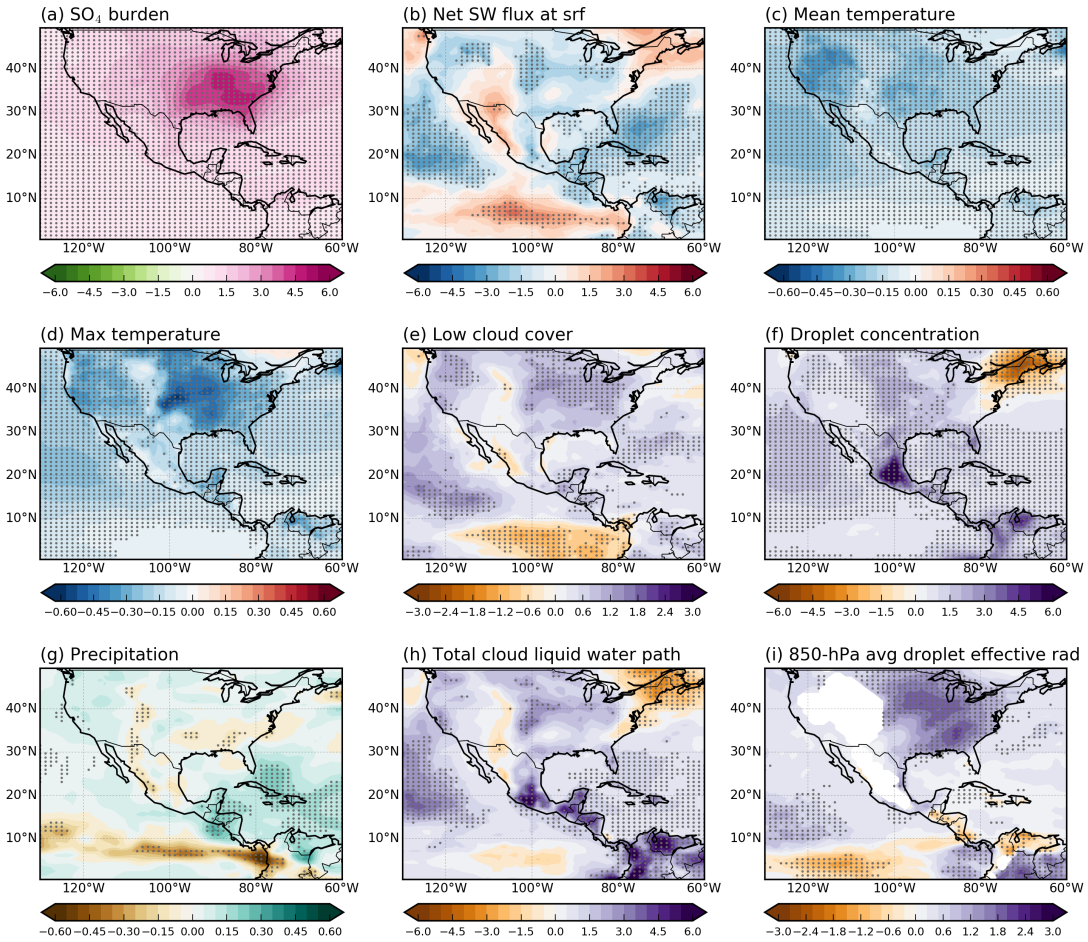

Figure 4.20: ALLF-XAER 1950-1975 summer trends for: (a) sulphate burden [(10^{-6} kg m^{-2}) decade^{-1}], (b) net shortwave radiation at the surface [(W m^{-2}) decade^{-1}], (c) mean temperature [°C decade^{-1}], (d) maximum temperature [°C decade^{-1}], (e) low cloud cover [% decade^{-1}], (f) vertically integrated droplet concentration [10^{9} m^{-2} decade^{-1}], (g) precipitation [(mm day^{-1}) decade^{-1}], (h) total cloud liquid water path [(g m^{-2}) decade^{-1}] and (i) 850-hPa average droplet effective radius [10^{-2} μm decade^{-1}]. In (b), negative values are upward fluxes and indicate cooling. The topography is masked out in (i). The significance of the trends difference (ALLF-XAER) at the 95% confidence level is stippled

formation (Figure 4.21(g)), and leading to enhanced precipitation (Figure 4.21(h)) and decreased shortwave radiation at the surface (Figure 4.21(i)). Conversely, the northerly and northeasterly flow of the NASH diverges off the east US coast, inhibiting cloud formation and, therefore, reducing precipitation there. The above changes highlight the direct effect of GHG on the surface temperature

(mean, maximum and minimum) and thus on HWs, and show the pathways of their associated feedbacks, in particular, the strong response of the atmospheric circulation to GHG forcing. Specifically, the greenhouse effect directly influences the frequency, duration and intensity of all three types of HWs, whereas the changes in the atmospheric circulation indirectly reinforce the positive HW trends through increasing moisture availability and triggering a positive feedback.

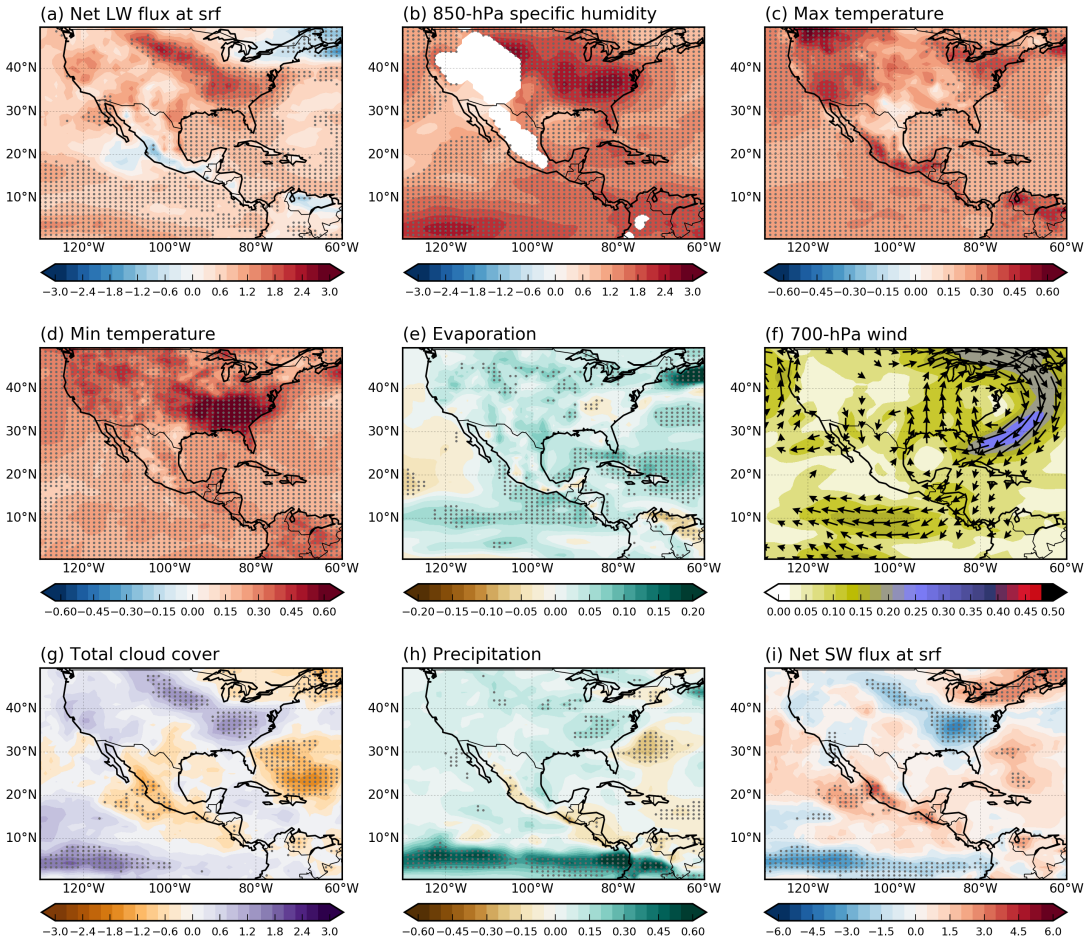

Figure 4.21: ALLF-XGHG 1980-2005 summer trends for: (a) net longwave radiation at the surface [(W m^{-2}), (b) 850-hPa specific humidity [(10^{-4} kg kg^{-1}) $decade^{-1}$], (c) maximum temperature [°C $decade^{-1}$], (d) minimum temperature [°C $decade^{-1}$], (e) evaporation [(mm day^{-1}) $decade^{-1}$], (f) 700-hPa wind [(m s^{-1}) decade $^{-1}$], (g) total cloud cover [% $decade^{-1}$], (h) precipitation [(mm day^{-1}) $decade^{-1}$] and (i) net shortwave radiation at the surface [(W m^{-2}) $decade^{-1}$]. In (a) and (i), negative values are upward fluxes and indicate cooling. The topography is masked out in (b). The significance of the trends difference (ALLF-XAER) at the 95% confidence level is stippled

4.5 Summary, discussion and conclusions

In this work we characterised three independent heat wave types (compound, daytime and nighttime) over Mexico and the US during the summers (June-August) of two periods with different historical anthropogenic forcing: 1950-1975 and 1980-2005. The characterisation was done based on three fundamental

HW metrics: frequency, duration and intensity. The relative contribution from anthropogenic aerosols and greenhouse gases was evaluated by contrasting the single-forcing ensembles (of 20 members each) with the all forcing one (40 members). Observations from the BEST dataset were used to validate the CESM-LENS results.

The three types of heat waves in the ALLF simulations exhibit a marked change from the first to the second period, with the frequency, duration and intensity increasing in the recent period over most regions of the domain. Each HW type, however, shows a preferred location of occurrence. The compound HWs show the largest changes over northern Mexico, west and central US. The daytime type is most recurrent over east US, the south-central US states and in Mexico. For the nighttime, the regions with the largest changes are the southeast US, central and southern Mexico. We also found that an increase/decrease in the HW frequency is usually accompanied by an increase/decrease in the duration and intensity in all three HW types. This indicates that the severity of the HW events increases/decreases as a result of the three indicators changing concurrently.

The results from the single-forcing ensembles prove a strong influence from anthropogenic origin on the HW changes in the second half of the 20^{th} century. During 1950-1975, the increase in aerosol emissions dominated the daytime HWs response to external forcing over most parts of the study domain, while the other two HW types show a regional dependence to the dominating forcing. In 1980-2005, the spatial patterns of trends driven by GHG forcing are remarkably similar to those of the ALLF, exhibiting a strong dominance of the greenhouse gases during the second period in all three HW types.

The aerosols increase (mainly of the sulphate type) during 1950-1975 triggered a series of changes in the radiative fluxes, cloud properties and ultimately in the temperature field. These identified changes suggest that the large negative trends in the frequency, duration and intensity of daytime and compound heatwaves during this period are the result of important aerosol-radiation interactions. On

the other hand, the significant positive trends in the HW indicators of all three HW types during 1980-2005 are the result of a strengthened greenhouse effect and the atmospheric circulation response to the GHG forcing. In addition, the negative trend in aerosol emissions during the latter period also contributed to the increase in the HW indicators.

We found that the mean states and the linear trends of the HW metrics analysed here are highly dependent on the HW type and the region considered. This shows the importance of using distinct HW definitions to properly identify the more recurrent HW type in each region and therefore to develop regionally-customised strategies for adaptation and mitigation to the these climate extreme events. Informed planning can help to significantly reduce public health impacts (Allen et al. 2018).

By using the CESM large ensemble we were able to distinguish the relative contribution of internal variability from that of external forcing with some confidence. In addition, the analysis of single-forcing experiments, allowed us to attribute the changes in the frequency, duration and intensity of the HWs to the evolution of anthropogenic aerosols and greenhouse gases. Another novel contribution for improving the HW characterisation in the region is the classification of HWs into three non-overlapping types. The compound, daytime and nighttime HWs presented different responses to anthropogenic forcing and are associated with diverse mechanisms. Changes considering these different HW types have not been studied before over some regions in the domain (e.g., in Mexico). We aim to help filling this knowledge gap.

As mentioned above, by using large ensemble simulations (40 members in ALLF and 20 members in XAER and XGHG), we gain confidence in the robustness of the results. Nevertheless, the use of other models with different physical parameterisations would be useful to confirm our findings. We investigated the role of anthropogenic forcing on the HW metrics, however, other factors such as land use and land cover changes have also been found to be related to recent

global heat wave trends (Findell et al. 2017). As GHGs are expected to continue to increase globally throughout the 21^{st} century (Wang et al. 2020), extending this analysis to the near and end-of-the-century future under different emission scenarios will aid in identifying and better preparing for the range of possible climate hot extremes.

Appendix

4.A Supplementary figures

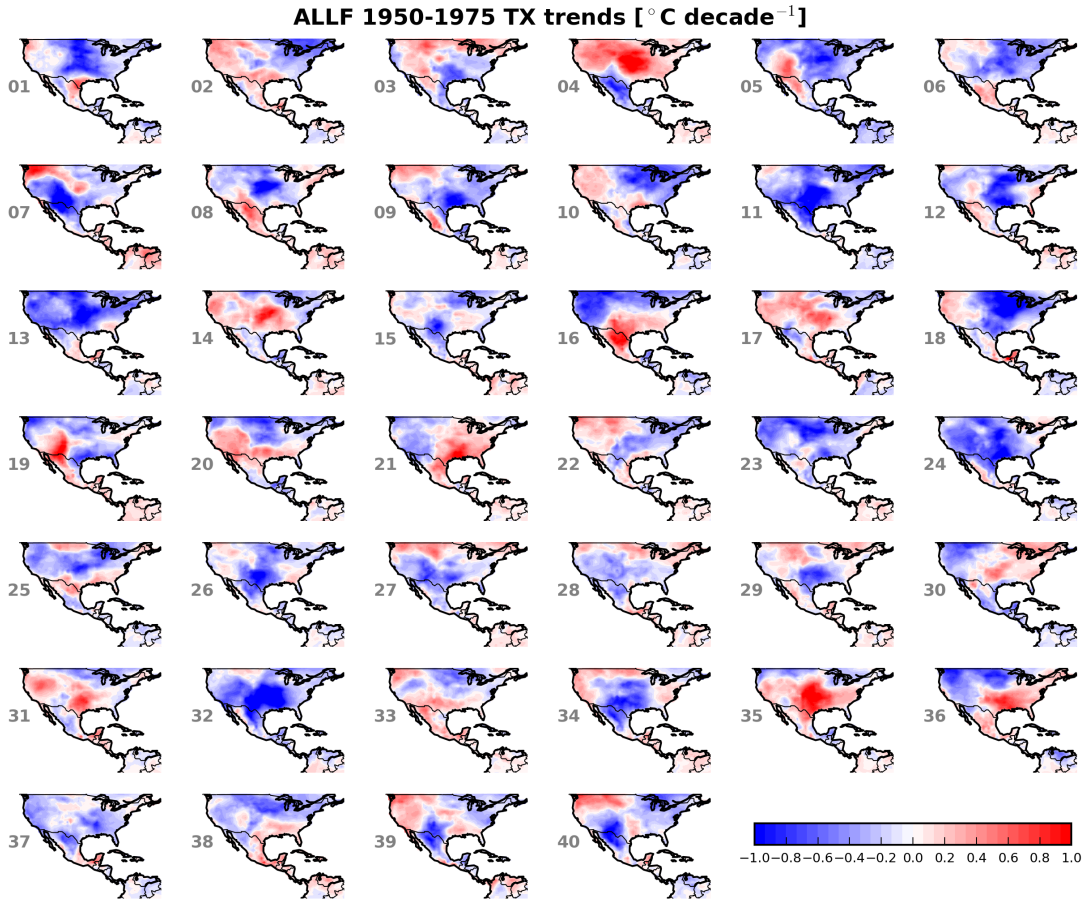

Figure 4.A.1: Summer 1950-1975 TX trends [°C decade^{-1}] from each of the 40 ALLF CESM-LENS ensemble members

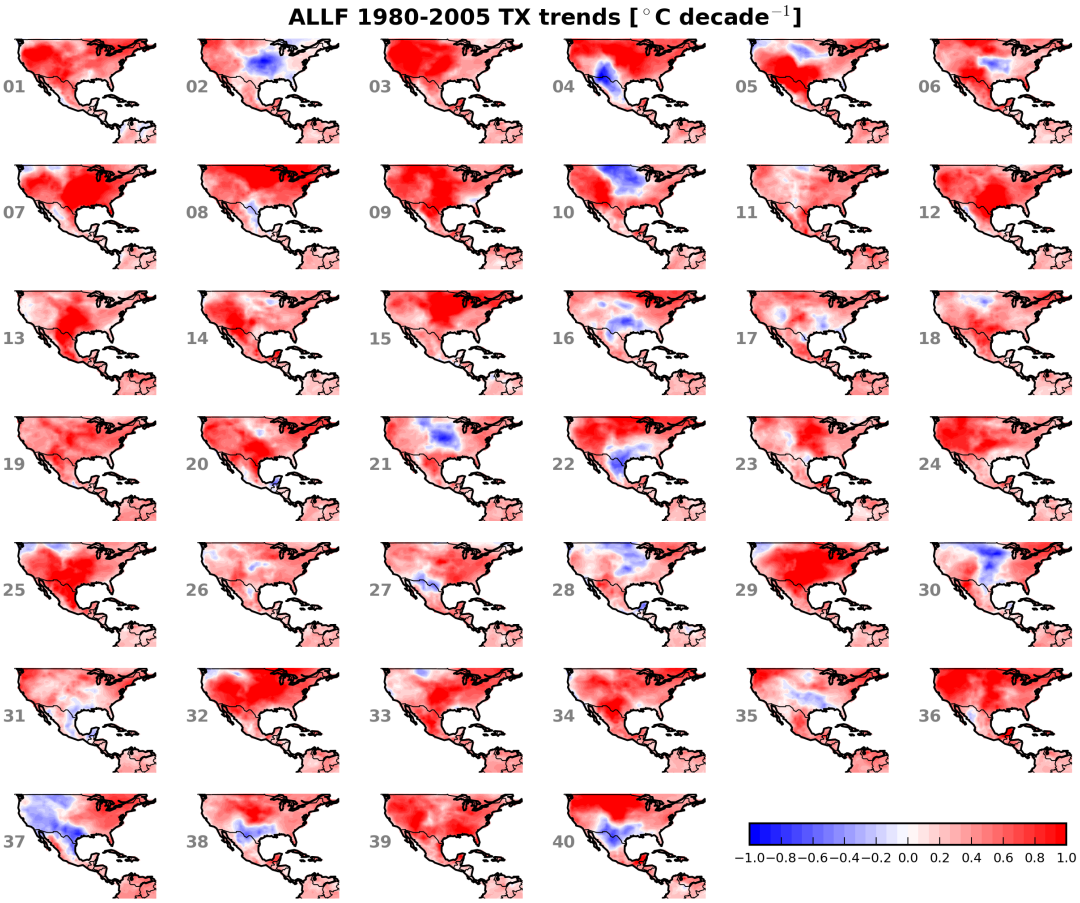

Figure 4.A.2: Summer 1980-2005 TX trends [°C decade^{-1}] from each of the 40 ALLF CESM-LENS ensemble members

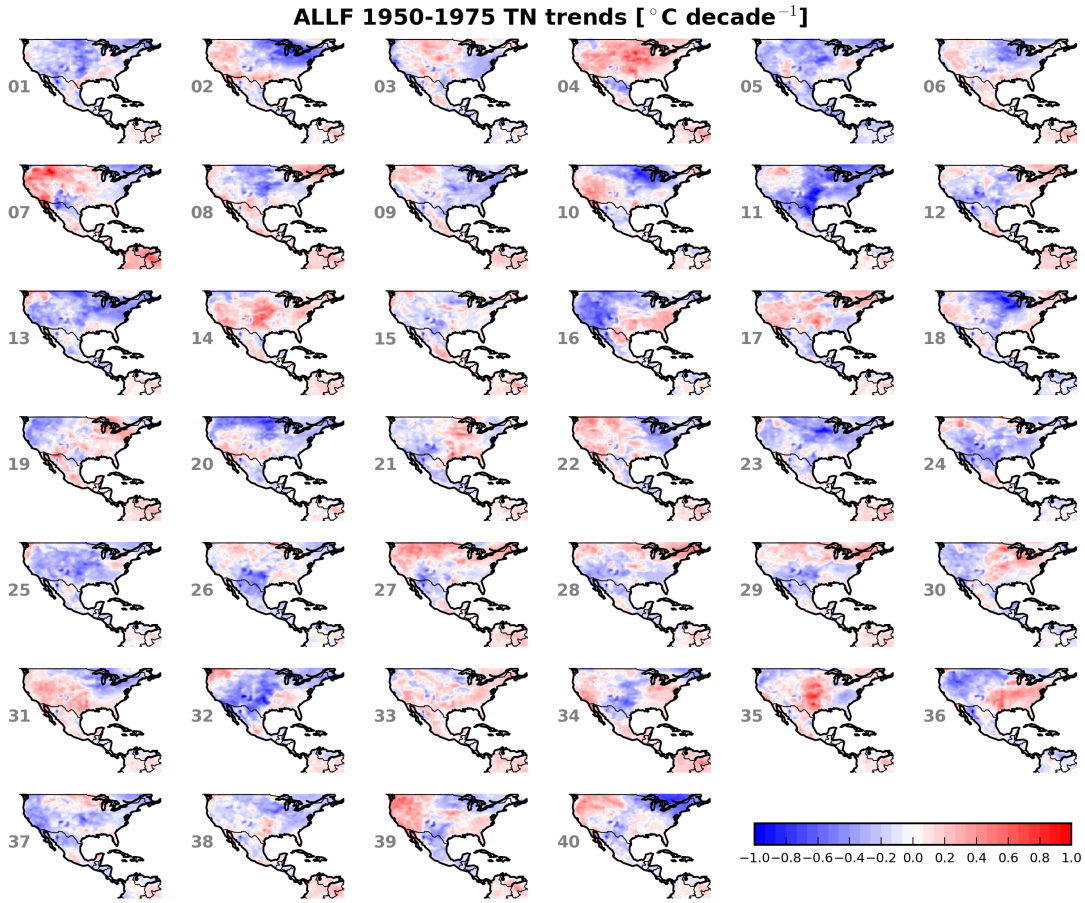

Figure 4.A.3: Summer 1950-1975 TN trends [°C decade^{-1}] from each of the 40 ALLF CESM-LENS ensemble members

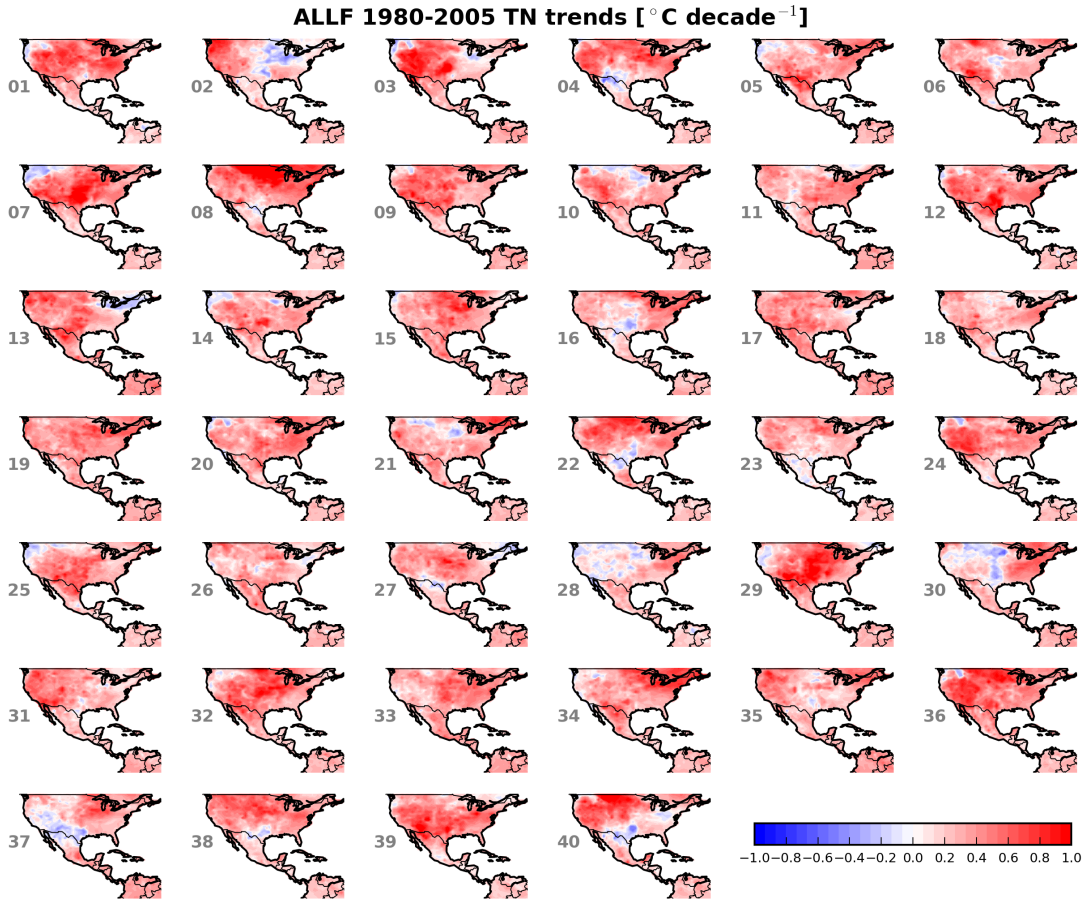

Figure 4.A.4: Summer 1980-2005 TN trends [°C decade^{-1}] from each of the 40 ALLF CESM-LENS ensemble members

Chapter 5

Concluding remarks

5.1 Summary

This PhD thesis addresses the mechanisms of summer climate variations over Central America, Mexico and the United States. A fundamental role of the regional atmospheric circulation and anthropogenic forcing in the mean and extreme climate variations was identified. First, the sub-seasonal variations of a key feature of the regional atmospheric circulation, the Caribbean Low-Level Jet, and their relationship to the hydroclimate are studied in Chapter 2. The impact of antropogenic aerosols in the regional and large-scale summer climate are then described in Chapter 3. Finally, the thesis is complemented with a characterisation of the recent changes in heat waves, their anthropogenic drivers and mechanisms in Chapter 4.

The sub-monthly spatio-temporal evolution of the CLLJ in the summertime was characterised by means of the extended empirical orthogonal function analysis and lead/lag linear regressions. This approach proved to be useful in revealing novel details in the dynamical processes of the jet evolution and its climate links. Among these links, the existence of key relationships with antecedent and lagged anomalies (which helped to identify the triggers of the summer intensification of the CLLJ and the oceanic lagged responses), the interaction of the jet with

large-scale dynamical circulation features (such as that with the North Atlantic sub-tropical high) and the role of inter-basin links between the Atlantic and the Pacific Oceans (which in turn showed to feedback on the CLLJ evolution) were elucidated. In addition to forcings of regional origin, the influence of two major modes of tropical variability, the el Niño Southern Oscillation and the Madden-Julian Oscillation, were found to be important contributors to the atmospheric circulation changes over the Caribbean. The CLLJ evolution and the climate response were shown to be robust across various observational datasets. A significant contribution of this analysis is the integral mechanistic depiction of the CLLJ evolution and its associated climate relationships. This had not been addressed before. Moreover, the identification of these links has important implications for the predictability of regional rainfall extreme events, such as flash floods and droughts.

The summer climate response to increased North American sulphate aerosol emissions was investigated in the Community Earth System Model. Two sets of experiments (of eight members each) with and without the post-industrial evolution of North American aerosol emissions were used. The aerosol-driven changes were identified by contrasting the linear trends of the ensemble-mean atmospheric fields in the two sets of experiments. This approach, although simple, proved to be appropriate as the aerosol emissions showed a near-linear increase during their highest peak (1950-1975). Our results evidence that the sharp 1950-1975 increase in North American sulphate aerosols had considerable regional and remote effects. A comprehensive analysis of the aerosol-radiation-cloud interactions, the surface and upper-level climate and atmospheric circulation anomalies allowed us to shed light on the physical mechanisms behind the aerosol-driven changes. In particular, we identified a prominent role of dynamical adjustments in the atmospheric circulation and of the interplay between local and remote influences in realising the impact of North American aerosols. This is one of the first studies describing with some detail the mechanisms of the

aerosol-induced changes on both regional and large-scale climate. With aerosol emissions (in particular of sulphates) considerably reduced in North America, and the expectation of a continued global decline in the following decades, the prominent role of North American aerosols and their large-scale footprint found here can help to narrow down the uncertainty in near-future projections of regional climate variability.

The noteworthy fingerprint of anthropogenic influence on the regional extreme climate variations was also evidenced. We distinguished the changes in frequency, duration and intensity of compound, daytime and nighttime heat waves during the second half of the 20^{th} century. To this end, we used three sets of simulations from the CESM-Large Ensemble (with all forcings, no evolving aerosols and no evolving GHGs). By using a large number of simulations (of up to 40 members), the role of internal variability on the changes in temperature extremes was assessed with some confidence. A novel contribution for improving the HW characterisation in the region is the classification of HWs into three non-overlapping types. Based on both, model outputs and observations, we showed that all the three HW types became considerably more frequent, longer-lasting and more intense in the recent decades. Notably, each HW type showed a preferred location of occurrence. The impacts on human health and ecosystems and the associated physical mechanisms have been shown to be different for each heat wave type. Hence, we argue the critical importance of distinguishing among the distinct HW types to properly characterise these hot extremes in the region. By contrasting the all-forcing and the single-forcing ensembles, we identified a dominant role of anthropogenic forcing on the changes in hot extremes. Noticeably, the relative role of GHGs and aerosols showed substantial changes over the second half of the 20^{th} century, with aerosols dominating the HW changes during 1950-1975, and the GHGs the following decades. A deeper understanding of these extreme events can be used for developing regionally-customised trustworthy future climate projections.

5.2 Limitations and recommendations for future research

This PhD research was aimed to be as comprehensive as possible within the time limits and available resources. Nevertheless, we faced some limitations, mainly related to data issues and the difficult decisions of choosing restricted domains/periods/seasons to be the focus of the work. For instance, the CLLJ characterisation was carried out using the first version of the CFSR reanalysis that is available until 2010. It would be desirable to extend the analysis to the most recent decade. Even more, exploring the evolution of the CLLJ in a future warmer climate will be of scientific interest and societal relevance. It is also noticeable that the EEOF methodology could be applied to other atmospheric or oceanic fields for identifying lead/lag climate relationships in any region/season.

A limitation in the chapters using model simulations (3 and 4), is that the results are dependent on a single model. Therefore, a corroboration of the findings of this work in other climate models would be valuable. The focus of Chapter 3 was on sulphate aerosols only, as this is the most common species. However, including other aerosol species would be necessary if the interest is on quantifying the net effect of all aerosol types. Although of a larger size than in previous works, the use of 8-member ensembles did not allow us to conclusively assess the contribution from internal variability with enough confidence in Chapter 3. In this regard, the use of large-ensembles proves to be advantageous.

A shortcoming in using a global climate model of coarse horizontal resolution (2.5°) over the topographically-complex Mexico and the narrow Central American landmass was noted. This represented two main concerns. The first one is that the interactions between the low-level circulation and the topography loose accuracy due to the low spatial resolution. This could lead to some sub-synoptic processes to be underrepresented. The second one is that the low resolution did not allow to identify with some confidence the aerosol-induced simulated changes over Central

America in Chapter 3. However, please note that some of the limitations in Chapter 3 were overcome in Chapter 4. In particular, the use of the CESM large ensemble (with up to 40 members and 1° horizontal resolution) enabled us to quantify the role of internal variability with greater certainty and the higher spatial resolution allowed us to recognise more detailed spatial patterns in the HW's identification.

It should also be mentioned that the CESM-LENS is initialised from perturbed atmospheric states, but other climate components such as the ocean, the principal reservoir of memory in the climate system, the land and the cryosphere are initialised from the same conditions, thus the CESM-LENS internal climate variability arises only from the atmospheric perturbations. This could be an important issue if the simulations are intended to be used for decadal climate predictions, in which case the CESM-DPLE (Yeager et al. 2018) would be a more appropriate tool.

Regarding Chapter 4, the heat wave analysis could be extended to include other types of climate extremes, such as the climate indices defined by the Expert Team on Climate Change and Detection Indices (ETCCDI). This would further allow to make a broader statement about the recent changes on extreme climate events in the region. Finally, the mechanistic findings found here could help to analyse the performance of climate models from the Coupled Model Intercomparison Project Phase 6 (CMIP6) in the region. Furthermore, the influence from anthropogenic forcing (mainly of GHGs) is expected to continue to increase globally throughout the 21^{st} century. Thus, extending the analyses carried out in this thesis to the near and end-of-the-century future under different emission scenarios in the CMIP6 project would be useful for identifying and better preparing for the range of possible changes in climate.

References

Albrecht, B. A. Aerosols, cloud microphysics, and fractional cloudiness. *Science*, 245(4923):1227–1230, 1989. URL https://doi.org/10.1126/science.245.4923.1227.

Alexander, L. V., Zhang, X., Peterson, T. C., Caesar, J., Gleason, B., Klein Tank, A., Haylock, M., Collins, D., Trewin, B., Rahimzadeh, F., et al. Global observed changes in daily climate extremes of temperature and precipitation. *J. Geophys. Res. Atmos.*, 111(D5), 2006. URL https://doi.org/10.1029/2005JD006290.

Alfaro, E. J., Chourio, X., Muñoz, Á. G., and Mason, S. J. Improved seasonal prediction skill of rainfall for the Primera season in Central America. *Int. J. Climatol.*, 38:e255–e268, 2018. URL https://doi.org/10.1002/joc.5366.

Allen, M., Babiker, M., Chen, Y., de Coninck, H., Connors, S., van Diemen, R., and Zickfeld, K. Ipcc, 2018: summary for policymakers. In *Global warming of 1.5°C an IPCC special report on the impacts of global warming of 1.5°C above pre-industrial levels and related global greenhouse gas emission pathways, in the context of strengthening the global response to the threat of climate change, sustainable development, and efforts to eradicate poverty. Geneva.* 2018. URL https://www.ipcc.ch/2018/10/08/.

Allen, R. J., Evan, A. T., and Booth, B. B. Interhemispheric aerosol radiative forcing and tropical precipitation shifts during the late twentieth century. *J. Clim.*,

28(20):8219–8246, 2015. URL https://doi.org/10.1175/jcli-d-15-0148.1.

Amador, J. A. A climatic feature of the tropical Americas: The trade wind easterly jet. *Top. Meteor. Oceanogr.*, 5(2):1–13, 1998. URL http://www.kerwa.ucr.ac.cr/handle/10669/76623.

Amador, J. A. The intra-Americas sea low-level jet. *Ann. N. Y. Acad. Sci.*, 1146 (1):153–188, 2008. URL https://doi.org/10.1196/annals.1446.012.

Amador, J. A., Chacón, R. E., and Laporte, S. Climate and climate variability in the Arenal river basin of Costa Rica. In *Climate and Water*, pages 317–349. Springer, 2003. URL https://doi.org/10.1007/978-94-015-1250-3_14.

Amador, J. A., Alfaro, E. J., Lizano, O. G., and Magaña, V. O. Atmospheric forcing of the eastern tropical Pacific: A review. *Prog. Oceanogr.*, 69(2):101–142, 2006. URL https://doi.org/10.1016/j.pocean.2006.03.007.

Amador, J. A., Alfaro, E. J., Rivera, E. R., and Calderón, B. Climatic features and their relationship with tropical cyclones over the intra-Americas seas. In *Hurricanes and climate change*, pages 149–173. Springer, 2010. URL https://doi.org/10.1007/978-90-481-9510-7_9.

Amador, J. A., Durán-Quesada, A., Rivera, E., Mora, G., Sáenz, F., Calderón, B., and Mora, N. The easternmost tropical Pacific. Part II: Seasonal and intraseasonal modes of atmospheric variability. *Rev. Biol. Trop.*, 64(Supplement 1):S23–S57, 2016. URL https://doi.org/10.15517/rbt.v64i1.23409.

Andrade, C. A. and Barton, E. D. The Guajira upwelling system. *Cont. Shelf Res.*, 25(9):1003–1022, 2005. URL https://doi.org/10.1016/j.csr.2004.12.012.

Andrade, C. A. and Barton, E. D. Sobre la existencia de una celda de circulación atmosférica sobre el Caribe y su efecto en las corrientes de Ekman

del Caribe suroccidental. *Boletín Científico CIOH*, (31):73–94, 2013. URL https://doi.org/10.26640/01200542.31.2013.

Angeles, M. E., Gonzalez, J. E., Erickson, D. J., and Hernández, J. L. Predictions of future climate change in the Caribbean region using global general circulation models. *Int. J. Climatol.*, 27(5):555–569, 2007. URL https://doi.org/10.1002/joc.1416.

Argüeso, D., Di Luca, A., Perkins-Kirkpatrick, S. E., and Evans, J. P. Seasonal mean temperature changes control future heat waves. *Geophys. Res. Lett.*, 43 (14):7653–7660, 2016. URL https://doi.org/10.1002/2016gl069408.

Banerjee, A., Polvani, L., and Fyfe, J. The United States warming hole: Quantifying the forced aerosol response given large internal variability. *Geophys. Res. Lett.*, 44(4):1928–1937, 2017. URL https://doi.org/10.1002/2016gl071567.

Barlow, M. and Salstein, D. Summertime influence of the Madden-Julian Oscillation on daily rainfall over Mexico and Central America. *Geophys. Res. Lett.*, 33(21), 2006. URL https://doi.org/10.1029/2006gl027738.

Basu, R. and Ostro, B. D. A multicounty analysis identifying the populations vulnerable to mortality associated with high ambient temperature in California. *Am. J. Epidemiol.*, 168(6):632–637, 2008. URL https://doi.org/10.1093/aje/kwn170.

Baxter, S. and Nigam, S. Key role of the North Pacific Oscillation–west Pacific pattern in generating the extreme 2013/14 North American winter. *J. Clim.*, 28 (20):8109–8117, 2015. URL https://doi.org/10.1175/jcli-d-14-00726.1.

Becker, A., Finger, P., Meyer-Christoffer, A., Rudolf, B., Schamm, K., Schneider, U., and Ziese, M. A description of the global land-surface precipitation data products of the Global Precipitation Climatology Centre with sample applications including centennial (trend) analysis from 1901–present. *Earth Syst. Sci. Data*, 5(1):71–99, 2013. URL https://doi.org/10.5194/essd-5-71-2013.

Bindoff, N. L., Stott, P. A., AchutaRao, K. M., Allen, M. R., Gillett, N., Gutzler, D., Hansingo, K., Hegerl, G., Hu, Y., Jain, S., et al. Detection and attribution of climate change: from global to regional. 2013. URL https://doi.org/10.1017/cbo9781107415324.022.

Bollasina, M. A. and Messori, G. On the link between the subseasonal evolution of the North Atlantic Oscillation and East Asian climate. *Clim. Dyn.*, pages 1–21, 2018. URL https://doi.org/10.1007/s00382-018-4095-5.

Bollasina, M. A., Ming, Y., and Ramaswamy, V. Anthropogenic aerosols and the weakening of the South Asian summer monsoon. *Science*, 334(6055):502–505, 2011. URL https://doi.org/10.1126/science.1204994.

Bollasina, M. A., Ming, Y., Ramaswamy, V., Schwarzkopf, M. D., and Naik, V. Contribution of local and remote anthropogenic aerosols to the twentieth century weakening of the South Asian Monsoon. *Geophys. Res. Lett.*, 41(2): 680–687, 2014. URL https://doi.org/10.1002/2013gl058183.

Booth, B. B., Dunstone, N. J., Halloran, P. R., Andrews, T., and Bellouin, N. Aerosols implicated as a prime driver of twentieth-century North Atlantic climate variability. *Nature*, 484(7393):228–232, 2012. URL https://doi.org/10.1038/nature11138.

Boucher, O., Randall, D., Artaxo, P., Bretherton, C., Feingold, G., Forster, P., Kerminen, V.-M., Kondo, Y., Liao, H., Lohmann, U., et al. Clouds and aerosols. In *Climate change 2013: the physical science basis. Contribution of Working Group I to the Fifth Assessment Report of the Intergovernmental Panel on Climate Change*, pages 571–657. Cambridge University Press, 2013. URL https://www.ipcc.ch/report/ar5/wg1/.

Burgman, R. J. and Jang, Y. Simulated US drought response to interannual and decadal Pacific SST variability. *J. Clim.*, 28(12):4688–4705, 2015. URL https://doi.org/10.1175/JCLI-D-14-00247.1.

Campbell, J. D., Taylor, M. A., Stephenson, T. S., Watson, R. A., and Whyte, F. S. Future climate of the Caribbean from a regional climate model. *Int. J. Climatol.*, 31(12):1866–1878, 2011. URL https://doi.org/10.1002/joc.2200.

Charlson, R. J., Schwartz, S., Hales, J., Cess, R. D., Coakley, J. J., Hansen, J., and Hofmann, D. Climate forcing by anthropogenic aerosols. *Science*, 255(5043): 423–430, 1992. URL https://doi.org/10.1126/science.255.5043.423.

Chen, J.-M. and Harr, P. A. Interpretation of extended empirical orthogonal function (eeof) analysis. *Monthly weather review*, 121(9):2631–2636, 1993. URL https://doi.org/10.1175/1520-0493(1993)121<2631:IOEEOF>2.0.CO;2.

Chen, Y. and Li, Y. An inter-comparison of three heat wave types in china during 1961–2010: Observed basic features and linear trends. *Sci. Rep.*, 7(1): 1–10, 2017. URL https://doi.org/10.1038/srep45619.

Cook, K. H. and Vizy, E. K. Hydrodynamics of the Caribbean low-level jet and its relationship to precipitation. *J. Clim.*, 23(6):1477–1494, 2010. URL https://doi.org/10.1175/2009jcli3210.1.

CRU, Harris, I. C., and Jones, P. D. CRU TS4.01: Climatic Research Unit (CRU) Time-Series (TS) version 4.01 of high-resolution gridded data of month-by-month variation in climate (jan. 1901- dec. 2016), 2017. URL https://catalogue.ceda.ac.uk/uuid/58a8802721c94c66ae45c3baa4d814d0.

CRU, Jones, P. D., and Harris, I. C. Climatic Research Unit: Time-series datasets of variations in climate with variations in other phenomena v3.0-v3.26, 2019. URL https://catalogue.ceda.ac.uk/uuid/3f8944800cc48e1cbc29a5ee12d8542d.

Cueto, R. O. G., Martínez, A. T., and Ostos, E. J. Heat waves and heat days in an arid city in the northwest of Mexico: current trends and in

climate change scenarios. *Int. J. Biometeorol.*, 54(4):335–345, 2010. URL https://doi.org/10.1007/s00484-009-0283-7.

Dee, D. P., Uppala, S. M., Simmons, A., Berrisford, P., Poli, P., Kobayashi, S., Andrae, U., Balmaseda, M., Balsamo, G., Bauer, d. P., et al. The ERA-Interim reanalysis: Configuration and performance of the data assimilation system. *Q. J. R. Meteorol. Soc.*, 137(656):553–597, 2011. URL https://doi.org/10.1002/qj.828.

Della-Marta, P. M., Haylock, M. R., Luterbacher, J., and Wanner, H. Doubled length of western European summer heat waves since 1880. *J. Geophys. Res. Atmos.*, 112(D15), 2007. URL https://doi.org/10.1029/2007JD008510.

Deser, C., Phillips, A. S., Alexander, M. A., and Smoliak, B. V. Projecting North American climate over the next 50 years: Uncertainty due to internal variability. *J. Clim.*, 27(6):2271–2296, 2014. URL https://doi.org/10.1175/JCLI-D-13-00451.1.

Ding, Q. and Wang, B. Circumglobal teleconnection in the Northern Hemisphere summer. *J. Clim.*, 18(17):3483–3505, 2005. URL https://doi.org/10.1175/JCLI3473.1.

Donat, M., Alexander, L., Yang, H., Durre, I., Vose, R., Dunn, R., Willett, K., Aguilar, E., Brunet, M., Caesar, J., et al. Updated analyses of temperature and precipitation extreme indices since the beginning of the twentieth century: The HadEX2 dataset. *J. Geophys. Res. Atmos.*, 118(5):2098–2118, 2013. URL https://doi.org/10.1002/jgrd.50150.

Durán-Quesada, A., Gimeno, L., Amador, J., and Nieto, R. A Lagrangian approach to moisture sources for Central America: Part I. Moisture sources identification. *J. Geophys. Res.*, 15, 2010. URL https://doi.org/10.1029/2010JD014168.

Endfield, G. H., Fern, I., et al. Decades of drought, years of hunger: archival investigations of multiple year droughts in late colonial Chihuahua. *Clim. Change*, 75(4):391, 2006. URL https://doi.org/10.1007/s10584-006-3492-7.

Enfield, D. B. and Alfaro, E. J. The dependence of Caribbean rainfall on the interaction of the tropical Atlantic and Pacific Oceans. *J. Clim.*, 12(7):2093–2103, 1999. URL https://doi.org/10.1175/1520-0442(1999)012<2093:tdocro>2.0.co;2.

Fiedler, P. C. The annual cycle and biological effects of the costa rica dome. *Deep Sea Res. Part I Oceanogr. Res. Pap.*, 49(2):321–338, 2002. URL https://doi.org/10.1016/S0967-0637(01)00057-7.

Findell, K. L., Berg, A., Gentine, P., Krasting, J. P., Lintner, B. R., Malyshev, S., Santanello, J. A., and Shevliakova, E. The impact of anthropogenic land use and land cover change on regional climate extremes. *Nature communications*, 8(1):1–10, 2017. URL https://doi.org/10.1038/s41467-017-01038-w.

Fuentes-Franco, R., Coppola, E., Giorgi, F., Pavia, E. G., Diro, G. T., and Graef, F. Inter-annual variability of precipitation over southern Mexico and Central America and its relationship to sea surface temperature from a set of future projections from CMIP5 GCMs and RegCM4 CORDEX simulations. *Clim. Dyn.*, 45(1-2):425–440, 2015. URL https://doi.org/10.1007/s00382-014-2258-6.

Funk, C., Peterson, P., Landsfeld, M., Pedreros, D., Verdin, J., Shukla, S., Husak, G., Rowland, J., Harrison, L., Hoell, A., et al. The climate hazards infrared precipitation with stations–a new environmental record for monitoring extremes. *Sci. Data*, 2:150066, 2015. URL https://doi.org/10.1038/sdata.2015.66.

García-Herrera, R., Díaz, J., Trigo, R. M., Luterbacher, J., and Fischer, E. M. A review of the European summer heat wave of 2003. *Crit. Rev. Envi-*

ron. Sci. Technol., 40(4):267–306, 2010. URL https://doi.org/10.1080/10643380802238137.

Ghan, S. J., Liu, X., Easter, R. C., Zaveri, R., Rasch, P. J., Yoon, J.-H., and Eaton, B. Toward a minimal representation of aerosols in climate models: Comparative decomposition of aerosol direct, semidirect, and indirect radiative forcing. *J. Clim.*, 25(19):6461–6476, 2012. URL https://doi.org/10.1175/jcli-d-11-00650.1.

Gillett, N. P., Shiogama, H., Funke, B., Hegerl, G., Knutti, R., Matthes, K., Santer, B. D., Stone, D., and Tebaldi, C. Detection and attribution model intercomparison project (DAMIP). *Geosci. Model Dev.*, 9(10):3685–3697, 2016. URL https://doi.org/10.5194/gmd-2016-74-rc2.

Gosling, S. N., Lowe, J. A., McGregor, G. R., Pelling, M., and Malamud, B. D. Associations between elevated atmospheric temperature and human mortality: a critical review of the literature. *Clim. Change*, 92(3-4):299–341, 2009. URL https://doi.org/10.1007/s10584-008-9441-x.

Gosling, S. N., Dunn, R., Carrol, F., Christidis, N., Fullwood, J., Gusmao, D. d., Golding, N., Good, L., Hall, T., Kendon, L., et al. Climate: Observations, projections and impacts, 2011. URL https://nottingham-repository.worktribe.com/output/1010959/climate-observations-projections-and-impacts.

Hall, T. C., Sealy, A. M., Stephenson, T. S., Kusunoki, S., Taylor, M. A., Chen, A. A., and Kitoh, A. Future climate of the Caribbean from a super-high-resolution atmospheric general circulation model. *Theor. Appl. Climatol.*, 113 (1-2):271–287, 2013. URL https://doi.org/10.1007/s00704-012-0779-7.

Hansen, J., Ruedy, R., Sato, M., and Lo, K. Global surface temperature change. *Rev. Geophys.*, 48(4), 2010. URL https://doi.org/10.1029/2010RG000345.

Hastenrath, S. L. Rainfall distribution and regime in Central America. *Arch. Meteor. Geophys. Bioklimatol., Serie B*, 15(3):201–241, 1967. URL https://doi.org/10.1007/bf02243853.

Herrera, E., Magaña, V., and Caetano, E. Air–sea interactions and dynamical processes associated with the midsummer drought. *Int. J. Climatol.*, 35(7): 1569–1578, 2015. URL https://doi.org/10.1002/joc.4077.

Hidalgo, H. G., Durán-Quesada, A. M., Amador, J. A., and Alfaro, E. J. The Caribbean low-level jet, the inter-tropical convergence zone and precipitation patterns in the intra-Americas sea: A proposed dynamical mechanism. *Geogr. Ann. Ser. A, Physical Geograph.y*, 97(1):41–59, 2015. URL https://doi.org/10.1111/geoa.12085.

Higgins, R. W., Janowiak, J. E., and Yao, Y.-P. *A gridded hourly precipitation data base for the United States (1963-1993)*. US Department of Commerce, National Oceanic and Atmospheric Administration, 1996. URL https://doi.org/10.5065/P6BM-VM62.

Hoesly, R. M., Smith, S. J., Feng, L., Klimont, Z., Janssens-Maenhout, G., Pitkanen, T., Seibert, J. J., Vu, L., Andres, R. J., Bolt, R. M., et al. Historical (1750–2014) anthropogenic emissions of reactive gases and aerosols from the Community Emissions Data System (CEDS). *Geosci. Model Dev.*, 11(PNNL-SA-123932), 2018. URL https://doi.org/10.5194/gmd-11-369-2018.

Huffman, G. J., Bolvin, D. T., Nelkin, E. J., Wolff, D. B., Adler, R. F., Gu, G., Hong, Y., Bowman, K. P., and Stocker, E. F. The TRMM multisatellite precipitation analysis (TMPA): Quasi-global, multiyear, combined-sensor precipitation estimates at fine scales. *J. Hydrometeorol.*, 8(1):38–55, 2007. URL https://doi.org/10.1175/JHM560.1.

Hurrell, J. W., Holland, M. M., Gent, P. R., Ghan, S., Kay, J. E., Kushner, P. J., Lamarque, J.-F., Large, W. G., Lawrence, D., Lindsay, K., et al. The

Community Earth System Model: a framework for collaborative research. *Bull. Amer. Meteor. Soc.*, 94(9):1339–1360, 2013. URL https://doi.org/10.1175/BAMS-D-12-00121.1.

Inoue, M., Handoh, I. C., and Bigg, G. R. Bimodal distribution of tropical cyclogenesis in the Caribbean: Characteristics and environmental factors. *J. Clim.*, 15(20):2897–2905, 2002. URL https://doi.org/10.1175/1520-0442(2002)015<2897:bdotci>2.0.co;2.

Jouanno, J. and Sheinbaum, J. Heat balance and eddies in the Caribbean upwelling system. *J. Phys. Oceanogr.*, 43(5):1004–1014, 2013. URL https://doi.org/10.1175/jpo-d-12-0140.1.

Kalnay, E., Kanamitsu, M., Kistler, R., Collins, W., Deaven, D., Gandin, L., Iredell, M., Saha, S., White, G., Woollen, J., et al. The NCEP/NCAR 40-year reanalysis project. *Bull. Amer. Meteor. Soc.*, 77(3):437–472, 1996. URL https://doi.org/10.1175/1520-0477(1996)077<0437:TNYRP>2.0.CO;2.

Karmalkar, A. V., Bradley, R. S., and Diaz, H. F. Climate change in Central America and Mexico: regional climate model validation and climate change projections. *Clim. Dyn.*, 37(3-4):605, 2011. URL https://doi.org/10.1007/s00382-011-1099-9.

Kay, J. E., Deser, C., Phillips, A., Mai, A., Hannay, C., Strand, G., Arblaster, J. M., Bates, S., Danabasoglu, G., Edwards, J., et al. The Community Earth System Model (CESM) large ensemble project: A community resource for studying climate change in the presence of internal climate variability. *Bull. Amer. Meteor. Soc.*, 96(8):1333–1349, 2015. URL https://doi.org/10.1175/BAMS-D-13-00255.1.

Kucharski, F., Bracco, A., Yoo, J., Tompkins, A., Feudale, L., Ruti, P., and Dell'Aquila, A. A Gill–Matsuno-type mechanism explains the tropical Atlantic

influence on African and Indian monsoon rainfall. *Q. J. Royal Meteorol. Soc.*, 135(640):569–579, 2009. URL https://doi.org/10.1002/qj.406.

Kunkel, K. E., Pielke Jr, R. A., and Changnon, S. A. Temporal fluctuations in weather and climate extremes that cause economic and human health impacts: A review. *Bull. Am. Meteorol. Soc.*, 80(6):1077–1098, 1999. URL https://doi.org/10.1175/1520-0477(1999)080<1077:tfiwac>2.0.co;2.

Kunkel, K. E., Liang, X.-Z., Zhu, J., and Lin, Y. Can CGCMs simulate the twentieth-century warming hole in the central United States? *J. Clim.*, 19(17): 4137–4153, 2006. URL https://doi.org/10.1175/jcli3848.1.

Kushnir, Y., Seager, R., Ting, M., Naik, N., and Nakamura, J. Mechanisms of tropical Atlantic SST influence on North American precipitation variability. *J. Clim.*, 23(21):5610–5628, 2010. URL https://doi.org/10.1175/2010JCLI3172.1.

Lamarque, J.-F., Bond, T. C., Eyring, V., Granier, C., Heil, A., Klimont, Z., Lee, D., Liousse, C., Mieville, A., Owen, B., et al. Historical (1850–2000) gridded anthropogenic and biomass burning emissions of reactive gases and aerosols: methodology and application. *Atmos. Chem. Phys.*, 10(15):7017–7039, 2010. URL https://doi.org/10.5194/acp-10-7017-2010.

Lau, N.-C. and Nath, M. J. A model study of heat waves over North America: Meteorological aspects and projections for the twenty-first century. *J. Clim.*, 25 (14):4761–4784, 2012. URL https://doi.org/10.1175/jcli-d-11-00575.1.

Lee, S. K., Enfield, D., and Wang, C. What drives the seasonal onset and decay of the Western Hemisphere Warm Pool? *J. Clim.*, 20(10):2133–2146, 2007. URL https://doi.org/10.1175/jcli4113.1.

Leibensperger, E., Mickley, L. J., Jacob, D. J., Chen, W.-T., Seinfeld, J., Nenes, A., Adams, P., Streets, D., Kumar, N., and Rind, D. Climatic effects of

1950–2050 changes in US anthropogenic aerosols–Part 2: Climate response. *Atmos. Chem. Phys.*, 12(7):3349–3362, 2012. URL https://doi.org/10.5194/acpd-11-24127-2011.

Lorenz, C. and Kunstmann, H. The hydrological cycle in three state-of-the-art reanalyses: Intercomparison and performance analysis. *J. Hydrometeorol.*, 13 (5):1397–1420, 2012. URL https://doi.org/10.1175/jhm-d-11-088.1.

Luber, G. and McGeehin, M. Climate change and extreme heat events. *Am. J. Prev. Med.*, 35(5):429–435, 2008. URL https://doi.org/10.1016/j.amepre.2008.08.021.

Magaña, V. and Caetano, E. Temporal evolution of summer convective activity over the Americas warm pools. *Geophys. Res. Lett.*, 32(2), 2005. URL https://doi.org/10.1029/2004gl021033.

Magaña, V., Amador, J. A., and Medina, S. The midsummer drought over Mexico and Central America. *J. Clim.*, 12(6):1577–1588, 1999. URL https://doi.org/10.1175/1520-0442(1999)012<1577:tmdoma>2.0.co;2.

Maldonado, T., Rutgersson, A., Caballero, R., Pausata, F. S., Alfaro, E., and Amador, J. The role of the meridional sea surface temperature gradient in controlling the Caribbean low-level jet. *J. Geophys. Res. Atmos.*, 122(11): 5903–5916, 2017. URL https://doi.org/10.1002/2016jd026025.

Maldonado, T., Alfaro, E. J., and Hidalgo, H. G. Revision of the main drivers and variability of Central America Climate and seasonal forecast systems. *Rev. Biol. Trop.*, 66(1), 2018. URL https://doi.org/10.15517/rbt.v66i1.33294.

Maloney, E. D. and Hartmann, D. L. Modulation of hurricane activity in the Gulf of Mexico by the Madden-Julian oscillation. *Science*, 287(5460):2002–2004, 2000. URL https://doi.org/10.1126/science.287.5460.2002.

Martin, E. R. and Schumacher, C. Modulation of Caribbean precipitation by the Madden–Julian oscillation. *J. Clim.*, 24(3):813–824, 2011. URL https://doi.org/10.1175/2010jcli3773.1.

Martinez, C., Goddard, L., Kushnir, Y., and Ting, M. Seasonal climatology and dynamical mechanisms of rainfall in the Caribbean. *Clim. Dyn.*, pages 1–22, 2019. URL https://doi.org/10.1007/s00382-019-04616-4.

Martinez-Sanchez, J. N. and Cavazos, T. Eastern Tropical Pacific hurricane variability and landfalls on Mexican coasts. *Clim. Res.*, 58(3):221–234, 2014. URL https://doi.org/10.3354/cr01192.

Mascioli, N. R., Previdi, M., Fiore, A. M., and Ting, M. Timing and seasonality of the United States warming hole. *Environ. Res. Lett.*, 12(3):034008, 2017. URL https://doi.org/10.1088/1748-9326/aa5ef4.

Meehl, G. A., Arblaster, J. M., and Tebaldi, C. Contributions of natural and anthropogenic forcing to changes in temperature extremes over the United States. *Geophys. Res. Lett.*, 34(19), 2007. URL https://doi.org/10.1029/2007gl030948.

Meehl, G. A., Washington, W. M., Arblaster, J. M., Hu, A., Teng, H., Kay, J. E., Gettelman, A., Lawrence, D. M., Sanderson, B. M., and Strand, W. G. Climate change projections in CESM1 (CAM5) compared to CCSM4. *J. Clim.*, 26(17): 6287–6308, 2013. URL https://doi.org/10.1175/JCLI-D-12-00572.1.

Méndez, M. and Magaña, V. Regional aspects of prolonged meteorological droughts over Mexico and Central America. *J. Clim.*, 23(5):1175–1188, 2010. URL https://doi.org/10.1175/2009jcli3080.1.

Mestas-Nuñez, A. M., Enfield, D. B., and Zhang, C. Water vapor fluxes over the intra-Americas Sea: Seasonal and interannual variability and associations with rainfall. *J. Clim.*, 20(9):1910–1922, 2007. URL https://doi.org/10.1175/jcli4096.1.

Ming, Y. and Ramaswamy, V. Nonlinear climate and hydrological responses to aerosol effects. *J. Clim.*, 22(6):1329–1339, 2009. URL https://doi.org/10.1175/2008jcli2362.1.

Mo, K. C., Chelliah, M., Carrera, M. L., Higgins, R. W., and Ebisuzaki, W. Atmospheric moisture transport over the United States and Mexico as evaluated in the NCEP regional reanalysis. *J. Hydrometeorol.*, 6(5):710–728, 2005. URL https://doi.org/10.1175/JHM452.1.

Muñoz, E. and Enfield, D. The boreal spring variability of the intra-Americas low-level jet and its relation with precipitation and tornadoes in the eastern United States. *Clim. Dyn.*, 36(1-2):247–259, 2011. URL https://doi.org/10.1007/s00382-009-0688-3.

Muñoz, E., Busalacchi, A. J., Nigam, S., and Ruiz-Barradas, A. Winter and summer structure of the Caribbean low-level jet. *J. Clim.*, 21(6):1260–1276, 2008. URL https://doi.org/10.1175/2007jcli1855.1.

Myhre, G., Shindell, D., and Pongratz, J. Anthropogenic and natural radiative forcing. 2014. URL https://doi.org/10.1017/cbo9781107415324.019.

Neale, R. B., Gettelman, A., Park, S., Chen, C.-C., Lauritzen, P. H., Williamson, D. L., et al. Description of the NCAR community atmosphere model (CAM 5.0). *NCAR Technical note*, 2012. URL https://doi.org/10.5065/D6N877R0.

Neri, C. and Magaña, V. Estimation of vulnerability and risk to meteorological drought in Mexico. *Weather Clim. Soc.*, 8(2):95–110, 2016. URL https://doi.org/10.1175/wcas-d-15-0005.1.

Nigam, S. and Ruiz-Barradas, A. Seasonal hydroclimate variability over North America in global and regional reanalyses and AMIP simulations: Varied representation. *J. Clim.*, 19(5):815–837, 2006. URL https://doi.org/10.1175/JCLI3635.1.

North, G. R., Bell, T. L., Cahalan, R. F., and Moeng, F. J. Sampling errors in the estimation of empirical orthogonal functions. *Mon. Weather Rev.*, 110(7): 699–706, 1982. URL https://doi.org/10.1175/1520-0493(1982)110<0699:seiteo>2.0.co;2.

Pachauri, R. K., Allen, M. R., Barros, V. R., Broome, J., Cramer, W., Christ, R., Church, J. A., Clarke, L., Dahe, Q., Dasgupta, P., and et al. *Climate change 2014: synthesis report. Contribution of Working Groups I, II and III to the fifth assessment report of the Intergovernmental Panel on Climate Change*. IPCC, 2014. URL https://www.ipcc.ch/report/ar5/syr/.

Perdigón-Morales, J., Romero-Centeno, R., Ordoñez, P., Nieto, R., Gimeno, L., and Barrett, B. S. Influence of the Madden-Julian Oscillation on moisture transport by the Caribbean Low Level Jet during the Midsummer Drought in Mexico. *Atmos. Res.*, 248:105243, 2020. URL https://doi.org/10.1016/j.atmosres.2020.105243.

Persad, G. G. and Caldeira, K. Divergent global-scale temperature effects from identical aerosols emitted in different regions. *Nat. Commun.*, 9(1):1–9, 2018. URL https://doi.org/10.1038/s41467-018-05838-6.

Polson, D., Bollasina, M., Hegerl, G. C., and Wilcox, L. Decreased monsoon precipitation in the Northern Hemisphere due to anthropogenic aerosols. *Geophys. Res. Lett.*, 41(16):6023–6029, 2014. URL https://doi.org/10.1002/2014gl060811.

Portmann, R. W., Solomon, S., and Hegerl, G. C. Spatial and seasonal patterns in climate change, temperatures, and precipitation across the United States. *Proc. Natl. Acad. Sci.*, 106(18):7324–7329, 2009. URL https://doi.org/10.1073/pnas.0808533106.

Qin, J. and Robinson, W. A. On the Rossby wave source and the steady linear

response to tropical forcing. *J. Atmos. Sci.*, 50(12):1819–1823, 1993. URL https://doi.org/10.1175/1520-0469(1993)050<1819:OTRWSA>2.0.CO;2.

Ridley, H. E., Asmerom, Y., Baldini, J. U., Breitenbach, S. F., Aquino, V. V., Prufer, K. M., Culleton, B. J., Polyak, V., Lechleitner, F. A., Kennett, D. J., et al. Aerosol forcing of the position of the intertropical convergence zone since AD 1550. *Nat. Geosci.*, 8(3):195, 2015. URL https://doi.org/10.1038/ngeo2353.

Robine, J.-M., Cheung, S. L. K., Le Roy, S., Van Oyen, H., Griffiths, C., Michel, J.-P., and Herrmann, F. R. Death toll exceeded 70,000 in Europe during the summer of 2003. *C. R. Biol.*, 331(2):171–178, 2008. URL https://doi.org/10.1016/j.crvi.2007.12.001.

Robinson, W. A., Reudy, R., and Hansen, J. E. General circulation model simulations of recent cooling in the east-central United States. *J. Geophys. Res. Atmos.*, 107(D24):ACL–4, 2002. URL https://doi.org/10.1029/2001jd001577.

Rodwell, M. J. and Hoskins, B. J. Subtropical anticyclones and summer monsoons. *J. Clim.*, 14(15):3192–3211, 2001. URL https://doi.org/10.1175/1520-0442(2001)014<3192:SAASM>2.0.CO;2.

Rohde, R., Muller, R., Jacobsen, R., Muller, E., Perlmutter, S., Rosenfeld, A., Wurtele, J., Groom, D., and Wickham, C. A new estimate of the average Earth surface land temperature spanning 1753 to 2011. *Geoinfor. Geostat.: An Overview*, 7:2, 2013. URL https://doi.org/10.4172/2327-4581.1000101.

Romero-Centeno, R., Zavala-Hidalgo, J., Gallegos, A., and O'Brien, J. J. Isthmus of Tehuantepec wind climatology and ENSO signal. *J. Clim.*, 16(15):2628–2639, 2003. URL https://doi.org/10.1175/1520-0442(2003)016<2628:iotwca>2.0.co;2.

Romero-Centeno, R., Zavala-Hidalgo, J., and Raga, G. Midsummer gap winds and low-level circulation over the eastern tropical Pacific. *J. Clim.*, 20(15): 3768–3784, 2007. URL https://doi.org/10.1175/jcli4220.1.

Ross, T. and Lott, N. A climatology of 1980-2003 extreme weather and climate events. 2003. URL https://repository.library.noaa.gov/view/noaa/13831.

Ruiz-Barradas, A. and Nigam, S. IPCCs twentieth-century climate simulations: Varied representations of North American hydroclimate variability. *J. Clim.*, 19(16):4041–4058, 2006. URL https://doi.org/10.1175/JCLI3809.1.

Saha, S., Moorthi, S., Pan, H.-L., Wu, X., Wang, J., Nadiga, S., Tripp, P., Kistler, R., Woollen, J., Behringer, D., et al. The NCEP climate forecast system reanalysis. *Bull. Am. Meteorol. Soc.*, 91(8):1015–1058, 2010. URL https://doi.org/10.1175/2010BAMS3001.1.

Santer, B. D., Wigley, T., Boyle, J., Gaffen, D. J., Hnilo, J., Nychka, D., Parker, D., and Taylor, K. Statistical significance of trends and trend differences in layer-average atmospheric temperature time series. *J. Geophys. Res. Atmos.*, 105(D6):7337–7356, 2000. URL https://doi.org/10.1029/1999jd901105.

Sardeshmukh, P. D. and Hoskins, B. J. The generation of global rotational flow by steady idealized tropical divergence. *J. Atmos. Sci.*, 45(7):1228–1251, 1988. URL https://doi.org/10.1175/1520-0469(1988)045<1228:TGOGRF>2.0.CO;2.

Serra, Y. L., Kiladis, G. N., and Hodges, K. I. Tracking and mean structure of easterly waves over the intra-Americas Sea. *J. Clim.*, 23(18):4823–4840, 2010. URL https://doi.org/10.1175/2010jcli3223.1.

Serra, Y. L., Jiang, X., Tian, B., Amador-Astua, J., Maloney, E. D., and Kiladis, G. N. Tropical intraseasonal modes of the atmosphere. *Annu.*

Rev. Environ. Resour., 39:189–215, 2014. URL https://doi.org/10.1146/annurev-environ-020413-134219.

Singh, B. Climate changes in the greater and southern Caribbean. *Int. J. Climatol.*, 17(10):1093–1114, 1997. URL https://doi.org/10.1002/(sici)1097-0088(199708)17:10<1093::aid-joc187>3.0.co;2-l.

Small, R. J. O., De Szoeke, S. P., and Xie, S.-P. The Central American midsummer drought: regional aspects and large-scale forcing. *J. Clim.*, 20(19):4853–4873, 2007. URL https://doi.org/10.1175/jcli4261.1.

Smith, S. J., van Aardenne, J., Klimont, Z., Andres, R. J., Volke, A., and Delgado Arias, S. Anthropogenic sulfur dioxide emissions: 1850-2005. *Atmos. Chem. Phys.*, 11(3):1101–1116, 2011. URL https://doi.org/10.5194/acp-11-1101-2011.

Song, F., Zhou, T., and Qian, Y. Responses of East Asian summer monsoon to natural and anthropogenic forcings in the 17 latest CMIP5 models. *Geophys. Res. Lett.*, 41(2):596–603, 2014. URL https://doi.org/10.1002/2013gl058705.

Stahle, D. W., Cook, E. R., Diaz, J. V., Fye, F. K., Burnette, D. J., Griffin, D., Soto, R. A., Seager, R., and Heim Jr, R. R. Early 21st-century drought in Mexico. *Eos Trans. AGU*, 90(11):89–90, 2009. URL https://doi.org/10.1029/2009eo110001.

Stevens, B. and Feingold, G. Untangling aerosol effects on clouds and precipitation in a buffered system. *Nature*, 461(7264):607–613, 2009. URL https://doi.org/10.1038/nature08281.

Stocker, T. F., Qin, D., Plattner, G.-K., Tignor, M., Allen, S. K., Boschung, J., Nauels, A., Xia, Y., Bex, V., Midgley, P. M., et al. Climate change 2013: The physical science basis, 2013. URL https://www.ipcc.ch/report/ar5/wg1/.

Su, Q. and Dong, B. Projected near-term changes in three types of heat waves over China under RCP4.5. *Clim. Dyn.*, 53(7-8):3751–3769, 2019a. URL https://doi.org/10.1007/s00382-019-04743-y.

Su, Q. and Dong, B. Recent decadal changes in heat waves over china: drivers and mechanisms. *J. Clim.*, 32(14):4215–4234, 2019b. URL https://doi.org/10.1175/JCLI-D-18-0479.1.

Sun, Q., Miao, C., Duan, Q., Ashouri, H., Sorooshian, S., and Hsu, K.-L. A review of global precipitation data sets: Data sources, estimation, and intercomparisons. *Rev Geophys*, 56(1):79–107, 2018. URL https://doi.org/10.1002/2017rg000574.

Taylor, M. A. and Alfaro, E. J. Central America and the Caribbean, climate of. In *Encyclopedia of world climatology*, pages 183–189. Springer, 2005. URL https://doi.org/10.1007/1-4020-3266-8_37.

Taylor, M. A., Stephenson, T. S., Chen, A. A., and Stephenson, K. A. Climate change and the Caribbean: review and response. *Caribb. Stud.*, pages 169–200, 2012. URL https://doi.org/10.1353/crb.2012.0020.

Taylor, M. A., Whyte, F. S., Stephenson, T. S., and Campbell, J. D. Why dry? investigating the future evolution of the Caribbean low level jet to explain projected Caribbean drying. *Int. J. Climatol.*, 33(3):784–792, 2013. URL https://doi.org/10.1002/joc.3461.

Thompson, D. W., Barnes, E. A., Deser, C., Foust, W. E., and Phillips, A. S. Quantifying the role of internal climate variability in future climate trends. *J. Clim.*, 28(16):6443–6456, 2015. URL https://doi.org/10.1175/JCLI-D-14-00830.1.

Ting, M. Maintenance of northern summer stationary waves in a GCM. *J. Atmos. Sci.*, 51(22):3286–3308, 1994. URL https://doi.org/10.1175/1520-0469(1994)051<3286:monssw>2.0.co;2.

Twomey, S. The influence of pollution on the shortwave albedo of clouds. *J. Atmos. Sci.*, 34(7):1149–1152, 1977. URL https://doi.org/10.1175/1520-0469(1977)034<1149:tiopot>2.0.co;2.

Undorf, S., Bollasina, M., Booth, B., and Hegerl, G. Contrasting the effects of the 1850–1975 increase in sulphate aerosols from North America and Europe on the Atlantic in the CESM. *Geophys. Res. Lett.*, 45(21):11–930, 2018a. URL https://doi.org/10.1029/2018GL079970.

Undorf, S., Polson, D., Bollasina, M., Ming, Y., Schurer, A., and Hegerl, G. Detectable impact of local and remote anthropogenic aerosols on the 20th century changes of West African and South Asian monsoon precipitation. *J. Geophys. Res. Atmos.*, 123(10):4871–4889, 2018b. URL https://doi.org/10.1029/2017jd027711.

Undorf, S. Isolating the impact of North American and European anthropogenic aerosol emissions since the early instrumental period. *The University of Edinburgh*, 2019. URL https://era.ed.ac.uk/handle/1842/35588.

United Nations. World Population Prospects 2019, vol. 1, comprehensive tables. http://esa.un.org/unpd/wpp/index.htm, 2019. Accessed: 2019-11-29.

Vega-Camarena, J. P., Brito-Castillo, L., Farfán, L. M., Gochis, D. J., Pineda-Martínez, L. F., and Díaz, S. C. Ocean–atmosphere conditions related to severe and persistent droughts in the Mexican Altiplano. *Int. J. Climatol.*, 38(2):853–866, 2018. URL https://doi.org/10.1002/joc.5215.

Wang, C. Variability of the Caribbean low-level jet and its relations to climate. *Clim. Dyn.*, 29(4):411–422, 2007. URL https://doi.org/10.1007/s00382-007-0243-z.

Wang, C. and Lee, S.-k. Atlantic warm pool, Caribbean low-level jet, and their potential impact on Atlantic hurricanes. *Geophys. Res. Lett.*, 34(2), 2007. URL https://doi.org/10.1029/2006gl028579.

Wang, H., Schubert, S., Suarez, M., Chen, J., Hoerling, M., Kumar, A., and Pegion, P. Attribution of the seasonality and regionality in climate trends over the United States during 1950–2000. *J. Clim.*, 22(10):2571–2590, 2009. URL https://doi.org/10.1175/2008jcli2359.1.

Wang, J., Chen, Y., Tett, S. F., Yan, Z., Zhai, P., Feng, J., and Xia, J. Anthropogenically-driven increases in the risks of summertime compound hot extremes. *Nat. Commun.*, 11(1):1–11, 2020. URL https://doi.org/10.1038/s41467-019-14233-8.

Weare, B. C. and Nasstrom, J. S. Examples of extended empirical orthogonal function analyses. *Mon. Weather Rev.*, 110(6):481–485, 1982. URL https://doi.org/10.1175/1520-0493(1982)110<0481:eoeeof>2.0.co;2.

Weaver, S. J. and Nigam, S. Variability of the Great Plains low-level jet: Large-scale circulation context and hydroclimate impacts. *J. Clim.*, 21(7):1532–1551, 2008. URL https://doi.org/10.1175/2007JCLI1586.1.

Weaver, S. J. and Nigam, S. Recurrent supersynoptic evolution of the Great Plains low-level jet. *J. Clim.*, 24(2):575–582, 2011. URL https://doi.org/10.1175/2010JCLI3445.1.

Westervelt, D., Horowitz, L., Naik, V., and Mauzerall, D. L. Radiative forcing and climate response to projected 21st century aerosol decreases. *Atmos. Chem. Phys. Discuss.*, 15(6), 2015. URL https://doi.org/10.5194/acp-15-12681-2015.

Westervelt, D., Conley, A., Fiore, A., Lamarque, J.-F., Shindell, D., Previdi, M., Faluvegi, G., Correa, G., and Horowitz, L. Multimodel precipitation responses to removal of US sulfur dioxide emissions. *J. Geophys. Res. Atmos.*, 122(9): 5024–5038, 2017. URL https://doi.org/10.1002/2017jd026756.

Westervelt, D., Conley, A., Fiore, A., Lamarque, J., Shindell, D., Previdi, M., Mascioli, N., Faluvegi, G., Correa, G., and Horowitz, L. Connecting regional

aerosol emissions reductions to local and remote precipitation responses. *Atmos. Chem. Phys.*, 18(16):12461–12475, 2018. URL https://doi.org/10.5194/acp-18-12461-2018.

Wheeler, M. C. and Hendon, H. H. An all-season real-time multivariate MJO index: Development of an index for monitoring and prediction. *Mon. Weather Rev.*, 132(8):1917–1932, 2004. URL https://doi.org/10.1175/1520-0493(2004)132<1917:aarmmi>2.0.co;2.

Whyte, F. S., Taylor, M. A., Stephenson, T. S., and Campbell, J. D. Features of the Caribbean low level jet. *Int. J. Climatol.*, 28(1):119–128, 2008. URL https://doi.org/10.1002/joc.1510.

Wilcox, L. J., Dunstone, N., Lewinschal, A., Bollasina, M., Ekman, A. M., and Highwood, E. J. Mechanisms for a remote response to Asian aerosol emissions in boreal winter. *Atmos Chem. Phys.*, 19:9081–9095, 2019. URL https://doi.org/10.5194/acp-19-9081-2019.

Wuebbles, D. J., Fahey, D. W., and Hibbard, K. A. Climate science special report: fourth national climate assessment. I, 2017. URL 10.7930/J08S4N35.

Xie, P. and Arkin, P. A. Global precipitation: A 17-year monthly analysis based on gauge observations, satellite estimates, and numerical model outputs. *Bull. Amer. Meteor. Soc.*, 78(11):2539–2558, 1997. URL https://doi.org/10.1175/1520-0477(1997)078<2539:gpayma>2.0.co;2.

Xie, S.-P., Xu, H., Kessler, W. S., and Nonaka, M. Air–sea interaction over the eastern Pacific warm pool: Gap winds, thermocline dome, and atmospheric convection. *J. Clim.*, 18(1):5–20, 2005. URL https://doi.org/10.1175/jcli-3249.1.

Yeager, S., Danabasoglu, G., Rosenbloom, N., Strand, W., Bates, S., Meehl, G., Karspeck, A., Lindsay, K., Long, M., Teng, H., et al. Predicting near-term changes in the Earth System: A large ensemble of initialized decadal

prediction simulations using the Community Earth System Model. *Bull. Am. Meteorol. Soc.*, 99(9):1867–1886, 2018. URL https://doi.org/10.1175/bams-d-17-0098.1.

Yu, S., Alapaty, K., Mathur, R., Pleim, J., Zhang, Y., Nolte, C., Eder, B., Foley, K., and Nagashima, T. Attribution of the United States warming hole: Aerosol indirect effect and precipitable water vapor. *Sci. Rep.*, 4:6929, 2014. URL https://doi.org/10.1038/srep06929.

Zelinka, M. D., Andrews, T., Forster, P. M., and Taylor, K. E. Quantifying components of aerosol-cloud-radiation interactions in climate models. *J. Geophys. Res. Atmos.*, 119(12):7599–7615, 2014. URL https://doi.org/10.1002/2014JD021710.

Zhang, C. Madden–Julian oscillation: Bridging weather and climate. *Bull. Am. Meteorol. Soc.*, 94(12):1849–1870, 2013. URL https://doi.org/10.1175/bams-d-12-00026.1.

Zhang, X., Alexander, L., Hegerl, G. C., Jones, P., Tank, A. K., Peterson, T. C., Trewin, B., and Zwiers, F. W. Indices for monitoring changes in extremes based on daily temperature and precipitation data. *Wiley Interdiscip. Rev. Clim. Change*, 2(6):851–870, 2011. URL https://doi.org/10.1002/wcc.147.